

INVESTIGATION OF DUAL ACTIVE NUCLEI, OUTFLOWS, SHOCK-HEATED GAS, AND YOUNG STAR CLUSTERS IN MARKARIAN 266

J. M. MAZZARELLA,¹ K. IWASAWA,² T. VAVILKIN,³ L. ARMUS,⁴ D.-C. KIM,^{5,6} G. BOTHUN,⁷ A. S. EVANS,^{5,6} H. W. W. SPOON,⁸ S. HAAN,^{4,9} J. H. HOWELL,⁴ S. LORD,¹⁰ J. A. MARSHALL,^{4,11} C. M. ISHIDA,¹² C. K. XU,¹⁰ A. PETRIC,^{4,11} D. B. SANDERS,¹³ J. A. SURACE,⁴ P. APPLETON,¹⁰ B.H.P. CHAN,¹ D. T. FRAYER,⁶ H. INAMI,⁴ E. YE. KHACHIKIAN,¹⁴ B. F. MADORE,^{15,1} G. C. PRIVON,⁵ E. STURM,¹⁶ VIVIAN U,¹³ S. VEILLEUX¹⁷

(Received; Accepted 29 July 2012)

To appear in the *Astronomical Journal*; draft version 15 Aug 2012

ABSTRACT

Results of observations with the *Spitzer*, *Hubble*, *GALEX*, *Chandra*, and *XMM-Newton* space telescopes are presented for the Luminous Infrared Galaxy (LIRG) merger Markarian 266. The SW (Seyfert 2) and NE (LINER) nuclei reside in galaxies with Hubble types SBb (pec) and S0/a (pec), respectively. Both companions are more luminous than L^* galaxies and they are inferred to each contain a $\approx 2.5 \times 10^8 M_{\odot}$ black hole. Although the nuclei have an observed hard X-ray flux ratio of $f_X(NE)/f_X(SW) = 6.4$, Mrk 266 SW is likely the primary source of a bright Fe $K\alpha$ line detected from the system, consistent with the reflection-dominated X-ray spectrum of a heavily obscured AGN. Optical knots embedded in an arc with aligned radio continuum radiation, combined with luminous H_2 line emission, provide evidence for a radiative bow shock in an AGN-driven outflow surrounding the NE nucleus. A soft X-ray emission feature modeled as shock-heated plasma with $T \sim 10^7$ K is co-spatial with radio continuum emission between the galaxies. Mid-infrared diagnostics provide mixed results, but overall suggest a composite system with roughly equal contributions of AGN and starburst radiation powering the bolometric luminosity. Approximately 120 star clusters have been detected, with most having estimated ages less than 50 Myr. Detection of $24 \mu\text{m}$ emission aligned with soft X-rays, radio continuum and ionized gas emission extending $\sim 34''$ (20 kpc) north of the galaxies is interpreted as $\sim 2 \times 10^7 M_{\odot}$ of dust entrained in an outflowing superwind. At optical wavelengths this Northern Loop region is resolved into a fragmented morphology indicative of Rayleigh-Taylor instabilities in an expanding shell of ionized gas. Mrk 266 demonstrates that the dust “blow-out” phase can begin in a LIRG well before the galaxies fully coalesce during a subsequent ULIRG phase, and rapid gas consumption in luminous dual AGNs with kpc-scale separations early in the merger process may explain the paucity of detected binary QSOs (with pc-scale orbital separations) in spectroscopic surveys. An evolutionary sequence is proposed representing a progression from dual to binary AGNs, accompanied by an increase in observed L_X/L_{IR} ratios by over four orders of magnitude.

Subject headings: galaxies: interactions — galaxies: nuclei — galaxies: active — galaxies: Seyfert — galaxies: starburst — galaxies: star clusters: general

¹Infrared Processing & Analysis Center, MS 100-22, California Institute of Technology, Pasadena, CA 91125; mazz,bchan@ipac.caltech.edu

²ICREA and Institut del Ciències del Cosmos (ICC), Universitat de Barcelona (IEEC-UB), Martí i Franquès 1, 08028 Barcelona, Spain; kazushi.iwasawa@icc.uib.edu

³Department of Physics and Astronomy, State University of New York at Stony Brook, Stony Brook, NY 11794-3800; vavilkin@grad.physics.sunysb.edu

⁴Spitzer Science Center, MS 314-6, California Institute of Technology, Pasadena, CA 91125; lee,jhhowell,jason,inami,haan@ipac.caltech.edu

⁵Department of Astronomy, University of Virginia, Charlottesville, VA 22904-4325; aeavans,gcp8y@virginia.edu

⁶National Radio Astronomy Observatory, 520 Edgemont Road, Charlottesville, VA 22903-2475; dkim,dfrayer@nrao.edu

⁷University of Oregon, Physics Department, Eugene OR, 97402; nuts@bigmoo.uoregon.edu

⁸Department of Astronomy, Cornell University, Ithaca, NY 14853; spoon@isc.astro.cornell.edu

⁹CSIRO Astronomy & Space Science, ATNF, Marsfield NSW 2122, Australia; sebastian.haan@csiro.au

¹⁰NASA Herschel Science Center, MS 100-22, California Institute of Technology, Pasadena, CA 91125;

lord,apple,cxu@ipac.caltech.edu

¹¹Astronomy Department, California Institute of Technology, MS 249-17, Pasadena, CA 91125; jason.marshall@caltech.edu,ap@astro.caltech.edu

¹²Subaru Telescope, National Astronomical Observatory of Japan, Hilo, HI 96720; cmishida@mac.com

¹³Institute for Astronomy, University of Hawaii, 2680 Woodlawn Drive, Honolulu, HI 96822; sanders,vivian@ifa.hawaii.edu

¹⁴Byurakan Astrophysical Observatory, Academician of National Academy of Sciences of Armenia, Byurakan, 378433 Aragatsodn Province, Republic of Armenia; khache@bao.sci.am

¹⁵The Observatories, Carnegie Institution of Washington, 813 Santa Barbara Street, Pasadena, CA 91101; barry@obs.carnegiescience.edu

¹⁶Max-Planck-Institut für extraterrestrische Physik, Postfach 1312, 85741 Garching, Germany; sturm@mpe.mpg.de

¹⁷Department of Astronomy, University of Maryland, College Park, MD 20742; veilleux@astro.umd.edu

1. INTRODUCTION

1.1. *LIRGs, ULIRGs and GOALS*

Luminous Infrared Galaxies (LIRGs; $10^{11} L_{\odot} \leq L_{ir} < 10^{12} L_{\odot}$) and Ultraluminous Infrared Galaxies (ULIRGs; $L_{ir} \geq 10^{12} L_{\odot}$) are intriguing objects with widespread implications for galaxy evolution. They contain the highest known rates of star formation, they exhibit a high frequency of active galactic nuclei (AGNs) and large-scale outflows (superwinds), and mounting evidence indicates that the majority of local (U)LIRGs represent an evolutionary process involving the transformation of major mergers between dusty, gas-rich disk galaxies into elliptical galaxies hosting classical UV-excess QSOs or powerful radio galaxies (e.g., Sanders & Mirabel 1996; Veilleux 2006). At redshifts of $z \sim 1$, LIRGs have a higher space density than ULIRGs and dominate the total star-formation density at that epoch (Le Floch et al. 2005). At $z \sim 2$ the contributions of LIRGs and ULIRGs to the total IR luminosity density are about equal (e.g., Caputi et al. 2007). Since LIRGs and ULIRGs were much more common in the early universe, these populations are fundamental in understanding both star formation and galaxy evolution.

The Great Observatories All-Sky LIRG Survey (GOALS)¹⁸ is utilizing imaging and spectroscopic data from NASA’s *Spitzer*, *Hubble*, *Chandra* and *GALEX* space observatories, in combination with ground-based observations, in a comprehensive study of more than 200 of the most luminous infrared galaxies in the local universe (Armus et al. 2009). The sample consists of 181 LIRGs and 23 ULIRGs that form a statistically complete subset of the flux-limited *IRAS* Revised Bright Galaxy Sample (RBGS), which itself is comprised of 629 extragalactic objects with 60 μm flux densities above 5.24 Jy and Galactic latitudes $|b| > 5^{\circ}$ (Sanders et al. 2003).

1.2. *Dual AGNs in Major Mergers*

A key scientific driver for GOALS is the investigation of the relative time-scales and energetics of active star formation and AGN phenomena during different phases of the merger sequence. It is now widely accepted that all massive galaxies likely have a supermassive black hole (SMBH) in their centers (e.g., Ferrarese & Ford 2005), with a SMBH mass proportional to the mass of the stellar bulge ($M_{\text{SMBH}}/M_{\text{bulge}} \approx 0.2\%$; Marconi & Hunt 2003). However, many uncertainties remain regarding the fueling of paired SMBHs during major mergers. While the nuclei are still separated by kpc scales, how common is it for both SMBHs to have accretion rates high enough to produce energetically significant *dual AGNs*, as opposed to one or both nuclei being powered predominantly by a burst of star formation? How do AGN characteristics depend on properties of the host galaxies and dynamics of the encounter? Are the fuel supplies and accretion rates sufficient to sustain two luminous AGNs well into a true *binary* stage (e.g., binary QSOs), when the SMBHs are closely bound ($r < 100$ pc) in Keplerian orbits inside a dynamically relaxed (elliptical) merger remnant (e.g., Colpi & Dotti 2009)? Is there something special about the physical conditions in systems that host dual AGNs, or is their lack of detection in some (U)LIRGs merely

a matter of observing them during the right stage prior to merging (i.e., an evolutionary timing coincidence), or accounting for differences in nuclear dust obscuration? What is the relative importance of AGNs and star formation in the energetics of the “superwind” phenomena that appears to be ubiquitous in (U)LIRGs (e.g., see the review by Veilleux 2006)?

Although (U)LIRGs are predominantly systems involving major mergers, extensive observations utilizing optical and infrared spectroscopy have so far turned up surprisingly few systems containing confirmed dual AGNs. This has a number of possible explanations. First, (U)LIRGs contain large quantities of centrally concentrated dust that can effectively obscure one or both AGNs at optical, near-infrared, and even mid-infrared wavelengths (e.g. Laurent et al. 2000; Spoon et al. 2004). Therefore, circumnuclear star formation can dominate the observed spectra while in reality a powerful AGN may be buried inside. Second, about 30% of observed LIRGs (e.g., Veilleux et al. 1995), and $\sim 40\%$ of ULIRGs (e.g., Veilleux et al. 1999) are classified as LINERs based on optical spectroscopy. It has proven difficult to distinguish between low-luminosity AGNs (photoionization from radiation due to accretion onto a SMBH), photoionization from very hot stars, and shock heating (induced by SNe and starburst-driven superwinds) as the primary source of ionization in LINERs (e.g., Veilleux et al. 1999).

Recent results indicate that most nearby LINERs are dominated by photo-ionization rather than shock heating, and that they are an important class of AGNs distinguished primarily by a lower accretion rate than in Seyfert nuclei (Kewley et al. 2006; Ho 2008). This implies that the frequency of dual AGNs may be much higher than inferred to date. Only recently, with the capability of the *Chandra X-ray Observatory* to penetrate their extensive dust cocoons with high-resolution hard X-ray observations, have suspected dual AGNs been confirmed in a small number of (U)LIRGs. Perhaps the best known example is NGC 6240, in which hard X-rays and strong Fe K α emission lines indicate the presence of two AGNs with a projected separation of $1''.4$ (1 kpc) (Komossa et al. 2003). A second case is the ULIRG Mrk 463, a system first pointed out as an active double-nucleus galaxy by Petrosian, Saakian & Khachikian (1978). The eastern component undoubtedly hosts a dust-enshrouded Type 1 AGN that is powering apparently young radio jets (Mazzarella et al. 1991a), but conflicting optical spectral classifications from various studies left the nature of the western nucleus in doubt (LINER, Seyfert 2, or starburst/AGN composite). Dual AGNs in Mrk 463 have been confirmed recently via detection of two compact, luminous sources of hard X-rays using *Chandra* (Bianchi et al. 2008). To date, very few systems in the GOALS sample have been confirmed to contain dual AGNs via X-ray observations. The first system is NGC 6240, and the second is Arp 299 (NGC 3690 + IC 694) (Ballo et al. 2004). This article presents an in-depth investigation of a third system in this rare class of objects that has considerable importance for understanding the evolution of galaxy mergers and their remnants.

1.3. *Complex Phenomena in Mrk 266*

One of the most remarkable LIRGs in the local Universe is Mrk 266 (NGC 5256). The system was first

¹⁸ <http://goals.ipac.caltech.edu/>

called out as an extraordinary object in the Markarian Survey (First Byurakan Sky Survey) of ultraviolet-excess galaxies due to the presence of two nuclei within what appeared to be a single galaxy (Petrosian, Saakian & Khachikian 1978, 1979). In a detailed spectroscopic investigation at optical wavelengths, Petrosian, Saakian & Khachikian (1980) showed that the nuclei have a radial velocity difference of 280 km s^{-1} , and based on the assumption that the nuclei revolve about a common center of gravity, masses of 7×10^9 and $10 \times 10^9 M_{\odot}$ were estimated for the SW and NE nuclei, respectively. As for all objects in the Markarian Survey, Mrk 266 stood out because its UV-to-optical flux ratio is higher than in normal galaxies. However, Mrk 266 is also a LIRG, with an infrared luminosity of $L_{\text{ir}} = 3.6 \times 10^{11} L_{\odot}$ (8 - 1000 μm , as estimated from flux densities in all four *IRAS* bands; Armus et al. 2009). As shown in the current study (§3.5), the global spectral energy distribution indicates the bulk of its energy is emitted in the mid-to far-infrared; much more energy is being emitted at the peak of the SED than is escaping in UV radiation ($\nu L_{\nu}(70\mu\text{m})/\nu L_{\nu}(0.2\mu\text{m}) \approx 20$).

Mrk 266 contains a filamentary nebula of ionized hydrogen ~ 30 kpc in diameter (Armus et al. 1990) surrounding the two nuclei. A luminous X-ray nebula ~ 100 kpc in extent detected by *ROSAT* (also surrounding the two nuclei) and complex kinematics derived from optical spectroscopy revealed one of the most spectacular examples of an outflowing, starburst-driven superwind (Wang et al. 1997). In addition to radio continuum emission from the two nuclei, a bright radio source located between the nuclei was detected and interpreted as enhanced synchrotron emission induced by extensive shocks at the interface of the merging galaxies (Mazzarella et al. 1988). Imaging in $\text{H}\alpha + [\text{NII}]$ (Mazzarella et al. 1988; Armus et al. 1990), $[\text{O III}] \lambda 5007$ (Hutchings et al. 1988) and soft X-rays (Kollatschny & Kowatsch 1998) also revealed a bright loop of emission extending $\sim 24''$ (17 kpc) to the north-east and connected to the SW (Seyfert 2) nucleus (Wang et al. 1997). Recent *Chandra* observations have resolved X-ray emission from both nuclei, and detected diffuse emission associated with the northern feature and between the nuclei (Brassington et al. 2007). The nature of the northern emission region (hereafter called the Northern Loop) has remained controversial, with suggestions including a component of the superwind (Wang et al. 1997), a “jet” from an AGN (Kollatschny & Kowatsch 1998), and a tidal tail (Brassington et al. 2007).

Mrk 266 is worthy of further detailed study because it manifests complex processes that are rarely detected simultaneously, presumably due to their relatively short time scales: vigorous star formation, a candidate dual AGN (depending on the ionizing source of the LINER), a powerful large-scale superwind, and substantial radio continuum and X-ray emission between the nuclei. The relative proximity of the system permits close-up investigation of an important stage in the evolution of major mergers that may involve the transformation of LIRGs into ULIRGs, AGN feedback with the ISM, and implications for fueling (or quenching) of accreting SMBHs which galaxy evolution models predict to have occurred in large numbers during earlier epochs.

In this study, new observations and re-processed

archival data from the *Spitzer*, *Hubble*, *Chandra*, *XMM-Newton* and *GALEX* space telescopes are analyzed in combination with multi-wavelength ground-based data. Imaging, photometric, and spectroscopic data are presented in §2. In §3 the new data are interpreted to obtain new insights into the nature of the colliding/merging system (§3.1), the nuclei and circumnuclear regions (§3.2), the region between the nuclei (§3.3), the extensive superwind (§3.4), the SEDs of the major components (§3.5), newly detected star clusters (§3.6), and the molecular gas properties (§3.7). In §3.8, Mrk 266 is examined in comparison with other interacting systems with strong radiation sources between the galaxies, and a sequence is proposed that may represent an evolutionary progression from dual AGNs (with kpc-scale separations) to binary AGNs (with parsec-scale orbits). Due to the large number of new measurements spanning many spectral regions, the basic observations and data reductions are described in §2, but most of the corresponding figures and tables are displayed alongside their interpretation and analyses in §3. Conclusions are summarized in §4. A systemic heliocentric recession velocity of $8353 \pm 13 \text{ km s}^{-1}$ (de Vaucouleurs et al. 1991) is adopted, corrected to $8825 \pm 22 \text{ km s}^{-1}$ via the flow model of Mould et al. (2000a,b) that accounts for three major attractors in the local Universe. We adapt cosmological parameters $H_0 = 70 \text{ km s}^{-1} \text{ Mpc}^{-1}$, $\Omega_M = 0.28$, and $\Omega_V = 0.72$ (Hinshaw et al. 2009). The corresponding luminosity distance to Mrk 266 is 129 Mpc (distance modulus 35.55 mag), and the spatial scale is $0.59 \text{ kpc/arcsec}^{19}$.

2. OBSERVATIONS

2.1. Optical and Near-Infrared Imaging with *HST*

Mrk 266 was observed 2005 November 17 with the Advanced Camera for Surveys (ACS) Wide Field Channel (WFC) as part of a *HST* Cycle 14 GOALS program to investigate 88 LIRGs with $L_{\text{ir}} > 10^{11.4} L_{\odot}$ (PID 10592, PI A. Evans). The system was imaged with an integration time of 22.5 minutes in the F435W filter (B band, $0.435 \mu\text{m}$, image #J9CV48010) and 13 minutes in the F814W filter (I band, $0.814 \mu\text{m}$, image #J9CV48020). The WFC has a field of view of $202'' \times 202''$ with pixels subtending $0''.05$. The images were processed through the standard STScI pipeline to remove instrumental signatures, subtract a dark frame, apply flat fielding, remove geometric distortion, and apply flux calibration. Residual cosmic ray removal, background subtraction, and accurate astrometric calibration using sources from *2MASS* (Skrutskie et al. 2006) were also performed using procedures detailed by Evans et al. (2012, in preparation). Figure 1 presents a composite color image constructed using the B and I band data, and labels identify major features that are analyzed throughout this article.

Near-infrared observations at $1.6 \mu\text{m}$ (F160W, H band) with the NIC2 aperture of NICMOS were acquired on 1997 September 13 in Cycle 7 (PID 7328, PI M. Malkan). The image (#N44B40010) was retrieved from the *HST* archive, corrected for bad pixels, cosmic rays were removed, and astrometric calibration was applied by aligning the galaxies with the ACS images. The central regions of the SW and NE galaxies in these three *HST*

¹⁹ Provided by NED at <http://ned.ipac.caltech.edu/>

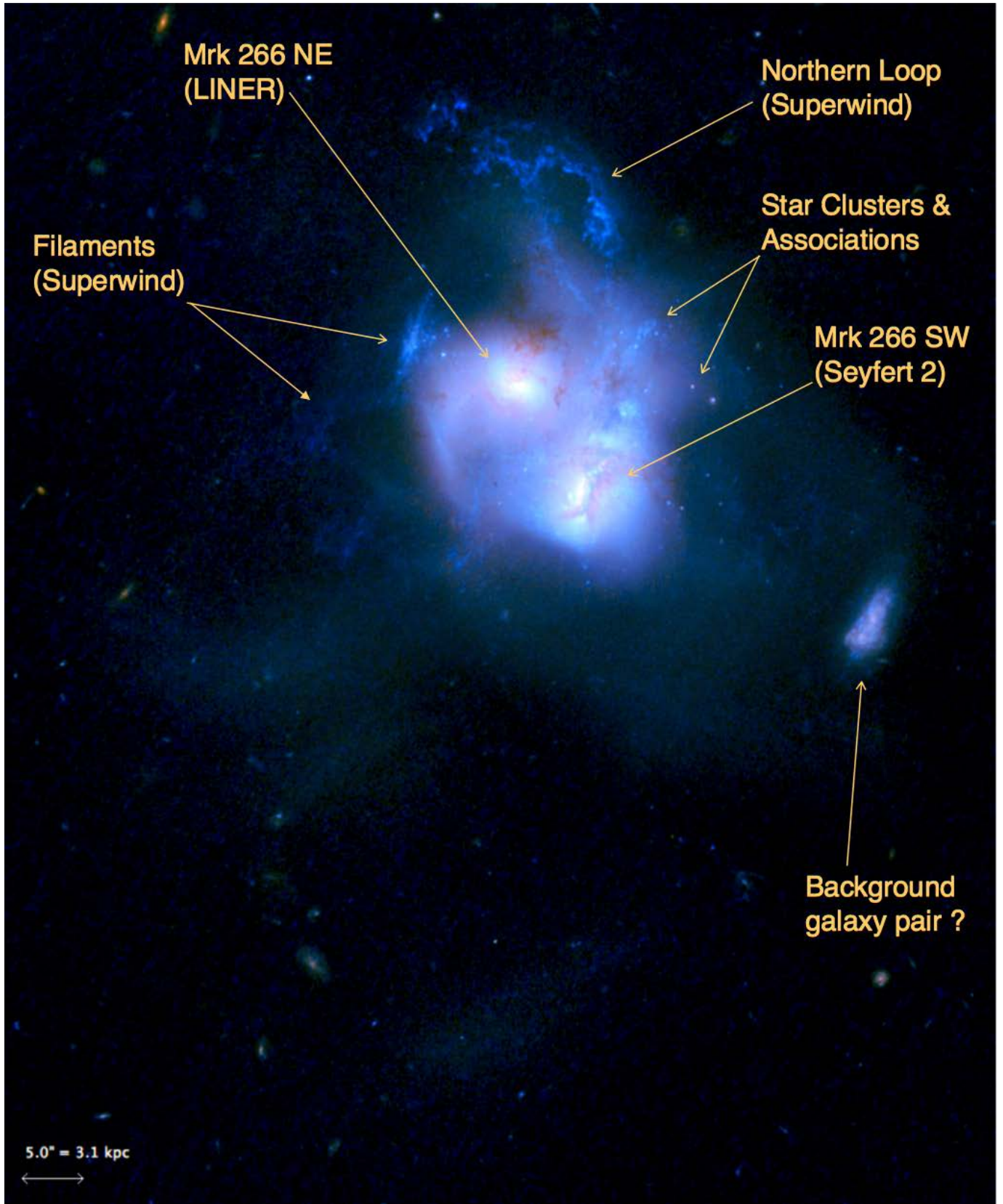


Figure 1. *HST* ACS I band and B band images combined to form a color composite image of the Mrk 266 system and its tidal features. North is up and east is left. The image field of view is $1'.4 \times 1'.6$, with a scale bar in the lower left corner. The color table has been chosen to maximize contrast for faint extended structures. The limiting surface brightness is 25.0 and $24.5 \text{ mag arcsec}^{-2}$ in the B and I band, respectively. Labels identify major structures that are studied throughout this article.

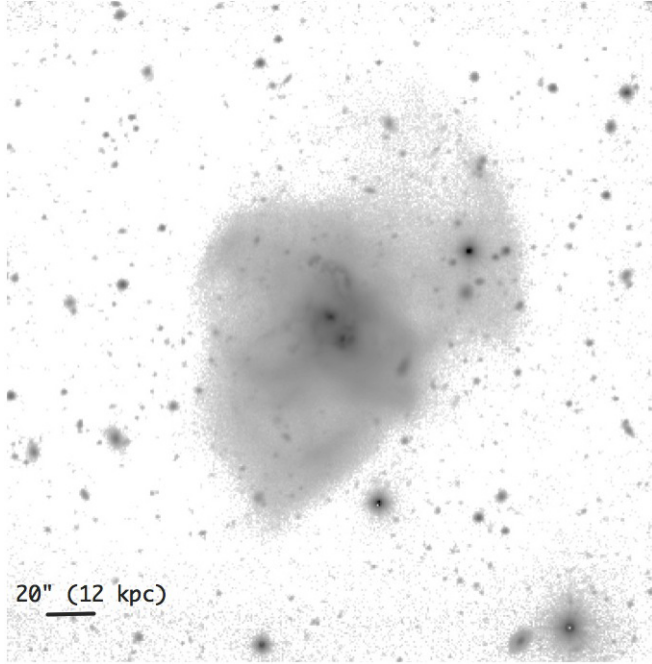


Figure 2. The result of stacking B, V, and I band images obtained with the University of Hawaii 2.2 m telescope (effective seeing $\sim 1''.5$ FWHM). The field of view is 150 kpc x 150 kpc ($4''.2 \times 4''.2$), and a scale bar is provided in the lower left. Faint, low surface-brightness emission spanning $2''.9$ (≈ 103 kpc) is detected. band are displayed in context with their analysis in §3.1.

2.2. Deep B+V+I Band Ground-Based Imaging

To complement the *HST* high-resolution imagery and reveal the faintest emission possible, Figure 2 shows the result of spatial registration and stacking of B, V, and I band images obtained on 1998 December 22 and 2000 May 04 with the University of Hawaii 2.2 m telescope (effective seeing $\sim 1''.5$ FWHM). Details of the data acquisition and reduction are given by Ishida (2004). The data are presented using Gaussian equalization to contrast the low and high surface-brightness features in the same view. Highly asymmetric, low surface-brightness emission can be seen spanning ≈ 103 kpc ($2''.9$) from the SE to NW extremities, which is approximately twice the extent of the faintest emission visible in the *HST* ACS data, SDSS, and previously published imagery.

2.3. X-Ray Observations with *Chandra* and *XMM-Newton*

2.3.1. *Chandra* Observations

Chandra observations were obtained with the Advanced CCD Imaging Spectrometer (ACIS-S) on 2001 November 02 (PI A. Read) with a total integration time of 19.95 ks. The spatial resolution is $\sim 1''$ FWHM. These observations were first presented by Brassington et al. (2007). In order to make refined measurements, highlight additional features, and analyze the X-ray properties alongside observations at other wavelengths, the data were taken from the *Chandra* Data Archive²⁰ (OBSID #2044) and re-processed using standard procedures in CIAO 4.0. The data were corrected for detector response and converted to flux density (f_ν) units. Details of

²⁰ <http://cxc.harvard.edu/cda/>

the data reduction procedures can be found in Iwasawa et al. (2011). Figure 3 shows the resulting full band (0.4 - 7 keV) image, the hard band (2-7 keV) image, a smoothed version of the full band data, and the 20 cm radio continuum image from Mazzarella et al. (1988). Figure 4 illustrates apertures with parameters listed in Table 1 that were used to define regions of interest, and Figure 5 shows the X-ray spectra constructed in these regions.

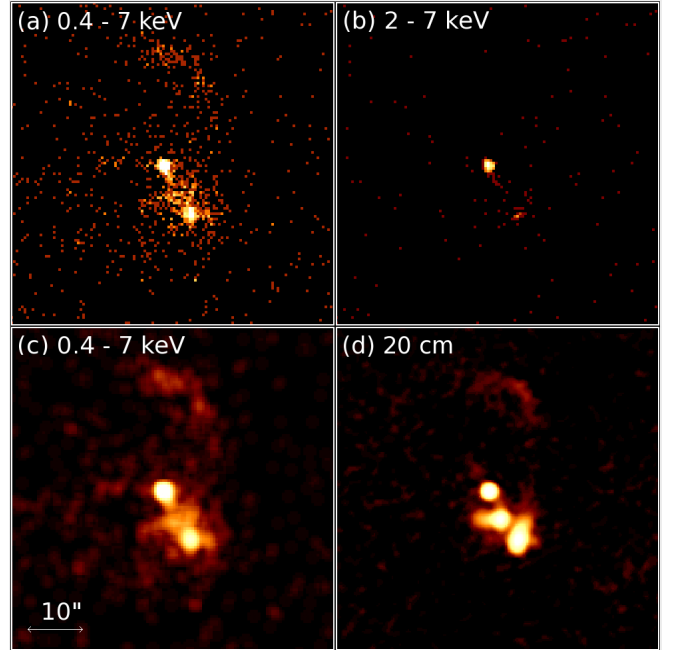


Figure 3. The X-ray and radio continuum emission in Mrk 266: (a) *Chandra* 0.4 - 7 keV (full band) X-ray image; (b) 2 - 7 keV (hard band) X-ray image; (c) 0.4 - 7 keV X-ray data (same as panel a) smoothed with a 2-pixel Gaussian kernel; and (d) 20 cm radio continuum image (VLA) from Mazzarella et al. (1988). The scale bar indicates $10''$.

2.3.2. *XMM-Newton* Observations

X-ray observations with *XMM-Newton*, reaching significantly higher energies (10 keV) than *Chandra* (7 keV), were acquired with the European Imaging Photon Camera (EPIC) on 2002 May 15 (PI A. Read). The data obtained with the EPIC pn-CCD camera were utilized, providing an angular resolution of $\sim 6''$ FWHM and a spectral resolution of $(E/\delta E) \sim 40$. The observation was performed with the Thin Filter in the extended full-window imaging mode. The data set (#0055990501) was taken from the *XMM-Newton* Science Archive²¹ and processed with standard procedures in the software packages SAS 8.1 and HEASoft 6.6 utilizing the latest calibration files (as of 2009 January). Time intervals with high particle background levels were discarded, leaving useful data with an effective exposure time of 13.2 ks. The count rate in the 0.4-10 keV band is 0.19 count s^{-1} . The X-ray emission is only marginally resolved by *XMM*, therefore the spectrum for the total system emission within a large aperture of $45''$ radius is produced here. Figure 6 shows the resulting *XMM* spectrum of the integrated emission from the system. Key features include Si XIII K α (1.853

²¹ <http://xmm.esac.esa.int/xsa/>

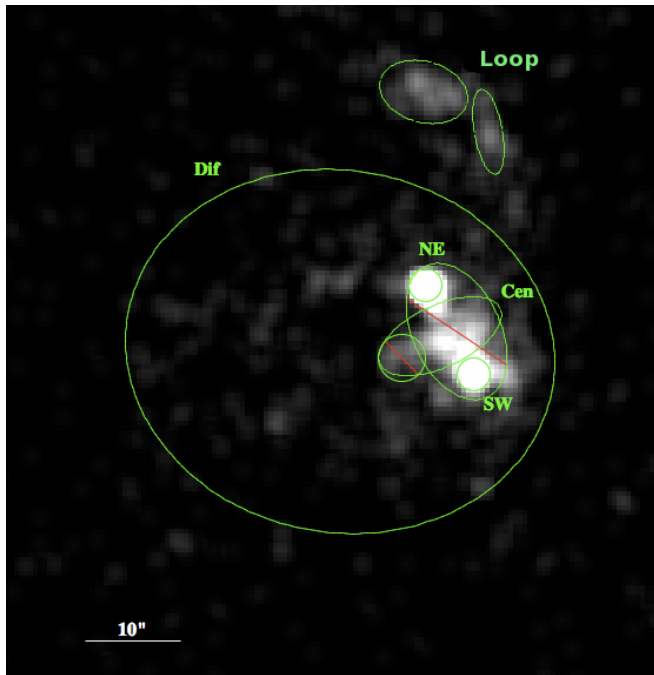


Figure 4. Elliptical apertures used to define regions of interest for extraction of X-ray spectra from the *Chandra* data: Mrk 266 NE (“NE”), Mrk 266 SW (“SW”), the central region between the nuclei (“Cen”), the Northern Loop (“Loop”), and surrounding diffuse emission (“Dif”). The two ellipses marked with red lines indicate regions subtracted from the ellipse labeled “Dif” to estimate the diffuse component. Parameters for the regions are listed in Table 1. A circular aperture of radius $33''$ used to measure the integrated system flux is not illustrated.

Table 1
Elliptical Apertures for X-ray Measurements

| Region (1) | RA, DEC (J2000) (2) | a'' (3) | b/a (4) | PA° (5) |
|----------------------|----------------------------|--------------|--------------|-------------------|
| SW | (13:38:17.31,+48:16:31.9) | 1.7 | 1.00 | ... |
| NE | (13:38:17.82,+48:16:41.2) | 1.7 | 1.00 | ... |
| Center | (13:38:17.66,+48:16:35.8) | 6.9 | 0.47 | 155 |
| Loop A | (13:38:17.15,+48:16:57.2) | 4.5 | 0.32 | 10 |
| Loop B | (13:38:17.83,+48:17:01.4) | 4.7 | 0.68 | 75 |
| Diffuse ^a | (13:38:18.71,+48:16:34.2) | 22.5 | 0.84 | 80 |
| Diffuse -1 | -(13:38:17.49,+48:16:36.3) | 4.6 | 0.61 | 25 |
| Diffuse -2 | -(13:38:18.07,+48:16:33.6) | 2.5 | 1.00 | ... |
| Total | (13:38:17.66,+48:16:35.8) | 33.0 | 1.00 | ... |

^a The diffuse emission is approximated by the flux within this large ellipse after subtraction of the flux in the two small ellipses in the following two rows, which are preceded by a minus sign in this table and marked with red lines in Figure 4.

keV) emission, as also observed in the *Chandra* spectra of the two nuclei (Fig. 5), and strong Fe $K\alpha$ line emission at 6.4 keV.

2.3.3. X-ray Measurements

Spectral measurements and results from continuum model fitting of the *Chandra* and *XMM-Newton* observations are presented in Table 2. The sum of the emission in the elliptical regions misses some low surface-brightness emission that is recovered in measurements of the total system in a circular aperture with a radius of $33''$. The total system fluxes measured by *Chandra*

Table 2
X-Ray Measurements

| Region (1) | F(Fe $K\alpha$) (2) | kT (soft) (3) | $F_x(\text{soft})$ (4) | $F_x(\text{hard})$ (5) |
|--------------------------|-------------------------|------------------------|---------------------------|---------------------------|
| Mrk 266 SW | $1.2^{+0.7}_{-0.5}$ | $0.77^{+0.07}_{-0.08}$ | 2.2 | 2.2 |
| Mrk 266 NE | < 1.6 | $0.72^{+0.11}_{-0.10}$ | 3.0 | 14 |
| Between Nuclei | ... | $0.66^{+0.06}_{-0.07}$ | 2.6 | 1.0 |
| Northern Loop | ... | $0.35^{+0.05}_{-0.05}$ | 1.4 | ... |
| Diffuse Region | ... | $0.54^{+0.04}_{-0.04}$ | 4.1 | ... |
| Total (<i>Chandra</i>) | ... | ... | 18 | 20 |
| Total (<i>XMM</i>) | $1.5^{+0.8}_{-0.6}$ | ... | 18 | 23 |

Note. — Measurements of the *Chandra* spectra in regions of interest; they are not corrected for absorption. Column (1): Region of interest, as illustrated in Fig. 4. Column (2): Flux of the Fe $K\alpha$ line in units of 10^{-6} ph cm^{-2} s^{-1} . The rest-frame energy measured from the XMM spectrum for this feature is $6.50^{+0.10}_{-0.05}$ keV. The value for the NE nucleus is a 2σ upper limit. Column (3): Temperature (kT in units of keV) of the soft (0.5-2 keV) X-ray emission with 1σ uncertainties. Column (4): Flux in the soft (0.5-2 keV) X-ray band in units of 10^{-14} erg cm^{-2} s^{-1} ; the estimated relative uncertainty is 20%. Column (5): Flux in the hard (2-7 keV) X-ray band in units of 10^{-14} erg cm^{-2} s^{-1} ; the estimated relative uncertainty is 30%. No flux is detected above 2 keV in the Northern Loop or in the Diffuse Region. Mrk 266 SW shows some emission above 2 keV, but most of the detected flux appears to originate in the Fe $K\alpha$ line. The NE and SW galaxies also both show strong Si XIII emission at 1.8-1.9 keV.

are, within the uncertainties (i.e., 20% in $F_x(\text{soft})$ and 30% in $F_x(\text{hard})$), in agreement with the XMM total flux measurements listed in Table 2. There may be some contribution of photoionized gas (by the AGNs) in the soft X-ray emission, but the S/N is insufficient to fit this component; therefore, the temperatures given in Table 2 are obtained from a model fit consisting of thermal emission due to star formation. Mrk 266 NE has an AGN component, which is modeled by an absorbed power-law with photon index 1.8 (fixed) and $N_{\text{H}} = 8.2^{+1.8}_{-1.3} \times 10^{22}$ cm^{-2} ; correcting for this absorption suggests an intrinsic hard-band flux of 2.7×10^{-13} erg cm^{-2} s^{-1} . There is a tail of hard X-ray emission in the source between the nuclei, but its spectral shape is not well constrained; the 2-7 keV flux given here is mostly due to this hard tail.

2.4. Ultraviolet Imaging with GALEX and XMM-Newton OM

Ultraviolet images of Mrk 266 were obtained on 2004 June 04 with an integration time of 111 sec in the NUV (2271 Å) and FUV (1528 Å) bands during the All Sky Imaging Survey (AIS) conducted by the Galaxy Evolution Explorer (GALEX). The data were extracted from MAST (tile AISCHV3.104.01135) as provided by the standard GALEX data processing pipeline, and photometry was performed directly from these images using procedures outlined by Howell et al. (2010).

Contemporaneously with the X-ray observations by *XMM-Newton* summarized above, the Optical/UV Monitor Telescope (XMM-OM) obtained observations of Mrk 266 in the U (3000 - 3900 Å), UVW1 (2450-3200 Å), and UVW2 (1800-2250 Å) filters with exposure times of 800, 1000 and 1400 sec, respectively. The XMM-OM instrument and data characteristics are described by Mason et al. (2001). These images have significantly better spatial resolution ($\sim 2''$ FWHM) and higher sensitiv-

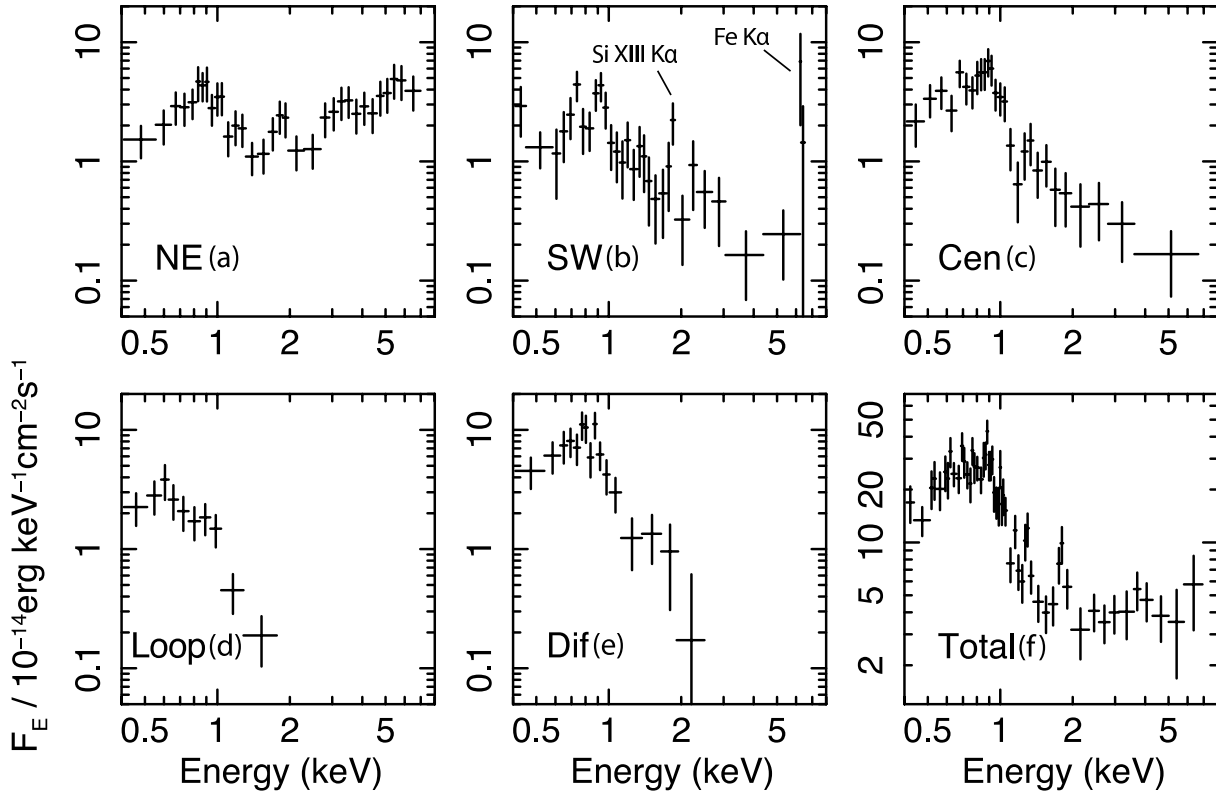


Figure 5. *Chandra* X-ray spectra covering 0.35 - 7 keV for the regions illustrated in Figure 4: (a) Mrk 266 NE (“NE”); (b) Mrk 266 SW (“SW”); (c) the central region between the nuclei (“Cen”); (d) the Northern Loop (“Loop”); (e) the diffuse emission (“Dif”); (f) and the total system emission (“Total”). The horizontal lines indicate the variable-width energy bands, and the vertical lines are 1σ error bars.

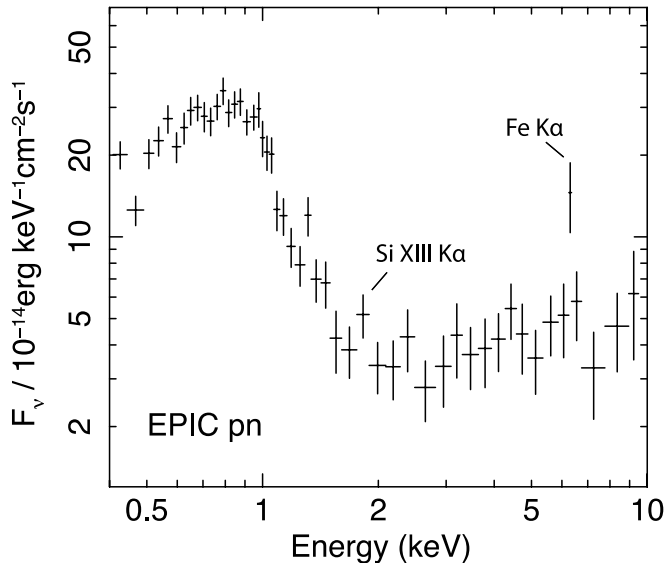


Figure 6. The 0.5 - 10 keV X-ray spectrum of Mrk 266 (integrated system) measured with the EPIC instrument onboard *XMM-Newton*. Primary features include the Fe K α emission line at 6.4 keV and an Fe K absorption edge at 7 keV.

ity than the AIS observations from GALEX, and they also considerably extend the UV coverage. The reduced and calibrated XMM-OM images, as produced using the methods documented by Kuntz et al. (2008), were obtained from MAST (dataset #0055990501). Photometric measurements (presented in §2.6.2) were calibrated using

zero-points in Table 19 of the *XMM-Newton* Users Handbook,²² which are 19.1890, 18.5662 and 16.5719 AB mag in the U, UVW1 and UVW2 filters, respectively. Figure 7 displays the UV imagery of Mrk 266 in the FUV band of GALEX and in three filters of XMM-OM.

2.5. Mid- and Far-Infrared Imaging with *Spitzer*

Imaging observations of Mrk 266 were obtained with the *Spitzer Space Telescope* as part of the Cycle 1 General Observing program for GOALS (PID 3672; PI J. Mazzarella). The Infrared Array Camera (IRAC, Fazio et al. 2004) onboard *Spitzer* was used to image the source at 3.6, 4.5, 5.8 and 8.0 μm (AOR #12305408). Due to the presence of bright galactic nuclei, the high dynamic range (HDR) mode was utilized in all four bands. The HDR frames were comprised of 1-2 second exposures to calibrate pixels that may have saturated in the 30-second exposures. The IRAC observations involved dithering to achieve redundancy to correct for cosmic ray hits and bad pixels. The Multiband Imaging Photometer for *Spitzer* (MIPS, Rieke et al. 2004) was utilized to image Mrk 266 at 24, 70 and 160 μm using the Photometry and Super Resolution mode (AOR #12349184). Each observation consisted of multiple 3-second integrations to insure adequate redundancy. Mapping cycles were used at each wavelength to correct the data for transients in the detectors. Details of the post-pipeline data processing and calibration of these data are given in Mazzarella et al.

²² <http://heasarc.gsfc.nasa.gov/docs/xmm/uhb/XMM.UHB.html>

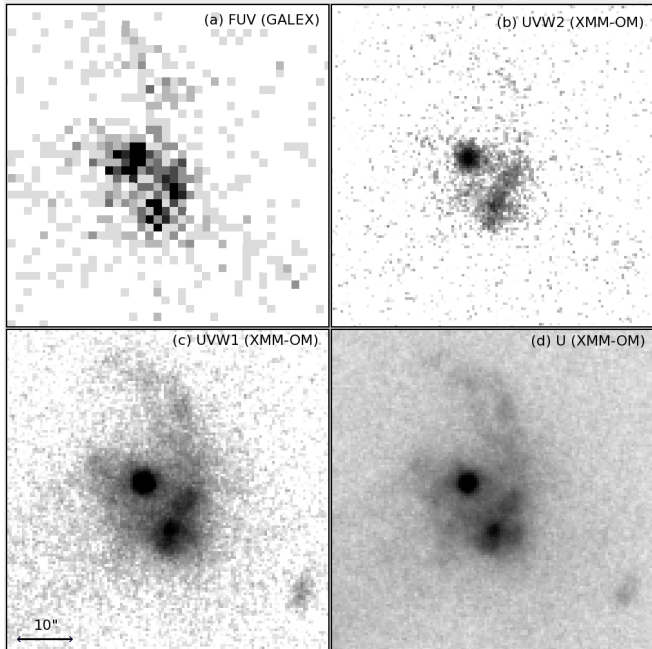


Figure 7. UV imagery of Mrk 266. (a) FUV (1528 Å) band of GALEX; (b) UVW2 (1800-2250 Å) band of XMM-OM; (c) UVW1 (2450-3200 Å) band of XMM-OM; (d) U (3000 - 3900 Å) band of XMM-OM.

2012 (in preparation). Various *Spitzer* images and photometric measurements for Mrk 266 are incorporated into the following sections in conjunction with the analyses of data in other spectral regions.

2.6. Mrk 266 from Radio Through X-Rays

2.6.1. Multi-Waveband Imagery

Figure 8 shows the structure of Mrk 266 in nine spectral regions spanning radio through X-rays using the observations discussed above. All images are displayed with the same orientation and scale to facilitate comparison. In each panel, contours of the 6 cm (4.885 GHz, $0''.3 \times 0''.4$ beam) image from Mazzarella et al. (1988) are superposed, primarily for astrometric reference. It is noteworthy that the elongated radio continuum structure with double peaks observed between the galaxy nuclei, as well as the elongated morphology of the SW galaxy, was confirmed in more sensitive 8.4 GHz observations with $0''.27 \times 0''.22$ resolution (Leipski et al. 2006).

2.6.2. Photometry and Spectral Energy Distributions

Using the data displayed in Figure 8 and other passbands discussed above, aperture photometry was performed in elliptical regions parameterized in the Appendix (Table 11 and Figure 31). However, an alternative measurement procedure was necessary for the lower resolution far-infrared data. The spatial resolution of the MIPS images, determined by the size of the *Spitzer* PSF (λ/D) are $6''$, $18''$, and $40''$ FWHM at 24, 70 and $160 \mu\text{m}$ respectively. The $24 \mu\text{m}$ IRAC image (Fig. 8c) clearly resolves the two galaxies, and it also reveals dust emission from the Northern Loop which is analyzed in §3.4.3. The $10''$ angular separation of the two galaxies is too small to be resolved by MIPS at 70 and $160 \mu\text{m}$. However, as shown in Figure 8b, the centroid of the $70 \mu\text{m}$

emission clearly indicates that the SW galaxy dominates the far-infrared emission from the system. The centroid of the $160 \mu\text{m}$ emission is also consistent with the SW galaxy providing the majority of the flux.

The 70 and $160 \mu\text{m}$ flux densities for the two galaxies were estimated as follows: The relation derived by Xu et al. (2010),

$$\log(L_{\text{ir}}) = \log(L_{24}) + 0.87(\pm 0.03) + 0.56(\pm 0.09) \times \log(L_8/L_{24}), \quad (1)$$

was used with measured monochromatic luminosities at 8 and $24 \mu\text{m}$ to derive L_{ir} ($1 - 1000 \mu\text{m}$) estimates of 2.3×10^{11} , 6.6×10^{10} , and $3.4 \times 10^{11} L_{\odot}$ for Mrk 266 SW, NE, and the total system respectively. Then, the ratios of $L_{70}/L_{\text{ir}} = 0.58$ and $L_{160}/L_{\text{ir}} = 0.19$ measured for the total system were applied to estimate the 70 and $160 \mu\text{m}$ flux densities for the two galaxies (Table 13). The estimated uncertainty in the fluxes derived using this procedure is $\approx 20\%$. Comparison of the summation of the estimated component flux densities with the measured total 70 and $160 \mu\text{m}$ flux densities for the total system (Table 12) indicates consistency within the uncertainties.

Appendix Tables 12 and 13 present photometry for the total system and for the components (SW, NE, the central region between the nuclei, and the Northern Loop). Figure 9 displays the resulting Spectral Energy Distributions (SEDs).

2.7. Mid-Infrared Spectroscopy with *Spitzer*

Mid-infrared spectroscopy of Mrk 266 obtained in staring mode with the Infrared Spectrograph (IRS, Houck et al. 2004) onboard *Spitzer* have been published by Brandl et al. (2006), Dudik et al. (2007), and Bernard-Salas et al. (2009). Unfortunately, these observations suffer from aperture effects that resulted in missing emission from some components in different spectral regions. Appendix §5.2 provides clarification of which emission features have been measured for each component of Mrk 266.

In order to overcome the limited spatial extent of the staring-mode observations, the IRS spectral map obtained on 2005 January 10 available in the *Spitzer* archive (program P03269; PI J. Gallimore; AOR #12459264) was used to construct spectra for each nucleus and for the total system. Spectral mapping with the SL module consisted of 13 integrations, each 6 seconds in duration and stepped perpendicular to the slit with an interval of $1''.8$ (half the slit width). Mapping with the LL module was performed with 5 integrations, each 6 seconds in duration and stepped perpendicular to the slit with an interval of $4''.85$ (half the slit width). The individual calibrated spectra produced by version S15.3 of the *Spitzer* Science Center pipeline were used to construct a spectral cube with the CUBISM package (Smith et al. 2007). In all cases, background observations were assembled from the non-primary slit and subtracted from the data. CUBISM was used to construct images over specific wavelength ranges and spectral features, including 5.5 , 10 , and $14 \mu\text{m}$ continuum and continuum-subtracted 6.2 , 7.7 , and $11.3 \mu\text{m}$ PAH, $9.7 \mu\text{m}$ H_2 S(3), and [S IV] $10.5 \mu\text{m}$ emission lines. These images are presented in Figure 10, where the first panel illustrates rectangular apertures used in CUBISM to extract 1-d spectra.

With a pixel size of $5''.1 \times 5''.1$ and a spatial resolution of $10''$ on the red end, we cannot use the LL observations ($14-38 \mu\text{m}$) to separate the two galaxies as we can with

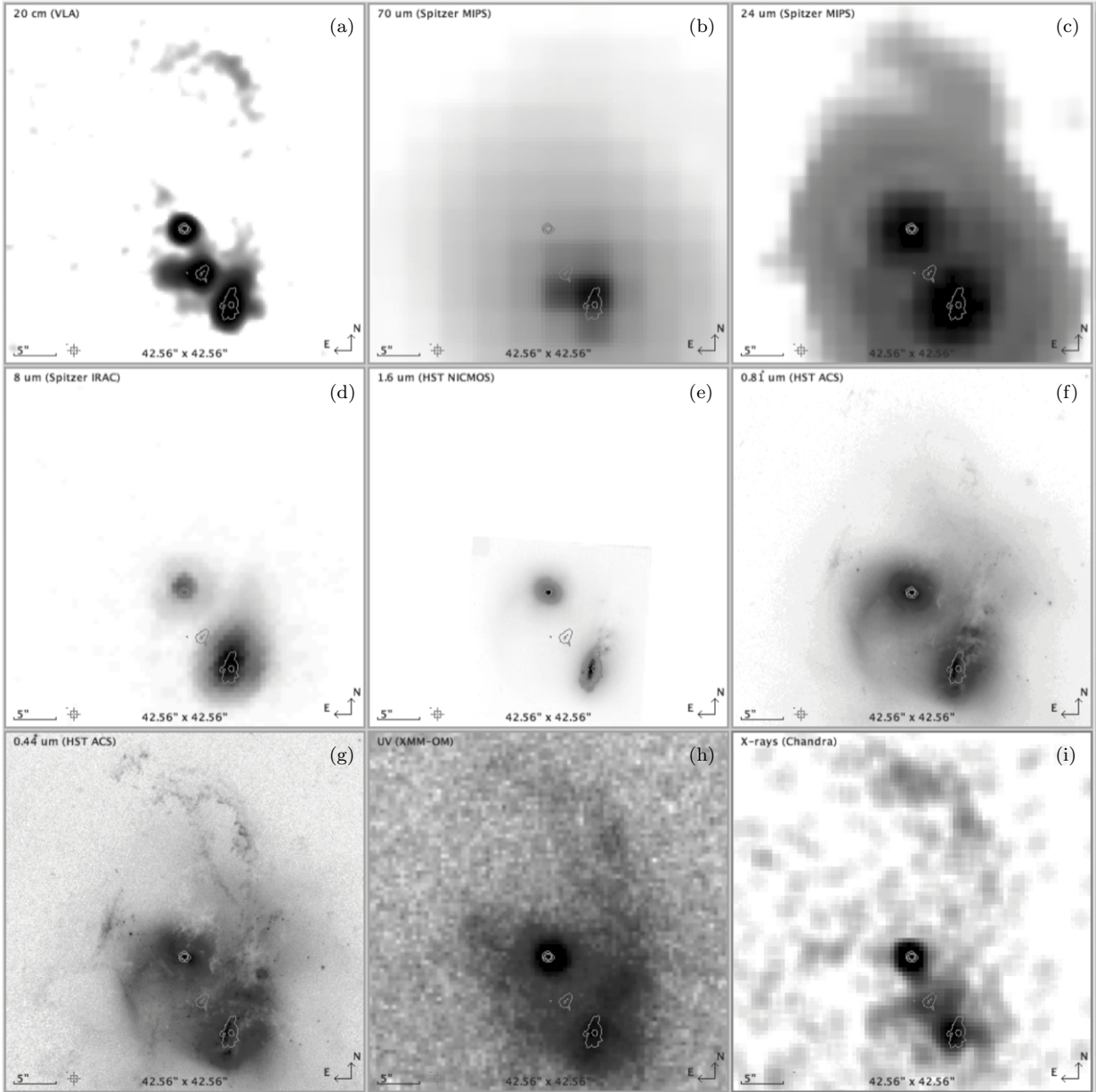


Figure 8. Imagery of Mrk 266 spanning radio through X-rays. The images are displayed at their native resolution (no PSF matching) and registered co-spatially within the uncertainty of the astrometry in each bandpass. Each panel shows the same $32''.5 \times 43''.7$ field of view. Labeled in each panel are the bandpass and telescope (upper left), and a scale bar indicating $5''$ (3.1 kpc). From the upper left to the lower right, each panel shows contours of the 6 cm radio continuum emission (Mazzarella et al. 1988) superposed on a grayscale representation of the following: (a) 20 cm radio continuum from the VLA; (b) $70 \mu\text{m}$ *Spitzer* MIPS; (c) $24 \mu\text{m}$ *Spitzer* MIPS; (d) $8 \mu\text{m}$ *Spitzer* IRAC; (e) $1.6 \mu\text{m}$ *HST* NICMOS; (f) I band ($0.81 \mu\text{m}$, F814W) *HST* ACS; (g) B band ($0.44 \mu\text{m}$, F435W) *HST* ACS; (h) U band ($0.35 \mu\text{m}$) *XMM-OM*; (i) X-rays ($0.4 - 2 \text{ keV}$) *Chandra*.

the SL data ($5.2\text{--}14.5 \mu\text{m}$). Further, the LL map did not completely cover the NE nucleus. A “total” SL+LL 1-d spectrum was extracted that contains most of the integrated emission of the system over $5\text{--}38 \mu\text{m}$ in a region 4×4 LL pixels in size (outlined in brown in Figure 10a). Another 1-d spectrum was extracted that fully covers both galaxies in the $5\text{--}14 \mu\text{m}$ SL spectrum in a region 13×13 SL pixels in size, where each pixel is $1''.8 \times 1''.8$. The resulting 1-d spectra, representing the sum of the emission from both galaxies, are presented in Figure 11 (SL+LL) and in Figure 12a (SL only), respectively. In addition, 1-d extractions from the SL map were constructed that provide a clean separation between the NE

and SW nuclei; these regions are shown as red and blue rectangles (each covering 5×5 SL pixels) in Figure 10a, and the resulting 1-d spectra are presented in Figures 12b and 12c. Due to the very high mid-infrared surface brightness of the galaxies, with a spatial resolution of $3''.6$ (two $1''.8$ pixels), even the SL spectral map does not enable a reliable separation of the nuclear emission from the diffuse emission surrounding the nuclei.

This is the first time mid-infrared spectra are available for each nucleus in Mrk 266 separately, as well as the integrated emission from both galaxies. Table 3 lists measured line fluxes and equivalent widths for the total system and, where possible, the individual galaxies.

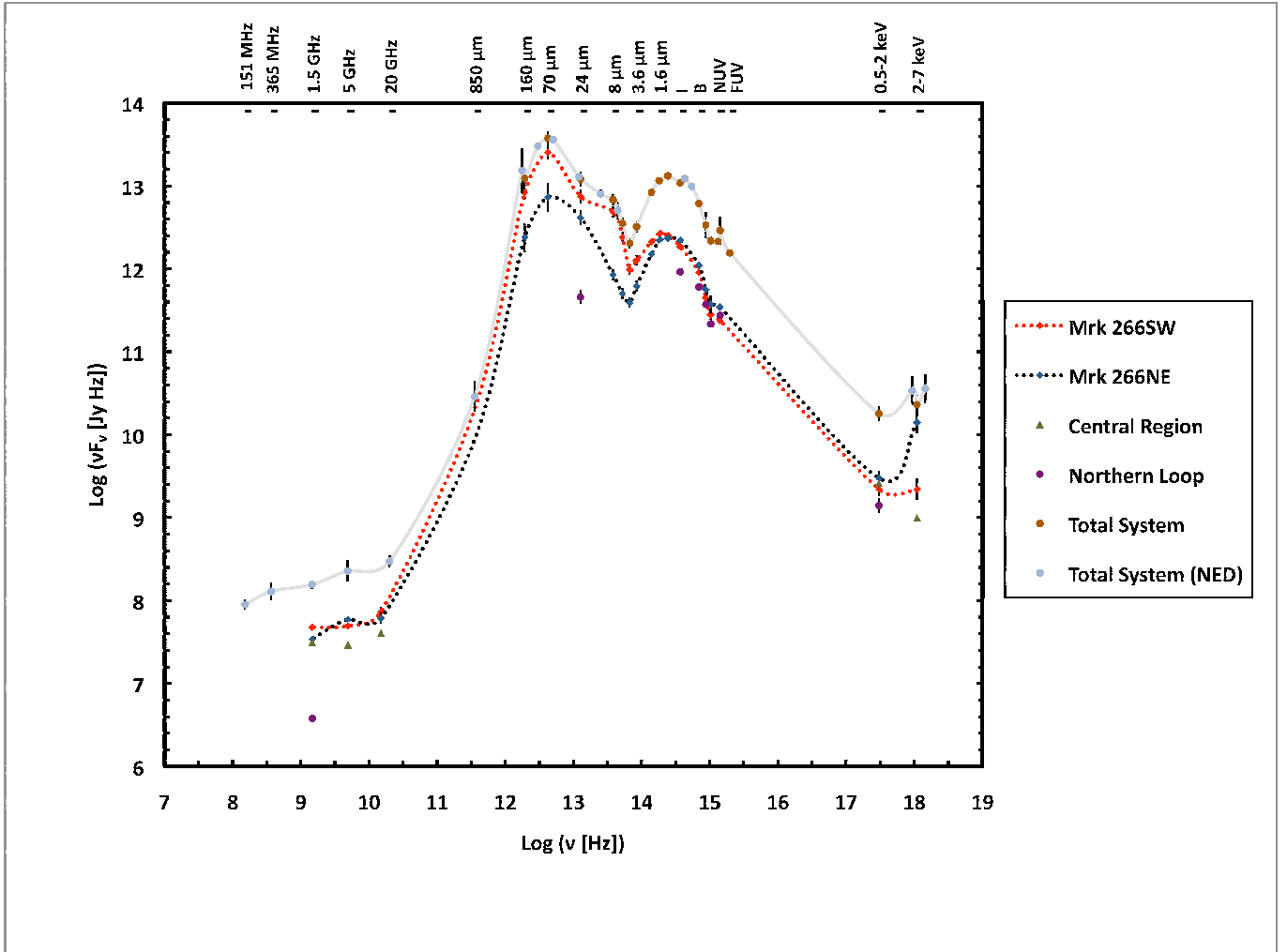


Figure 9. SEDs for Mrk 266 SW (red), Mrk 266 NE (blue), the Central Region (green) between the nuclei, the Northern Loop (purple), and the integrated emission from the Total System (brown). The legend shows the color coding used to identify the various components. Most of the photometric measurements are presented here for the first time and some data were selected from NED, as listed in Tables 12 and 13. The monochromatic fluxes plotted are computed via $\log(\nu f_\nu [\text{Jy Hz}])$. Conversions to other units are as follows: $\log(\nu f_\nu [\text{W m}^{-2}]) = \log(\nu f_\nu [\text{Jy Hz}]) - 26.00$; $\log(\nu L_\nu [\text{W}]) = \log(\nu f_\nu [\text{W m}^{-2}]) + 50.30$; $\log(\nu L_\nu [L_\odot]) = \log(\nu f_\nu [\text{W}]) - 26.58$.

The fluxes were converted from surface brightness units ($\text{W m}^{-2} \text{sr}^{-1}$) to W cm^{-2} by multiplying by the extraction aperture. Most of the spectral features in the SL+LL spectrum of the integrated emission from the galaxy pair (Fig. 11) were measured using the PAHFIT package (Smith et al. 2007), which includes decomposition of various spectral components and an extinction correction based on a fit with a $\tau_{9.7\mu\text{m}} = 0.30$ dust screen, corresponding to $A_V \approx 5.7$ mag. However, since the nuclei were resolved only in the SL data (Figure 12b and 12c), and PAHFIT produces most reliable continuum and feature fits when SL and LL are combined, we have used a spline-fitting technique (Hony et al. 2001; Peeters et al. 2002) to measure the SL features listed in Table 3 for the SW and NE galaxies. This further allows for direct comparison to other sources in the literature where this technique has been employed. Spline-fitting was also utilized for the PAH EQW measurements to estimate the local continuum and the silicate absorption strength. As noted by Smith et al. (2007), spline fitting systematically underestimates PAH fluxes compared to full spectral decomposition via PAHFIT. The various measurements are

identified in Table 3 with superscripts p (PAHFIT) and s (spline fitting), respectively.

3. ANALYSIS & DISCUSSION

Mrk 266 is a complex collection of many different physical subsystems, each of which are identified in Fig. 1 and discussed in the following subsections. At the macro level, Mrk 266 is clearly a merging system with two distinct AGNs coupled with strong spatial differences in current star formation, outflow, merger dynamics and AGN heating. But within that framework there are several specific questions that we can directly address using our multiwavelength data set: What are the structural parameters and underlying stellar populations of the two host galaxies? Is there evidence for dynamic outflow from each nucleus? Is the NE LINER a genuine AGN or is it powered by star formation? Is the origin of the observed diffuse emission tidal or due to galactic superwinds? What are the properties of the suspected star clusters that are forming in the merging system? Is Mrk 266 a unique dual AGN system, or are we observing a short-lived phase of an evolutionary process that commonly occurs when two massive, dusty disks merge?

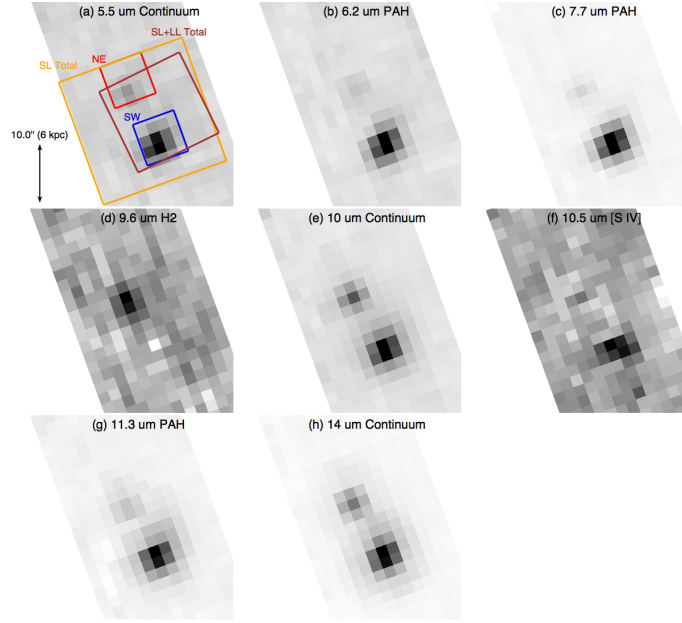


Figure 10. Image slices through the 2-d spectral IRS map. Panels (a) - (h) show images in the indicated spectral features (pure line or continuum emission). All images have north up and east left, and have the same scale indicated by the bar in panel (a). The colored rectangles overlaid on the $5.5 \mu\text{m}$ image in panel (a) indicate the regions of the 2-d spectral cube used to extract 1-d spectra. Brown box: “total” emission in the SL+LL modules plotted in Figure 11 (Mrk 266NE was not fully covered by the LL aperture); orange box: “total” emission from the SL module plotted in Figure 12a; red box: emission from the NE nucleus in the SL module plotted in Figure 12b; blue box: emission from the SW nucleus in the SL module plotted in Figure 12c.

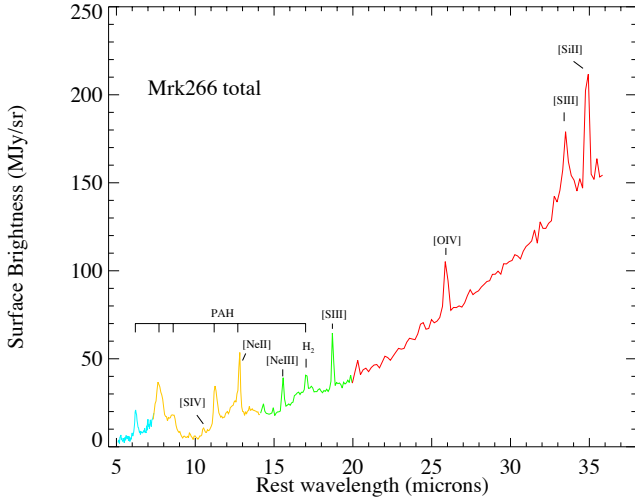


Figure 11. 1-d spectrum of Mrk 266 extracted from a low-resolution spectral map constructed from the SL and LL modules of the IRS. The region used to produce this spectrum is shown as a brown box in Figure 10. This is our best attempt to represent the integrated emission for both galaxies across the full $5\text{--}38 \mu\text{m}$ range covered by the low-resolution modules of the IRS, with the caveats noted in the text. The colors in this spectrum represent the various orders in the IRS instrument and are not related to the colors in Fig. 10.

3.1. Interacting/Merging Galaxies Revealed

3.1.1. Morphology and Bulge/Disk/Bar Decomposition

High resolution *HST* imagery (Fig. 1) has revealed a wealth of morphological structures within Mrk 266. At optical wavelengths (B and I) there are two distinct galaxies within a diffuse and highly asymmetric envelope. Patchy dust obscuration and clumpy star formation regions are evident on a variety of scales. The underlying structure of the two galaxies is best revealed in the NIC-

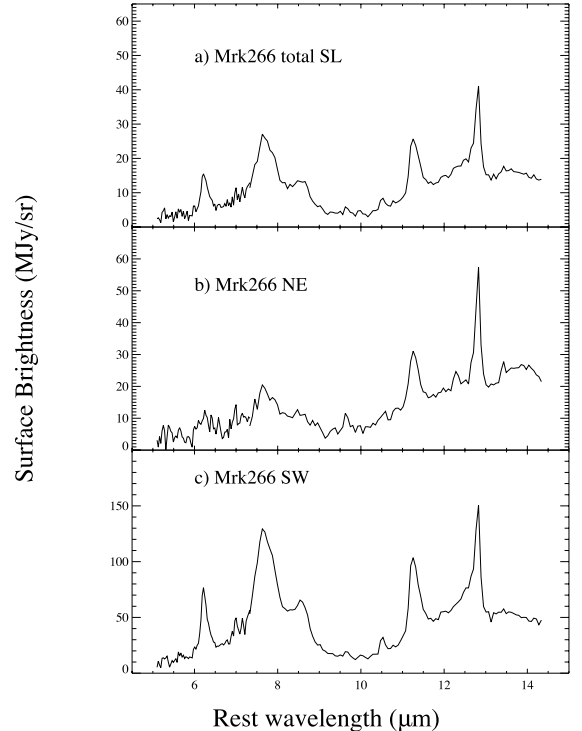


Figure 12. The spatial resolution of the SL observations permit a clean separation of the two galaxies that is not possible with the LL observations. Each panel is a 1-d extraction from the SL spectral map presented in Figure 10: (a) orange region covering the entire region; (b) red region containing Mrk 266 NE; (c) blue region containing Mrk 266 SW.

Table 3
Measurements from Low-Res Spectral Mapping

| Feature (1) | Flux (1×10^{-20} W cm $^{-2}$) (2) | EQW (μ m) (3) |
|-----------------------------------|--|---------------------------------|
| Mrk 266 Total ^a | | |
| 6.2 μ m PAH | 40.2 (± 1.8) ^P | 0.47(± 0.03) ^S |
| H ₂ S(5) 6.91 μ m | 0.66 (± 0.50) ^P | ... |
| [Ar II] 6.99 μ m | 2.34 (± 0.72) ^P | ... |
| 7.7 μ m PAH Complex | 163.0 (± 6.1) ^P | 0.46(± 0.02) ^S |
| 8.3 μ m PAH | 13.7 (± 1.8) ^P | ... |
| 8.6 μ m PAH | 26.8 (± 1.5) ^P | 0.15(± 0.01) ^S |
| [Ar III] 9.02 μ m | 0.80 (± 0.49) ^P | ... |
| H ₂ S(3) 9.65 μ m | 1.42 (± 0.38) ^P | ... |
| [S IV] 10.51 μ m | 1.59 (± 0.29) ^P | ... |
| 11.3 μ m PAH Complex | 31.9 (± 1.2) ^P | 0.51(± 0.01) ^S |
| 12.0 μ m PAH | 11.85 (± 0.83) ^P | ... |
| H ₂ S(2) 12.27 μ m | 0.89 (± 0.15) ^P | ... |
| 12.6 μ m PAH Complex | 23.78 (± 0.73) ^P | ... |
| [Ne II] 12.81 μ m | 6.78 (± 0.18) ^P | ... |
| 13.6 μ m PAH | 8.86 (± 0.70) ^P | ... |
| 14.2 μ m PAH | 2.80 (± 0.52) ^P | ... |
| [Ne III] 15.56 μ m | 3.57 (± 0.24) ^P | ... |
| 16.4 μ m PAH | 2.08 (± 0.38) ^P | ... |
| H ₂ S(1) 17.04 μ m | 1.61 (± 0.19) ^P | ... |
| 17 μ m PAH Complex | 19.4 (± 1.7) ^P | ... |
| 17.4 μ m PAH | 1.01 (± 0.36) ^P | ... |
| [S III] 18.71 μ m | 4.16 (± 0.28) ^P | ... |
| [O IV] 25.9 μ m | 4.52 (± 0.14) ^P | ... |
| [S III] 33.51 μ m | 3.71 (± 0.28) ^P | ... |
| [Si II] 34.86 μ m | 5.69 (± 0.39) ^P | ... |
| Mrk 266 SW ^b | | |
| 6.2 μ m PAH | 17.78 (± 0.35) ^S | 0.67(± 0.03) ^S |
| 7.7 μ m PAH Complex | 30.46 (± 0.35) ^S | 0.54(± 0.01) ^S |
| 8.6 μ m PAH | 5.45 (± 0.14) ^S | 0.17(± 0.01) ^S |
| [S IV] 10.51 μ m | 0.95 (± 0.13) ^S | ... |
| 11.3 μ m PAH Complex | 10.376 (± 0.088) ^S | 0.73(± 0.01) ^S |
| [Ne II] 12.81 μ m | 6.15 (± 0.99) ^S | ... |
| Mrk 266 NE ^b | | |
| 6.2 μ m PAH | 2.418 (± 0.019) ^S | 0.4 (± 0.1) ^S |
| 7.7 μ m PAH Complex | 2.86 (± 0.28) ^S | 0.25(± 0.03) ^S |
| 8.6 μ m PAH | 0.69 (± 0.11) ^S | 0.10(± 0.02) ^S |
| H ₂ S(3) 9.65 μ m | 0.52 (± 0.14) ^S | ... |
| 11.3 μ m PAH Complex | 2.170 (± 0.078) ^S | 0.34(± 0.02) ^S |
| H ₂ S(2) 12.27 μ m | 0.308 (± 0.063) ^S | ... |
| [Ne II] 12.81 μ m | 1.84 (± 0.29) ^S | ... |

^a Spectral measurements for the integrated emission from both galaxies in Mrk 266. Features in the 5.2-14.5 μ m (SL) and 14.5-38 μ m (LL) regions were measured from the 1-d spectrum plotted in Figure 11; this region is 4x4 LL pixels in size, where each pixel is 5''1 x 5''1, as outlined in brown in Figure 10(a).

^b Spectral features measured from the SL spectra of Mrk 266 SW and NE as plotted in Figure 12c and 12b. These 1-d spectra were extracted from the blue and red regions of the spectral map shown in Figure 10, which have dimensions of 5x5 SL pixels, where each pixel is 1''8 x 1''8. ^P These line fluxes were measured using PAHFIT and include an extinction correction based on a fit with a $\tau_{9.7\mu m} = 0.30$ dust screen, which corresponds to $A_V \approx 5.7$ mag.

^S EQW measurements for the PAH features were measured using a spline-fitting technique for estimating the local continuum. Spline fitting was also used to estimate fluxes of features in the SL spectra of the individual galaxies which could not be measured with PAHFIT. See text for details.

MOS H band image. The SW galaxy (Fig. 13) is a barred spiral with two arms and predominant dust features, and the estimated Hubble type is SBb (pec). The NE galaxy (Fig. 14) has no discernible spiral arms and appears to be Hubble type S0 or S0/a (pec).

Table 4
GALFIT Results

| Band (1) | $\frac{f}{f_{\text{tot}}}$ (%) (2) | C(n) (3) | $\frac{B}{D}$ (4) | r_e (5) | $\frac{b}{a}$ (6) | PA $^\circ$ (7) | mag _{AB} (8) |
|------------------------------------|---------------------------------------|-------------|----------------------|--------------|----------------------|--------------------|--------------------------|
| Mrk 266 SW ^a | | | | | | | |
| 0.44 μ m | 68.2 | B(4) | ... | 9.99 | 0.79 | -38 | ... |
| 0.44 μ m | 68.2 | T | ... | ... | ... | ... | 14.40 \pm 0.02 |
| 0.81 μ m | 63.0 | B(4) | ... | 8.28 | 0.79 | -19 | ... |
| 0.81 μ m | 63.0 | T | ... | ... | ... | ... | 13.13 \pm 0.01 |
| 1.6 μ m | 41.8 | B(4) | ... | 4.92 | 0.49 | -13 | ... |
| 1.6 μ m | 9.6 | D(1) | 0.23 | 2.45 | 0.74 | -88 | ... |
| 1.6 μ m | 2.4 | b | ... | 0.57 | 0.27 | -9 | ... |
| 1.6 μ m | 0.0 | P | ... | ... | ... | ... | ... |
| 1.6 μ m | 53.8 | T | ... | ... | ... | ... | 12.55 \pm 0.03 |
| Mrk 266 NE ^b | | | | | | | |
| 0.44 μ m | 31.8 | D(1) | ... | 3.11 | 0.70 | -91 | ... |
| 0.44 μ m | 31.8 | T | ... | ... | ... | ... | 15.23 \pm 0.02 |
| 0.81 μ m | 13.9 | B(4) | ... | 1.43 | 0.60 | -113 | ... |
| 0.81 μ m | 23.1 | D(1) | 0.58 | 3.98 | 0.69 | -63 | ... |
| 0.81 μ m | 37.0 | T | ... | ... | ... | ... | 13.71 \pm 0.02 |
| 1.6 μ m | 46.1 | B(4) | ... | 3.46 | 0.81 | -113 | ... |
| 1.6 μ m | 0.2 | P | ... | 0.00 | 1.00 | 0 | ... |
| 1.6 μ m | 46.3 | T | ... | ... | ... | ... | 12.71 \pm 0.03 |
| Mrk 266 Total (SW+NE) ^c | | | | | | | |
| 0.44 μ m | 1.0 | T | ... | ... | ... | ... | 13.97 \pm 0.02 |
| 0.81 μ m | 1.0 | T | ... | ... | ... | ... | 12.60 \pm 0.02 |
| 1.6 μ m | 1.0 | T | ... | ... | ... | ... | 11.88 \pm 0.04 |

Note. — Fitting parameters and results of modeling the HST data using GALFIT. Column (1): HST Filter: B = F435W (0.44 μ m); I = F814W (0.81 μ m); H = F160W (1.6 μ m). Column (2): Percentage of the total flux of the GALFIT model of the *galaxy pair* accounted for by the indicated component of the model image at 0.44, 0.81 or 1.6 μ m. Column (3): Model components coded as follows: B=Bulge (Sersic index n=4); D=Disk (Sersic index n=1); b=bar; P=Point source based on Tiny Tim Krist (1993); T = Total flux from all GALFIT components for the galaxy. Column (4): Bulge-to-Disk ratio. Column (5): Effective radius of the Seric fit (kpc units). Column (6): Axis ratio of the component fit. Column (7): Position angle of the component fit (degrees east of north). Column (8): Apparent AB magnitude of the sum of the GALFIT model components for each galaxy, where $f_\nu(Jy) = 10^{0.4(8.9-m_{AB})}$. Conversions between the AB and Vega systems (<http://www.stsci.edu/hst/acs/analysis/zeropoints/>) are as follows: $B_{AB} - B_{Vega} = -0.11$; $I_{AB} - I_{Vega} = 0.42$; $H_{AB} - H_{Vega} = 1.32$.

^a The 1.6 μ m image of Mrk 266 SW is modeled as the sum of Pointsource + Bar + Disk (n = 1) + Bulge (n = 4) components. The 0.44 and 0.81 μ m images are too confused by extinction and H II regions to derive reliable models of the underlying stars; simple Bulge (n = 4) models were fit at these wavelengths only to examine the residual images for fine structure in the star-forming regions (Fig. 16).

^b The 1.6 μ m image of Mrk 266 NE is modeled as the sum of Pointsource + Bulge (n = 4) components; there are no significant Bar or Disk components detected for this galaxy.

^c The total flux (apparent magnitude) accounted for in the GALFIT model for the galaxy pair in each *HST* passband.

In the extremities of the system are three notable features at optical wavelengths (Fig. 1): (1) Extending $\sim 25''$ (15 kpc) to the north is a fragmented, filamentary feature known as the Northern Loop; this structure is examined in detail in §3.4. (2) Faint emission extending $\sim 60''$ (36 kpc) to the south and $\sim 40''$ (24 kpc) to the south-east from the center of the system appears to be tidal debris. The deep B+V+I image (Fig. 2) reveals much fainter, asymmetric emission spanning ≈ 103 kpc (2'.9). The peculiar morphology and vast extent of this emission are consistent with numerical simulations

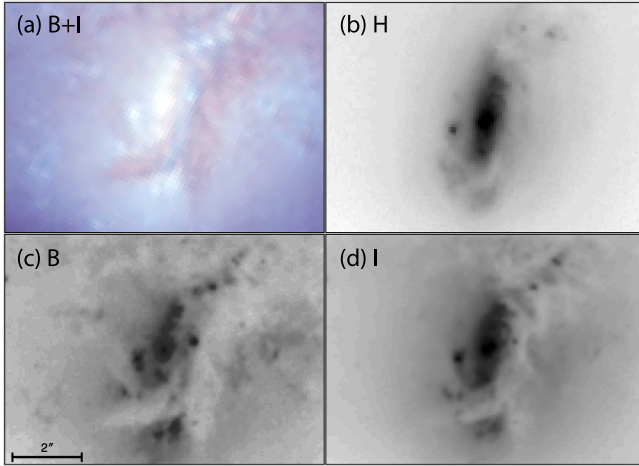


Figure 13. A close-up of HST imagery of Mrk 266 SW showing a color composite of ACS B+I bands (a); NICMOS H band (b); ACS B band (c); and ACS I band (d). The images are displayed with an emphasis on the high surface brightness emission near the nucleus. The spatial resolution is very similar in all 4 bands, but there has been no PSF matching. The scale bar indicates $2''$.

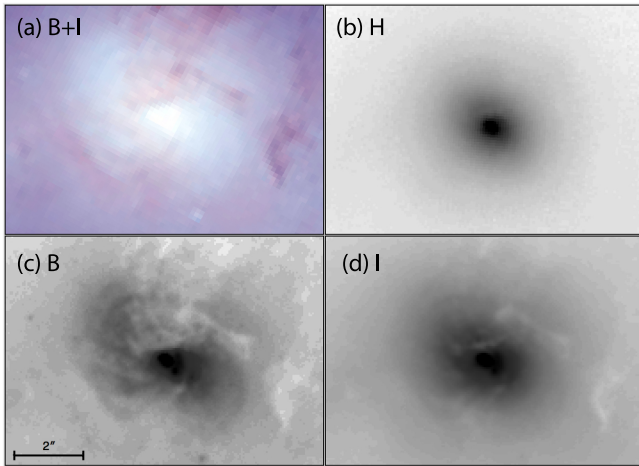


Figure 14. HST imagery of Mrk 266 NE displaying the same bands as in Figure 13.

of tidal debris created during a major merger (e.g., Mihos 1999; Cox et al. 2006). (3) Approximately $25''$ to the south-west are two objects that could be either knots near the end of a tidal tail or background galaxies. The latter interpretation is favored due to what appear to be compact nuclei and spiral arms. If these are background galaxies with similar physical size and separation as Mrk 266, their projected diameters ($\approx 3''$) and separation ($\approx 2''$) imply they are ~ 5 times further away than Mrk 266 (distance ~ 650 Mpc, $z \sim 0.15$); redshift measurements are needed for confirmation.

Using GALFIT (Peng et al. 2002), quantitative isophotal analysis was performed on both component galaxies in the three *HST* bands. At $1.6 \mu\text{m}$ (H band) where dust obscuration is minimal and thus permits the most reliable decomposition of the underlying galaxies, various trial fits involving possible point source, bulge, disk and/or bar components were made; potential nuclei were modeled using a point spread function generated from the Tiny Tim package (Krist 1993)²³. Figure 15 shows

²³ <http://www.stsci.edu/software/tinytim/tinytim.html>

the components of the best-fitting models in the H band. Due to extensive, patchy dust obscuration and complex star-forming regions, only models with possible bulge and disk components were considered in the B and I bands. Subtraction of the best-fitting models from the direct images are useful to elucidate further fine structures, as shown visually for all three bands in Figure 16. The results of this structural analysis at H band are the following: a) The SW galaxy has no detected point source emission; its nucleus is therefore obscured by dust even at $1.6 \mu\text{m}$. b) The NE galaxy exhibits no significant disk component and therefore can be modeled using only a point source plus bulge profile. c) Approximately 10% of the total H-band light is in the form of diffuse emission which is likely tidal in origin (Fig. 15a). In the optical bands the residual images reveal the following: a) The SW galaxy has many knots of emission which are likely star clusters or associations; these features are analyzed in detail in §3.6. b) The largest features in the B-band residual image appear to be giant star-forming regions (superassociations) situated on both ends of the stellar bar. This phenomenon, in which superassociations occur on both sides of stellar bars much more frequently than they occur on a single side, was pointed out by Magtesian & Khachikian (1991). c) The NE galaxy has numerous radial, asymmetric filaments (most pronounced in the B band) indicative of bi-conical outflow from the AGN; this region is analyzed more fully in §3.2.4. Parameters from the GALFIT modeling are listed in Table 4. Adopting a distance modulus of 35.55 mag (see §1.3), the apparent H magnitudes (Vega system) of Mrk 266 SW and NE (Table 4) correspond to remarkably similar absolute magnitudes of $M_H(\text{SW}) = -24.32$ and $M_H(\text{NE}) = -24.16$.

3.1.2. Galaxy Luminosities and Derived Stellar Masses

The H-band ($1.6 \mu\text{m}$) luminosity function of galaxies in the Coma Cluster has been approximated as a Schechter function with $L_H^* = -23.9$ mag (de Propris et al. 1998). Therefore, Mrk 266 SW and NE are $\approx 50\%$ and 30% more luminous than the typical L_H^* galaxy in the local universe. Applying the mean mass-to-light ratio at H-band of 4.6 (M_\odot/L_\odot) for spiral galaxies (including early types S0 and S0/a; Gavazzi et al. (1996)) results in total galaxy mass estimates of $6.3 \times 10^{10} M_\odot$ (SW) and $5.3 \times 10^{10} M_\odot$ (NE). Estimates of the stellar mass in old stars derived from the mean ratio of $M_*/\nu L_\nu(2.2\mu\text{m}) = 5.6(\pm 1.5)$ based on model predictions by Lacey et al. (2008) produces similar results of $M_* = 6.1 \times 10^{10} M_\odot$ (SW) and $M_* = 4.4 \times 10^{10} M_\odot$ (NE).²⁴ SED model fitting can improve on stellar masses estimated from monochromatic luminosities U et al. (2011). Next we turn attention to the nuclei and their circumnuclear regions.

²⁴ The model curve for $z = 0$ galaxies in Figure 13c of Lacey et al. (2008), adjusted to $h = 0.70$, corresponds to a range of 4.5 - 7.0 in $M_*/\nu L_\nu(2.2\mu\text{m})$. A significantly lower ratio of $M_*/L_{2.2\mu\text{m}} \approx 1$ was found by Arnouts et al. (2007) and Cole et al. (2001). The nature of this discrepancy is beyond the scope of this article.

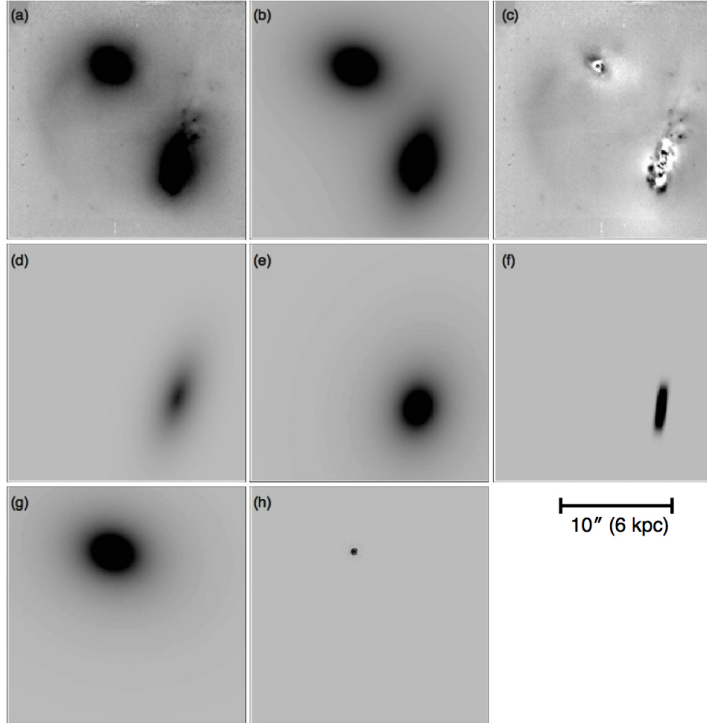


Figure 15. Results of GALFIT modeling of the $1.6 \mu\text{m}$ NICMOS image of Mrk 266. The top row shows (a) the direct image, (b) the GALFIT model fit, and (c) the residual image (direct image minus model fit). The center row shows the components of the model for the SW galaxy: (d) the disk, bulge (e), and stellar bar (f). The bottom row shows the components of the model for the NE galaxy: (g) the bulge and (h) the point source modeled with Tiny Tim. The scale bar indicates $10''$ (6 kpc).

3.2. The Nuclei and Circumnuclear Regions

3.2.1. Optical and Infrared Spectral Diagnostics

Using optical emission-line diagnostics, the NE nucleus has been classified as a LINER and the SW nucleus as a Seyfert 2 (e.g., Hutchings et al. 1988; Mazzarella & Boroson 1993; Ishigaki et al. 2000). At optical wavelengths, the NE nucleus has brighter continuum emission and less extinction than the SW nucleus. Yuan et al. (2010) classified Mrk 266 NE as a composite AGN/starburst nucleus, and they concluded that the NE and SW nuclei have similar relative AGN and starburst contributions within the LINER and Seyfert 2 branches of the $[\text{O III}]5007/H\beta$ vs. $[\text{O I}]6300/H\alpha$ diagnostic diagram.²⁵ Since the IRS apertures encompass an area of $5.4 \times 5.4 \text{ kpc}^2$ (Fig. 10), whereas published optical diagnostics were obtained through smaller apertures of $\sim 1 \times 1 \text{ kpc}^2$, nuclear emission is more diluted by extranuclear emission in the mid-IR spectra than in the optical spectra. However, since the mid-IR spectra penetrate much more dust than the optical spectra, if there is sufficient centrally concentrated dust heated by an embedded AGN, this emission can potentially overpower the extended star formation (as in many ULIRGs). The IRS spectra of the two nuclei (Fig. 12) show them to be similarly dominated by PAH emission, and the large PAH equivalent widths

²⁵ The identifications of the NE and SW nuclei of Mrk 266 were mistakenly swapped in the tables and figures of Kim et al. (1995) and Veilleux et al. (1995), and thus also in Table 2 of Yuan et al. (2010). The identifications are corrected here.

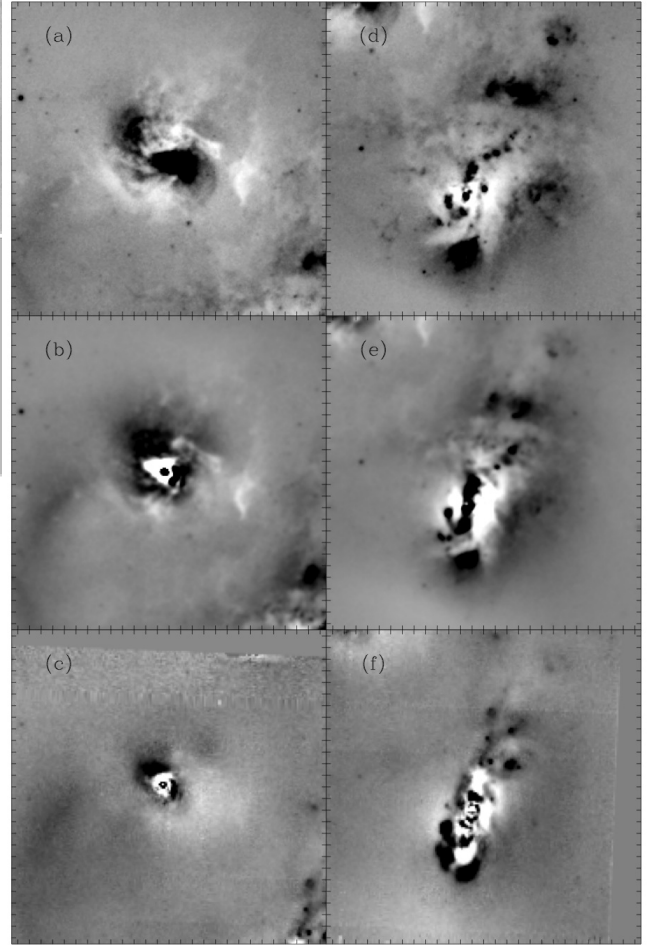


Figure 16. Residuals resulting from subtraction of GALFIT models parameterized in Table 4 from the direct HST images. The left column shows results for the NE galaxy at $0.44 \mu\text{m}$ (a), $0.81 \mu\text{m}$ (b) and $1.6 \mu\text{m}$ (c). The right column shows results for the SW galaxy at $0.44 \mu\text{m}$ (d), $0.81 \mu\text{m}$ (e) and $1.6 \mu\text{m}$ (f). Black (white) regions represent positive (negative) flux with respect to the image model fits. The tick marks are separated by $0''.5$.

(Table 3) indicate the prominence of star-formation (e.g., Armus et al. 2007). The NE source has lower PAH fluxes and equivalent widths, indicating excess warm dust emission compared to the SW source.

The $6.2 \mu\text{m}$ PAH EQWs and $9.7 \mu\text{m}$ silicate absorption strengths²⁶ place the SW galaxy on the bottom right vertex of the silicate depth versus PAH EQW plot of Spoon et al. (2007), a region dominated by galaxies with high star formation rates; the NE galaxy (with similar Si strength but a lower $6.2 \mu\text{m}$ EQW of $0.4 \mu\text{m}$ compared to $0.67 \mu\text{m}$ for the SW galaxy) is in a region populated with AGN and ULIRGs having substantial dust heating by non-stellar radiation. The observed silicate strength in the SW galaxy (-0.60 ± 0.06) is intermediate between the values observed for the face-on galaxy NGC 7714 and the edge-on galaxy M82, which is consistent with the derived disk axial ratio of $\approx 42^\circ$ for Mrk 266 SW

²⁶ The empirical method of Spoon et al. (2007) was applied to the SL spectrum ($5\text{--}14 \mu\text{m}$ region; Fig. 12) to measure silicate strengths of $-0.62 (\pm 0.06)$, $-0.69 (\pm 0.12)$, and $-0.66 (\pm 0.07)$ for the SW nucleus, the NE nucleus, and the total system, respectively. A similar absorption strength, $-0.60 (\pm 0.06)$, was measured using the $5\text{--}40 \mu\text{m}$ SL+LL data for the total system (Fig. 11).

Table 5
Estimated AGN Contributions to the Mid-Infrared and Bolometric Luminosity

| Diagnostic (1) | SW Galaxy | | | NE Galaxy | | | Total System | | |
|---|--------------|---|--|--------------|---|--|--------------|---|---|
| | Value (2) | $\frac{L_{\text{AGN}}}{L_{\text{Diag}}}$ (3) | $\frac{L_{\text{AGN}}}{L_{\text{Bol}}}$ (4) | Value (5) | $\frac{L_{\text{AGN}}}{L_{\text{Diag}}}$ (6) | $\frac{L_{\text{AGN}}}{L_{\text{Bol}}}$ (7) | Value (8) | $\frac{L_{\text{AGN}}}{L_{\text{Diag}}}$ (9) | $\frac{L_{\text{AGN}}}{L_{\text{Bol}}}$ (10) |
| (1) $[\text{O IV}] 25.89\mu\text{m}/[\text{Ne II}] 12.81\mu\text{m}^{\text{a}}$ | 0.93 | 23% | 73% | ... | ... | ... | 0.67 | 17% | 64% |
| (2) $[\text{Ne V}] 14.32\mu\text{m}/[\text{Ne II}] 12.81\mu\text{m}^{\text{a}}$ | 0.14 | 11% | 53% | ... | ... | ... | ... | ... | ... |
| (3) PAH $6.2\mu\text{m}$ EQW $[\mu\text{m}]^{\text{b}}$ | 0.67 | 0% | ... | 0.4 | 30% | ... | 0.47 | 10% | ... |
| (4) PAH $7.7\mu\text{m}$ EQW $[\mu\text{m}]^{\text{b}}$ | 0.54 | 69% | 43% | 0.25 | 79% | 56% | 0.46 | 71% | 46% |
| (5) $f(\text{PAH } 6.2\mu\text{m})/f_{5.5\mu\text{m}}$ vs. $f(15\mu\text{m})/f_{5.5\mu\text{m}}^{\text{b}}$ | 1.6, 8.6 | 47% | 9% | 0.56, 6.4 | 81% | 33% | 2.0, 2.9 | 52% | 11% |
| (6) $f_{\nu}(30)/f_{\nu}(15)^{\text{c}}$ | 3.9 | 89% | 82% | 3.3 | 92% | 87% | 4.8 | 85% | 76% |
| Mean ^d | | 40% | 52% | | 71% | 59% | | 47% | 49% |
| Std. Dev. | | 35% | 29% | | 28% | 27% | | 33% | 28% |

Note. — Column (1): Mid-infrared spectral diagnostic used to estimate the fractional contribution of radiation from an AGN. Columns (2)-(4): For the SW galaxy, the value of the diagnostic followed by the percentage of AGN contribution to the diagnostic luminosity and the estimated percentage of AGN contribution to L_{bol} . The latter uses the zero-points and bolometric corrections from Veilleux et al. (2009); see §3.2.1. Columns (5)-(7): The same as columns (2)-(4), but for the NE galaxy. Columns (8)-(10): The same as columns (2)-(4), but for the total system.

^a Based on published high-resolution, staring-mode data (Appendix Table 14). The NE nucleus was not fully covered in these observations.

^b Based on new low-resolution measurements from the IRS spectral map (Table 3).

^c The continuum flux density ratio estimated via interpolation in the SED of the global system, $f_{\nu}(30\mu\text{m})/f_{\nu}(15\mu\text{m}) = 4.8$, is within 8% of the value $f_{\nu}(30\mu\text{m})/f_{\nu}(15\mu\text{m}) = 5.4$ computed from the *IRS* (SL+LL) spectrum. Given this close agreement, since the 15 and 30 μm fluxes could not be measured for the individual galaxies with the *IRS* (because they were unresolved by the LL module), the flux ratios estimated by interpolation from the broad-band photometry in the SEDs for the individual galaxies (Table 13) were substituted.

^d The mean $L_{\text{AGN}}/L_{\text{Bol}}$ values omit the $6.2\mu\text{m}$ PAH EQW because there is no bolometric correction available for this diagnostic.

(Table 4). The observed silicate absorption strengths correspond to $N_{\text{H}} = 2.2 \times 10^{22}$ and $2.4 \times 10^{22} \text{ cm}^{-2}$ for the SW and NE nuclei, respectively; these values result from applying the relationships $N_{\text{H}} = \tau_{9.7\mu\text{m}} \times 3.5 \times 10^{22} \text{ cm}^{-2}$ and $A_{9.7\mu\text{m}}/A_{\text{v}} = 0.06$ (Roche & Aitken 1984). However, for clumpy dust configurations expected in AGN tori, emission and absorption cannot be disentangled along the line of sight and therefore these are lower limits to the true silicate column to the central sources.

Various empirical diagnostics have been published to quantify the relative contributions to dust heating from AGN and starburst sources (e.g., Armus et al. 2007). We focus primarily on the suite of methods applied to local ULIRGs and QSOs by Veilleux et al. (2009), including application of their bolometric corrections to express the estimated AGN dust heating contributions as a fraction of L_{bol} . All methods assume that the line emitting regions are subject to the same amount of extinction within the aperture, which may be questionable, especially for Mrk 266 SW. Since the NE galaxy was not observed in the high-resolution IRS mode, methods that involve the fine structure lines can only be applied to the SW galaxy. The results are summarized in Table 5. For the SW galaxy, the $[\text{O IV}]/[\text{Ne II}]$ ratio indicates an overall AGN contribution to L_{bol} of 73%, whereas the $[\text{Ne V}]/[\text{Ne II}]$ ratio suggests 53%. The $6.2\mu\text{m}$ EQW indicates that the mid-IR luminosity of the SW component is due entirely to a starburst, and a 30% AGN contribution is inferred for the NE galaxy. This diagnostic suggests a 10% AGN contribution to the mid-IR luminosity of the total system.²⁷ The AGN fractions estimated from the $6.2\mu\text{m}$ EQW are substantially lower than those obtained using the EQW of the $7.7\mu\text{m}$ PAH feature (see Table 5). This discrepancy may be due to greater difficulty measuring

the $7.7\mu\text{m}$ PAH feature because of confusion from surrounding features ($8.6\mu\text{m}$ PAH and silicate absorption) and complications in defining the proper continuum level.

The continuum shape over 3-16 μm provides another diagnostic. The physical basis is that dust grains located near an AGN can reach temperatures as high as 500-1000 K (before they sublimate), and such high dust temperatures would completely dominate the continuum emission compared to dust heated by a starburst. This method was developed by Laurent et al. (2000), adapted by Peeters et al. (2004) for interpretation of mid-IR spectra from the *Infrared Space Observatory* (*ISO*), and modified further for *Spitzer* IRS data by Armus et al. (2007). Continuum fluxes in the relevant passbands were combined with the $6.2\mu\text{m}$ PAH fluxes, and the formulation of Veilleux et al. (2009) was used to compute AGN fractions before and after bolometric corrections. The results suggest $L_{\text{AGN}}/L_{\text{bol}}$ is 33% for the NE galaxy, but only about 10% for the SW galaxy and the total system. The continuum flux density ratio $f_{\nu}(30\mu\text{m})/f_{\nu}(15\mu\text{m})$ provides our final empirical diagnostic; Veilleux et al. (2009) found this to be an effective substitute for the PAH-free and silicate-free MIR/FIR ratio.

On average, with a standard deviation of nearly 30%, these diagnostics indicate approximately equal contributions of AGN and starburst heating of the dust in both galaxies (Table 5). This is similar to the average AGN contribution to L_{bol} found for ULIRGs in the QUEST sample with Seyfert 2 spectral classifications (Veilleux et al. 2009). The variation in these diagnostics may be due, in part, to the different optical depths probed by different wavelengths.

Finally, there is a significant difference in the PAH properties of the galaxies. The modeling of Draine & Li (2001) combined with the ratios of the PAH features ($f_{11.3\mu\text{m}}/f_{7.7\mu\text{m}}$ and $f_{6.2\mu\text{m}}/f_{7.7\mu\text{m}}$) indicate a dominance of relatively warm, ionized PAHs in the SW component

²⁷ The CAFE SED fitting package provides an independent, model-dependent estimate of the AGN contribution to the total infrared luminosity. See §3.5.

and cooler, neutral PAHs in the NE component. The PAH line flux ratios for the total system reflect the fact that the SW galaxy dominates the total mid- and far-infrared emission from Mrk 266. The $f_{11.3\mu\text{m}}/f_{7.7\mu\text{m}}$ PAH ratio in Mrk 266 NE (0.76) is substantially larger than the ratio in the SW galaxy (0.34). The former is similar to the ratios observed in other galaxies containing AGNs, and the latter is near the mean value (0.25) observed in galaxies with pure starburst (H II) spectra (Smith et al. 2007). Following the inferences proposed by Smith et al., this suggests that the hard radiation field surrounding the partially obscured AGN in the NE galaxy may be preferentially destroying PAH molecules small enough to emit at $7.7\ \mu\text{m}$, thus increasing the $11.3\mu\text{m}/7.7\mu\text{m}$ PAH ratio compared to the SW nucleus which has a more heavily obscured AGN and a higher star formation rate.

3.2.2. Warm Molecular Gas

In the NE galaxy, the IRS spectral maps (Figs. 10 and 12) reveal bright rotational lines of molecular hydrogen, specifically $H_2\ S(3)\ 9.7\mu\text{m}$ and $H_2\ S(2)\ 12.3\mu\text{m}$. In the SW galaxy, the $H_2\ S(3)\ 9.7\mu\text{m}$ emission is much weaker, and any $H_2\ S(2)\ 12.3\ \mu\text{m}$ emission that may be present intrinsically is overshadowed by the blue wing of the strong $12.6\ \mu\text{m}$ PAH complex. In contrast, the SW galaxy has bright [S IV] $10.51\ \mu\text{m}$ emission, whereas the NE nucleus is undetected in this feature. Give that the NE galaxy has 8 and $24\ \mu\text{m}$ flux densities that are 1.8 and 5.7 times fainter than the SW galaxy (see Table 13 and Fig. 9), it is surprising that the H_2 line emission in Mrk 266 NE is substantially more luminous than in Mrk 266 SW. This suggests that the majority of the detected H_2 line emission in the NE galaxy has a different origin than in the SW galaxy. A prime candidate for the enhanced H_2 emission in Mrk 266 NE is shock excitation.

Analysis of near-infrared spectra of Mrk 266 led Davies et al. (2000) to conclude that fast C shocks ($v_s \sim 40\ \text{km s}^{-1}$) are responsible for $\approx 70\%$ of the $H_2\ 1-0\ S(1)$ emission in the two nuclei, with fast J shocks ($v_s \sim 300\ \text{km s}^{-1}$) and UV fluorescence responsible for the remaining $\approx 30\%$. Davies et al. demonstrated that the powerful radio continuum and $1-0\ S(1)$ emissions observed in Mrk 266 NE cannot be explained with pure starburst models, and they are likely generated predominantly by shocks. Furthermore, the presence of $1-0\ S(1)$ emission extended out to $\sim 1\ \text{kpc}$ from the NE nucleus, with a large equivalent width and low $S(1)/B\gamma$ ratio that rule out star formation, provides additional evidence that the H_2 emission is excited by spatially extended shocks. Davies et al. speculated that Mrk 266 NE may itself be a very close pair of galactic nuclei with shocked molecular gas settled between them, as observed in NGC 6240. Our interpretation of the latest data from *Spitzer*, *HST* and *Chandra* favors an AGN-driven outflow as the origin of strong shocks in Mrk 266 NE (see §3.2.4).

3.2.3. AGN Black Hole Masses

Marconi & Hunt (2003) established an empirical relation between H-band bulge luminosity and nuclear black hole mass. Combining measurements of the total H-band absolute magnitudes with the GALFIT image decomposition results showing that 78% and 99% of the total H-band light is in the bulge components

of the SW and NE galaxies (§3.1.1), the calibration of Marconi & Hunt (Group 1 Galaxies) yields black hole masses of 2.3×10^8 (SW) and $2.6 \times 10^8\ M_\odot$ (NE). An independent diagnostic is available from the high-ionization, mid-IR emission lines detected in Mrk 266 SW. Using the approach of Dasyra et al. (2008), the [Ne V] $14.32\mu\text{m}$ ([O IV] $25.89\mu\text{m}$) emission line luminosity of $1.58\ (10.5) \times 10^{41}\ \text{erg s}^{-1}$ computed from published high-resolution *IRS* measurements (Appendix Table 14) corresponds to $M_{\text{BH}} = 1.7\ (3.2) \times 10^8\ M_\odot$ for the SW nucleus, which is consistent with the IR photometry. The inferred black hole masses are therefore in the typical range known to power other luminous AGNs.

3.2.4. Evidence for Nuclear Outflows and Shocks

In the previous section the radiation field heating the dust in the two nuclear environments was established. In this section evidence is presented for dynamical outflows from the nuclei. Within a radius of $2''$ (1.2 kpc) around the NE nucleus (Figs. 14c,d and 16a), the *HST* optical imaging reveals structure that is strongly suggestive of a bi-conical outflow with patchy dust extinction. Evidence for this interpretation rather than spiral arms is as follows: (a) Multiple filamentary structures extend radially and asymmetrically from the nucleus rather than in a symmetric spiral pattern. (b) There is the lack of improved definition in any spiral arm pattern in the I-band image relative to B-band. (c) Photometric deconvolution (§3.1.1) indicates the NE galaxy is bulge-dominated. There are also conspicuous knots of concentrated emission along a concave arc located $0.4\ \text{W}$ of the nucleus. Table 6 lists photometric measurements of the 3 most prominent optical knots. The individual knot luminosities of $L_B \approx 3 \times 10^8\ L_\odot$ are substantially higher than other luminous star clusters in Mrk 266 (see §3.6, Fig. 27), and their orientation in an arc embedded within a triangular bow-like structure suggests they may be energized by an AGN-driven outflow in a situation similar to M51 (Cecil 1988) rather than by unusually massive star clusters.

A comparison of the B-band emission with published high-resolution 18 cm radio continuum observations (Thean et al. 2001) is shown in Figure 17. The 18 cm MERLIN map exhibits limb-brightening at the location of the optical arc and knots $0''.4$ (240 pc) west of the nucleus, and a secondary radio continuum peak is located $0''.6$ (360 pc) NE of the nucleus. An axis at position angle 56° intersects the radio/optical nucleus, the radio emission $0''.6$ NE of the nucleus, and B-band knots situated $0''.4$ and $0''.9$ SW of the nucleus. Bi-conical AGN outflows with aligned radio continuum and optical emission-line radiation with dimensions of $\lesssim 1\ \text{kpc}$ are commonly observed in Seyfert galaxies and in some LINERS, especially those that are nearly face-on such as NGC 1068 and M51. (See, for example, the review of Veilleux et al. (2005).) The optical morphology of the NE nuclear environment is remarkably similar to the radiative bow shock observed $5''$ (230 pc) south of the nucleus of M51, which is also a LINER (Cecil 1988; Ford et al. 1985).

The combined data suggest that the AGN in Mrk 266 NE is ejecting radio-emitting plasma along an axis with $\text{PA} \approx 56^\circ$, which is also aligned with a bi-conical ionization cone that extends to a radius of 1.2 kpc from the nucleus. The 6 cm radio power ($4.2 \times 10^{22}\ \text{W Hz}^{-1}$) and

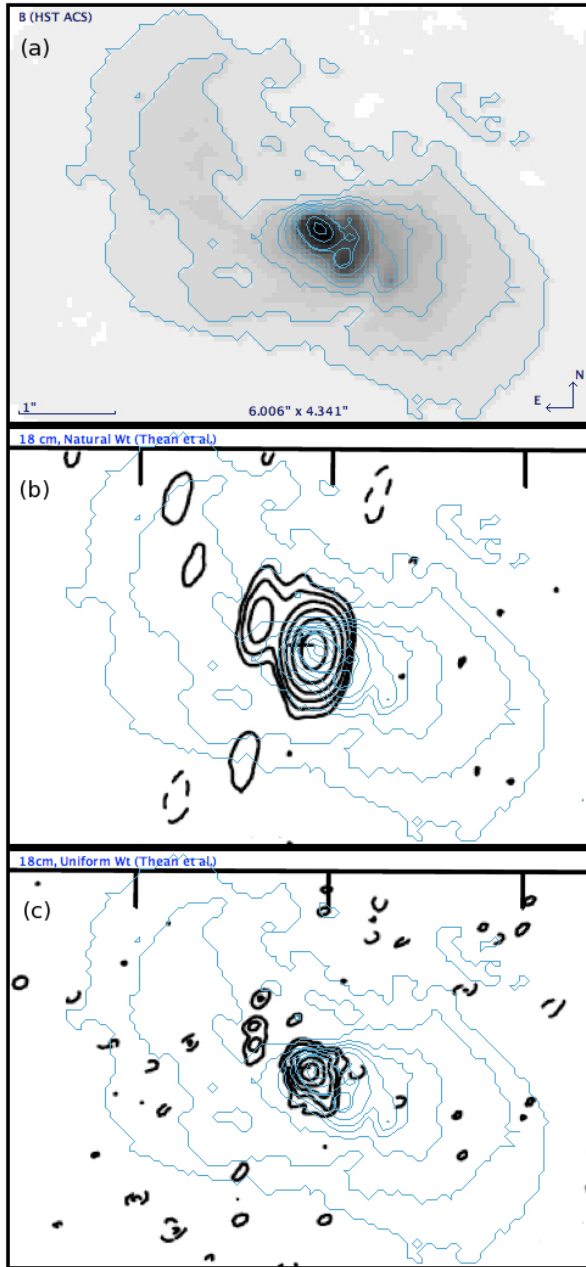


Figure 17. Comparison of new $0.44 \mu\text{m}$ (*HST* ACS) imagery with published 18 cm radio continuum (MERLIN) emission (Thean et al. 2001, Fig. 1) in the circumnuclear region of Mrk 266 NE. Top (a): *HST* ACS B-band image in grayscale; the same B-band data are contoured (blue) and overlaid here and in the following two panels. Center (b): 18 cm radio continuum interferometry with natural weighting and spatial resolution 0.5×0.3 HPBW (thick black contours) overlaid with ACS B-band (thin blue contours). Bottom (c): 18 cm radio continuum interferometry with uniform weighting and spatial resolution 0.2×0.1 HPBW (thick black contours) overlaid with ACS B-band (thin blue contours). The plus signs in panels (b) and (c) are from (Thean et al. 2001, see their Fig. 1) and they mark the optical nuclear positions, where the marker extent indicates the 2σ positional uncertainty. These positions are in good agreement with the astrometry we derived for the ACS images. The scale bar indicates $1''$, and the field of view is 6.0×4.3 for all three panels.

spectral index ($\alpha_{20,6,2\text{cm}} = 0.61 \pm 0.04$) of Mrk 266 NE are consistent with optically thin synchrotron emission (Mazzarella et al. 1988), and these parameters are similar to other luminous AGNs in the local universe (e.g., Rush

et al. 1996). The radio jet appears to be running into dense material concentrated 0.4 (240 pc) SW from the nucleus, but it is able to escape to a greater distance in the opposite direction (Fig. 17). This hypothesis is consistent with the velocity field measured for the molecular gas (§3.7) which shows a rotating disk aligned roughly orthogonal to this putative ionization cone. The B-I color map from the *HST* data (Figure 26) reveals that dust is distributed primarily along the NS direction, which again is roughly orthogonal to the AGN jet/outflow axis. Regions inside a radius of $\sim 2''$ from the nucleus of Mrk 266 NE (Fig. 26) are as blue as the Northern Loop, which is known to be dominated by bright [O III] $\lambda 5007$ and $\text{H}\alpha$ line emission (Hutchings et al. 1988; Ishigaki et al. 2000)²⁸. Davies et al. (2000) provided independent evidence for shock-heated gas in this region in the form of the radial profile of the 1-0 S(1) H_2 $2.12 \mu\text{m}$ emission line. Furthermore, the $\text{Br}\gamma$ emission-line image presented by Davies et al. (2000) shows a bimodal structure oriented at $\text{PA} \approx 50^\circ$ centered on the NE nucleus, providing additional support for our hypothesis. While most of this evidence is indirect, its combined weight favors our interpretation that the extranuclear emission around Mrk 266 NE is dominated by an AGN-powered outflow that is generating spatially extend shocks.

Similar events may be occurring in the SW galaxy. The *HST* images show numerous compact structures over a 1 kpc size region that share the same NS orientation as the prominent stellar bar seen in the H-band image. It is highly likely that these compact structures are young stellar clusters (see §3.6). Observations at 1.6 GHz (Thean et al. 2001) show sub-arcsecond structure aligned NW-SE with respect to the SW nucleus, similar to previous 5 GHz measurements (Mazzarella et al. 1988). Comparing the new *HST* images with the extended radio emission maps suggests the circumnuclear emission in this case is dominated by star formation. An AGN outflow in the SW galaxy may be present but is difficult to detect due to its relatively high inclination ($\approx 42^\circ$). It is very difficult to disentangle starburst-driven winds from AGN-driven winds in galaxies containing both a Seyfert 2 and a powerful starburst Veilleux et al. (e.g., 2005). Although evidence for an AGN-driven outflow in the circumnuclear region of Mrk 266 SW is weak, there is ample evidence for a starburst-driven superwind on a larger scale based on the filamentary $\text{H}\alpha$ and [O III] line emission that comprise the Northern Loop, and from the fainter emission-line filaments labeled “eastern arm-like region” and “west knot” in Figure 2 of Ishigaki et al. (2000), all of which appear to connect or align with the SW nucleus. Properties of the kpc-scale outflow revealed by the new data are discussed in §3.4.

3.2.5. Hard X-Ray Properties of the Nuclei

Basic properties of the *Chandra* data for Mrk 266 were presented by Brassington et al. (2007). We have per-

²⁸ The [O III] $\lambda 5007$ line emission around Mrk 266 NE (Hutchings et al. 1988) is elongated along the same position angle as the *HST* B-band image contoured here in Figure 17. This provides evidence that the *HST* B-band image is dominated by emission-line gas in this region. The passband of the F435W filter omits the [O III] lines, but it includes the [O II] $\lambda 3727$ line observed in the spectrum of Mrk 266 NE (Kim et al. 1995) and also at large radii within the ionization cones of many AGNs (e.g. Tadhunter 2008).

Table 6

Photometry of Knots Embedded in the Arc 0''4 west of the NE Nucleus

| R.A. hh:mm:ss.sss (1) | Dec dd:mm:ss.ss (2) | m _{F435W} mag (3) | m _{F814W} mag (4) |
|-----------------------------|---------------------------|----------------------------------|----------------------------------|
| 13:38:17.75 | 48:16:40.9 | 19.94 ± 0.03 | 19.02 ± 0.05 |
| 13:38:17.75 | 48:16:41.1 | 20.09 ± 0.03 | 18.89 ± 0.04 |
| 13:38:17.75 | 48:16:41.3 | 20.27 ± 0.03 | 19.06 ± 0.04 |

Note. — Columns (1) and (2): J2000 R.A. and Dec, with 1σ uncertainty in the absolute astrometry of 0''.5. Columns (3) and (4): Apparent magnitudes and uncertainties measured in the HST/ACS F435W (B) and F814 (I) bands, respectively.

formed additional processing to reveal previously unknown structural details and physical properties. As shown in Figure 18a, the SW (Seyfert 2) nucleus has a much softer X-ray spectrum and lower luminosity than the NE (LINER or composite AGN/Starburst) nucleus. The luminosity and hard X-ray spectrum of the NE nucleus provide a clear signature of an obscured AGN. The X-ray spectrum obtained of the integrated system with XMM (Fig. 6) shows strong Fe $K\alpha$ emission at 6.4 keV. This high-ionization feature has been observed in the ULIRGs Arp 220 (Iwasawa et al. 2005), in the LIRG NGC 3690 (Ballo et al. 2004), and more recently in the integrated (stacked) spectrum of 30 LIRGs in the GOALS sample that are relatively faint in the hard X-ray band (Iwasawa et al. 2009). Modeling the global XMM spectrum of Mrk 266 with a thermal (soft, extended) component due to star formation and an absorbed power-law (hard, compact) component from the AGNs results in an absorption column of $N_{\text{H}} = 6.5 \times 10^{22} \text{ cm}^{-2}$, which is close to the lower limits derived from the 9.6 μm silicate absorption feature (§3.2.1).

Unlike XMM, *Chandra* was able to resolve the nuclei and has detected two separate sources of (2-7 keV) X-ray emission, with the bulk of the combined emission emanating from the NE component (Fig. 3). The physical origin of the bright Fe $K\alpha$ line observed in the XMM spectrum of the integrated system is less clear. The *Chandra* spectrum of the total emission from Mrk 266 (Fig. 5f) does not show the Fe $K\alpha$ line. However, the large aperture (33'' radius) used to produce this spectrum introduces substantial noise in the background in the higher energy bands where there is very little extended emission. Detailed inspection of the *Chandra* data within small apertures centered on the nuclei provides a strong clue that the Fe $K\alpha$ line originates primarily from the SW nucleus²⁹, indicative of a reflection-dominated spectrum of a heavily obscured AGN. Since optical spectra reveal the presence of Seyfert 2 activity in the SW nucleus, the weakness of the hard X-ray emission can be understood as a consequence of suppression of X-rays by Compton thick absorption. Heavy obscuration towards the SW nucleus as inferred from the *Spitzer* IRS spec-

²⁹ The 6-7 keV (Fe K) image contains 10 counts from the NE nucleus and 4 counts from the SW nucleus, while the neighboring 3-6 keV band shows a much larger contrast, with 79 counts from the NE nucleus and only 1 count from the SW nucleus. In other words, the spectrum of the SW nucleus has almost no detected flux at energies > 4 keV, but it shows a sudden rise at the Fe K band (Fig. 5). This suggests that the hard band spectrum of the SW nucleus is dominated by flux from the Fe $K\alpha$ line.

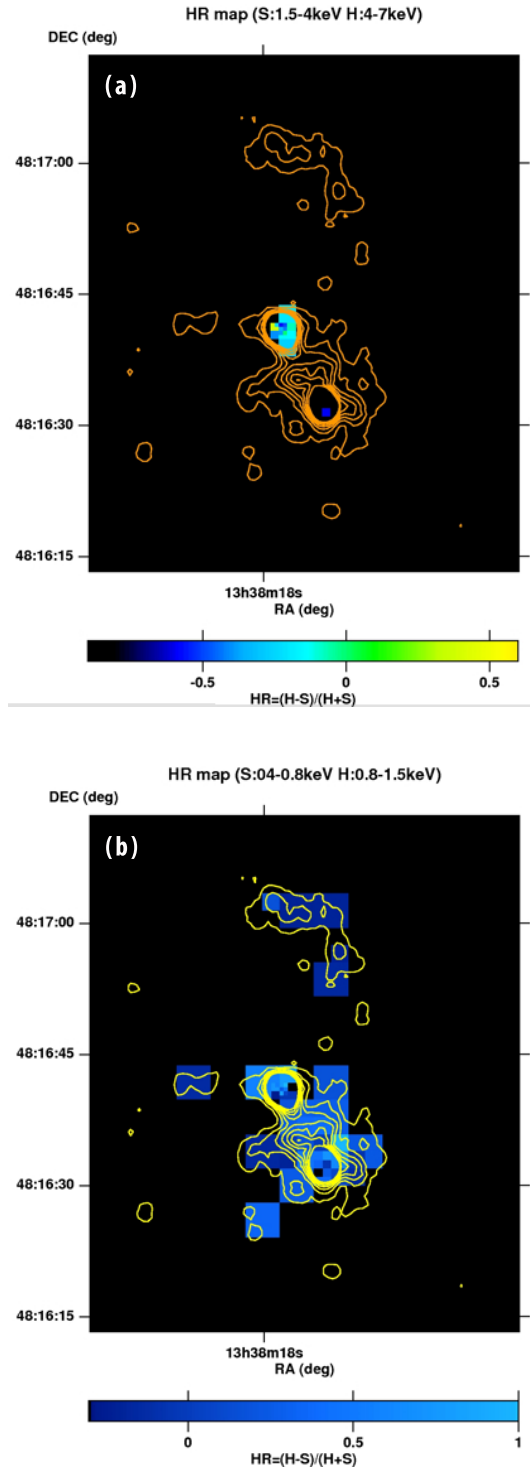


Figure 18. Maps of the hardness of the *Chandra* X-ray emission. (a): The hardness ratio between 1.5 and 7 keV, defined as $\text{HR}_{\text{hard}} = (F_{4-7\text{keV}} - F_{1.5-4\text{keV}})/(F_{4-7\text{keV}} + F_{1.5-4\text{keV}})$. The hard X-ray emission from the SW nucleus is too faint to measure this flux ratio, with the exception of the peak pixel which has $\text{HR}_{\text{hard}} = -0.4$ (blue). (b): The hardness ratio between 0.4 and 1.5 keV, defined as $\text{HR}_{\text{soft}} = (F_{0.8-1.5\text{keV}} - F_{0.4-0.8\text{keV}})/(F_{0.8-1.5\text{keV}} + F_{0.4-0.8\text{keV}})$; this illustrates the temperature variation over the diffuse emission. HR_{hard} and HR_{soft} are plotted using colors as indicated in their respective legends. The soft band X-ray data are overlaid as contours drawn with linear intervals between 1.4% and 12% of the peak brightness (in the NE nucleus) to emphasize the extended, diffuse emission.

trum and the large column density of obscuring material estimated from the CO (1-0) observations (§3.7) support this interpretation of the X-ray data.

If the 6-7 keV photons in the *Chandra* spectrum of the SW nucleus are due to Fe $K\alpha$ line emission, as our analysis suggests, the flux of $1.2^{+0.7}_{-0.5} \times 10^{-6}$ ph cm $^{-2}$ s $^{-1}$ accounts for the majority of the Fe $K\alpha$ line flux detected in the XMM-Newton spectrum. This means that the NE nucleus accounts for most of the escaping hard X-ray continuum, but it emits little Fe K emission. The equivalent width of Fe K expected from a source absorbed by $N_{\text{H}} \approx (6 - 8) \times 10^{22}$ cm $^{-2}$, as inferred for the NE nucleus (Table 2), is at most 0.1 keV (e.g. Awaki et al. 1991; Krolik et al. 1994; Ghisellini, Haardt & Matt 1994), while the equivalent width measured in the XMM-Newton spectrum is ~ 0.5 keV. This mismatch can be readily explained if the bulk of the Fe $K\alpha$ line emission is from the SW nucleus. The Fe $K\alpha$ line luminosity is 3×10^{40} erg s $^{-1}$. Using the relation derived in Iwasawa et al. (2005) for the Type 2 AGN in the HyLIRG IRAS F15307+3252, the intrinsic 2-10 keV luminosity of the obscured AGN in Mrk 266 SW is $\sim 1 \times 10^{42} f^{-1}$ erg s $^{-1}$, where f is the (unknown) visible fraction of the reflecting matter in the line of sight. The observed $F_{\text{X}}/F_{[\text{O III}]}$ ratio for the SW nucleus also indicates a highly absorbed X-ray source with $N_{\text{H}} \gtrsim 10^{24}$ cm $^{-2}$. (See Appendix §5.3.)

Finally, it should be emphasized that the Fe $K\alpha$ line detections are marginal. However, we gain confidence through independent 2σ detections for the global system with XMM and for the SW galaxy with *Chandra*, combined with line flux values that agree within the uncertainties in the calibrations and S/N (Table 2). A detection of Fe has also been reported at the 90% confidence level with ASCA GIS observations (Risaliti et al. 2000). Confirmation requires more sensitive observations.

3.2.6. The LINER in Mrk 266 NE

The relative strength of the PAH features, silicate absorption, and continuum shape indicate Mrk 266 NE is typical of an “IR LINER” or “Transition” between IR-luminous LINERs and “Type 1” LINERs. Although the mid-IR data for Mrk 266 NE are only sufficient to compute 3 of the 6 parameters in diagnostic diagrams (Fig. 2 of Sturm et al. (2006)), the relatively small $6.2\mu\text{m}/11.2\mu\text{m}$ PAH flux ratio (1.1) is on the low end of the distribution observed in “IR LINERs” (where the transition to Type 1 occurs), whereas the continuum flux ratios $f_{\nu}(15\mu\text{m})/f_{\nu}(6\mu\text{m}) = 16$ and $f_{\nu}(30\mu\text{m})/f_{\nu}(6\mu\text{m}) = 54$ place Mrk 266 NE on the extreme end of the distribution of “IR LINERs” with very red, warm dust continua. Mid-IR spectral data alone do not permit a clear distinction between the various kinds of energy sources that can power a LINER (e.g., Kewley et al. 2006; Ho 2008). However, there are at least four indicators that Mrk 266 NE is energized primarily by an AGN, in addition to shock excitation: (1) small PAH equivalent widths and a deficiency of 6.2 and 7.7 μm PAH emission relative to 11.3 μm PAH emission (§3.2.1); (2) morphological evidence for a radiative bow shock within an ionization cone aligned with radio plasma in an outflow (§3.2.4); (3) spectral properties of the luminous, hard X-ray point source (§3.2.5); and (4) a high $\text{H}_2(1-0)$ S(1) to Br γ flux ratio (Imanishi et al. 2009). Indeed, the strength and spatial extent of H_2 emission indicate the presence

of extensive shocks in the region (§3.2.2) that may be triggered by outflow from the AGN (§3.2.4).

3.3. Between the Colliding Galaxies

3.3.1. A Search for Counterparts to the Radio Emission

The bright radio continuum source located between the nuclei of Mrk 266 (Figs. 8a and 19) was interpreted as a source of enhanced synchrotron emission induced by shocking of the ISM at the interface of the merging galaxies (Mazzarella et al. 1988). Direct imaging of this area with *HST* ACS and NICMOS, *Spitzer* IRAC and MIPS (§2.6.1), and spectral mapping with *Spitzer* IRS (§2.7) reveals no obvious source at optical continuum, near-IR, or mid-IR wavelengths. This strongly rules out any third (dust-obscured) galaxy nucleus or a luminous off-nuclear star-forming region as observed in other interacting systems such as the Antennae (Mirabel et al. 1998) and II Zw 96 (Inami et al. 2010). Additionally, there is no detectable emission from this region in the near-UV or far-UV (Fig. 7 and 8h), and there is no detection of warm molecular gas in the continuum-free H_2 S(3) 9.67 μm emission-line image (Fig. 10). Although a bridge of CO (1-0) emission has been detected between the galaxies (Imanishi et al. 2009), it is shown below (§3.7) that this material is located to the north of the central radio continuum emission. Next we turn attention to the only other waveband where a source of radiation has been detected that is spatially correlated with the radio continuum emission between the galaxies.

3.3.2. X-Rays Between the Nuclei

Substantial soft X-ray emission has been detected between the nuclei of Mrk 266 by *Chandra*. Analysis by Brassington et al. (2007) indicates that the X-ray emitting gas in this region has an intrinsic luminosity of $9.8(\pm 0.5) \times 10^{40}$ erg s $^{-1}$ and has a temperature of 1.07 keV, approximately twice the temperature of much more diffuse emission surrounding the two galaxies (omitting the nuclei and northern source). Brassington et al. suggested that this X-ray emission is likely associated with the collision between the two galaxies, as proposed previously for the radio continuum emission (Mazzarella et al. 1988). The present work extends these results using re-processing of the *Chandra* data to enhance the definition of structure in the diffuse X-ray emission and to further characterize its physical properties.

To begin with, Figures 3 and 19 illustrate the remarkable correspondence between the 0.4-7.0 keV X-ray emission and the 20 cm radio continuum emission. As shown in Figures 8 and 19, the higher resolution 6 cm radio continuum emission ($0''.3 \times 0''.4$ FWHM), resolves the 20 cm source into a flattened structure with two sub-components. These components are coincident with the brightest knot of soft (0.4-4.0 keV) X-ray emission located between the galaxies. The contours of the full-band (0.4-7.0 keV) X-ray image in Figure 18 further delineates the structure of the diffuse emission between the nuclei and to the south-west. Figure 18b presents the hardness of the soft X-ray spectrum (HR_{soft}), which indicates temperature variations within the extended emission.

Figure 20 provides a detailed view of the enhanced soft X-ray emission between the two galaxies. The X-ray spectra in the three circled areas show that the SE region

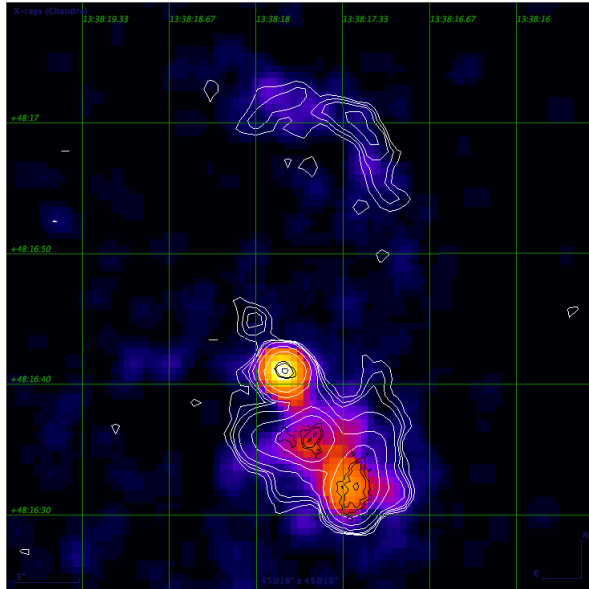


Figure 19. Mrk 266 *Chandra* 0.4 - 7 keV (full band) X-ray image in pseudocolor, VLA 20 cm radio continuum in white contours, and VLA 6 cm radio continuum in black contours. The X-ray data are based on image processing described in §2.3.1 of this study, and the radio data are from Mazzarella et al. (1988). The brightest 20 cm contours have been omitted so as not to obscure the 6 cm and X-ray emission. (See also Fig. 8.) The field of view is $45'' \times 45''$ and the coordinate grid is in J2000 equatorial coordinates.

has a softer spectrum indicating a lower temperature ($kT \approx 0.35$ keV) than the other two regions ($kT \approx 0.8$ keV). These differences are also reflected in the HR_{soft} map, where the SE region has $HR_{\text{soft}} = -0.16$ and the region at the radio continuum peak and $4''$ NE of that location have HR_{soft} ranging from 0.2 to 0.4. Therefore, the X-ray brightness certainly increases at the radio peak, but the temperature of the X-ray emitting gas at that location is similar to the region $4''$ (2.4 kpc) to the NW. A caveat in this analysis is that when dust obscuration is also varying spatially, HR_{soft} may not translate directly to real variations in temperature.

Table 7 presents physical parameters estimated from spectral analysis of the soft X-ray emission illustrated in Figure 20. The most straightforward interpretation is that the X-ray emission is the result of gas being shock-heated to $T \sim 10^7$. This physical process would also give rise to the observed enhanced synchrotron radiation (Mazzarella et al. 1988). Davies et al. (2000) interpreted the lack of H_2 1-0 S(1) emission from the central region of Mrk 266 as evidence for very fast shocks with relative velocities of ≈ 1000 km s^{-1} produced at the interface of superwinds emerging from the two galaxies. Such fast shocks would generate the observed non-thermal radio continuum emission and also heat the gas to $\gtrsim 10^6$ K, far above the dissociation temperature of H_2 . This would explain the lack of detected H_2 emission lines between the galaxies in the near-infrared observations of Davies et al. and in the mid-infrared IRS spectroscopy presented in the current study (§2.7). This physical scenario also predicts higher temperatures in the shocked region compared with the diffuse superwind. This is exactly what our refined analysis of the *Chandra* data reveals.

The estimated cooling time in this region is only 4 Myr. This is very short compared to the dynamical time scale

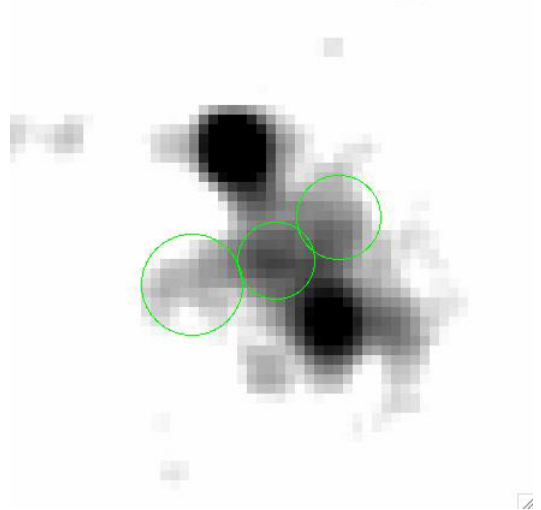


Figure 20. A close-up view of the *Chandra* soft-band (0.4 - 7 keV) X-ray emission in the region between the nuclei and to the SW. The three circled regions centered on the radio continuum peak (70 counts), $4''$ to the NW (70 counts), and $4''$ SE (39 counts), are used to analyze the hardness of the X-ray emission to deduce differences in the gas temperature.

Table 7
Spectral Analysis of X-rays Between the Nuclei

| Parameter (1) | Value (2) | Units (3) |
|-------------------------|------------------------|------------------------|
| 0.5-2 keV Flux | 2.7×10^{-14} | erg s^{-1} cm^{-2} |
| Temperature (kT) | $0.72^{+0.11}_{-0.09}$ | keV |
| Luminosity ^a | 1.4×10^{41} | erg s^{-1} |
| Volume | 8.1×10^{65} | cm^3 |
| Electron Density | 1.1×10^{-2} | cm^{-3} |
| Thermal Energy | 1.8×10^{55} | erg |
| Gas Mass | 1.2×10^7 | M_{\odot} |
| Cooling Time | 4×10^6 | yr |

Note. — Column (1): Physical parameter computed from analysis of the soft band (0.5-2.0 keV) *Chandra* emission in the region between the colliding disks of Mrk 266. Column (2): Value. Column (3): Units. The computations assume an angular-scale distance of 129 Mpc and the scale of 0.59 kpc/ $''$ (see §1.3), and the emitting region is approximated by a tube $4''$ in diameter and $13''$ in length at a position angle of -45° .

^a The bolometric luminosity of this thermal gas, as deduced via extrapolation from fitting the data at energies of 0.01-10 keV.

of the merger (a few hundred million years), and therefore it is likely that we are observing this emission during a short-lived phase of the interaction. This would explain why so few interacting systems have been found with radio continuum and X-ray emission enhanced between the galaxies to the same extent as in Mrk 266. However, as shown below, there is evidence that gas in this region may be replenished from the powerful starburst-driven superwinds (§3.4), or from gravitational infall of material toward the center of mass of the system (§3.7).

3.4. The Superwind and Northern Loop

An outstanding characteristic of Mrk 266 is the extensive filamentary nebula of ionized hydrogen ~ 30 kpc in diameter (Armus et al. 1990) contained within an X-ray nebula ~ 100 kpc in extent. Optical emission-line diag-

nostics and kinematics indicate this is one of the most energetic examples of an outflowing, starburst-driven superwind (Wang et al. 1997). Mrk 266 has the third highest $H\alpha$ luminosity in a sample of 40 local infrared-bright galaxies studied by Armus et al. (1990). Kollatschny & Kowatsch (1998) presented deep observations with *ROSAT* HRI that revealed luminous soft X-ray emission spatially correlated with a loop of $H\alpha$ and $[O\ III]\ \lambda 5007$ line emission $\sim 14''$ long by $7''$ wide extending ~ 10 - $34''$ (6-20 kpc) to the north of the system (herein called the Northern Loop), leading these authors to interpret the X-ray emission in this region as hot post-shock gas in a high-velocity “jet” (most likely emanating from the SW nucleus). Kollatschny & Kowatsch (1998) argued also that the X-ray emission is too luminous and the opening angle of the X-ray/ $[O\ III]$ emitting region is too small to be explained by a superwind. A third possibility, suggested by Brassington et al. (2007), is that the northern structure is a tidal tail containing in situ star formation that is responsible for the soft X-ray emission and $H\alpha$ emission. In the subsections below we exploit the new multiwavelength data to make the case that the Northern Loop is the most luminous component of a superwind energized by star formation and one (or both) AGNs.

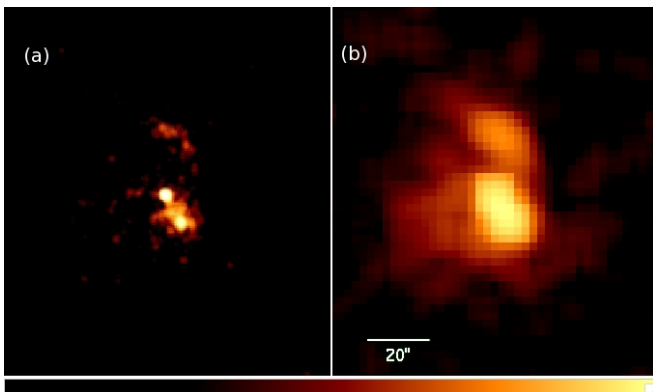


Figure 21. *Chandra* 0.4 - 7 keV (full band) X-ray data contrasting the high surface-brightness emission (highest resolution) with the large-scale diffuse emission. Left (a): Processed for maximum spatial resolution and smoothed with a 2-pixel Gaussian kernel (same as Fig. 3, bottom left). Right (b): The same data smoothed with a 6-pixel Gaussian kernel to highlight diffuse emission.

3.4.1. Spatially Correlated Soft X-rays and $H\alpha$ Filaments

Our reprocessing of the *Chandra* data (Fig. 21) reveals that the X-ray emission detected in the direct high-resolution data is a high-surface-brightness ridge embedded in a longer spur that extends an additional $\sim 20''$ (12 kpc) toward the NE. A map of the hardness of the soft X-ray spectrum (Fig. 18) shows the northern region has $HR_{\text{soft}} \approx -0.2$, indicating a relatively cool temperature of $kT \approx 0.3$ keV. If this is a region of in situ star formation, one would expect to find a high density of star clusters; however, the nearest detected optical star clusters are more than $5''$ (3 kpc) SW from the brightest X-ray and radio continuum emission in the Northern Loop (§3.6). Therefore, the properties of this feature must be ascribed to something other than starlight. Figure 22 shows that the diffuse soft X-ray emission (0.4 - 1.0 keV) corresponds remarkably well with observed $H\alpha$ filaments

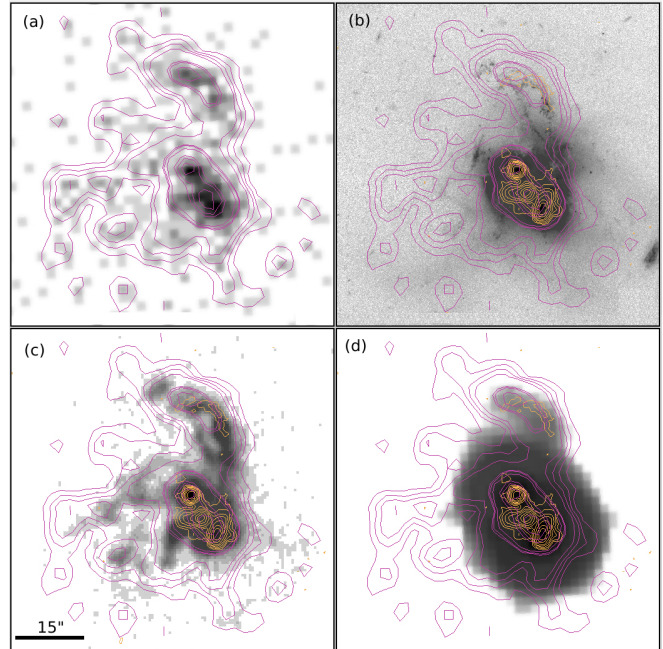


Figure 22. Soft X-rays compared to other wavelengths: (a): *Chandra* soft (0.4-1 keV) X-ray image re-binned with $2'' \times 2''$ pixels (grayscale). The contours are the same data smoothed with a 3-pixel Gaussian kernel to emphasize the faint, diffuse emission; the same contours are also overlaid in the other three panels. (b): *HST/ACS* B-band ($0.44\ \mu\text{m}$, F435W) image (grayscale) with the 0.4 - 1 keV X-ray data overlaid as magenta contours and the VLA 20 cm radio continuum image (Mazzarella et al. 1988) overlaid as orange contours. (c): $H\alpha$ image (Ishigaki et al. 2000) with the same contours as panel (b). (d): $24\ \mu\text{m}$ *Spitzer* MIPS image with the same contours as panels (b) and (c). Each field is $1/2 \times 1/2$ and the scale bar indicates $15''$.

and knots that extend out to ~ 18 kpc ($30''$) to the north and to the east of the galaxies. In the northern region, the soft X-rays have highest surface brightness near the outer edge of the Northern Loop detected in $H\alpha$ and in the B band (including $[O\ II]\ \lambda 3727$ line emission), which is also co-spatial with 20 cm radio continuum emission. Close spatial correlation between hot X-ray emitting gas and warm $H\alpha$ -emitting gas is a signature of winds in objects ranging from ULIRGs to dwarf starburst galaxies (Grimes et al. 2005).

3.4.2. Structure in the Northern Loop at ~ 100 pc Scales

The filamentary morphology of the Northern Loop revealed by the *HST* imagery is evidence for an expanding shell or “bubble” that is fragmenting due to Rayleigh-Taylor instabilities in a starburst- or AGN-driven superwind. Three dimensional hydrodynamic simulations of galactic winds predict this phenomena (Cooper et al. 2008). Elongated structures $\approx 0.5 - 1''$ (300-600 pc) in length protruding inward from the western, outer edge of the Northern Loop are highly suggestive of Rayleigh-Taylor fingers or bow shocks predicted by simulations (e.g., Heckman et al. 1990; Cooper et al. 2008). These protrusions appear to have a radial distribution centered on the NE nucleus (Fig. 23), indicating this AGN may be a primary energizing source for this component of the superwind. Wang et al. (1997) and Ishigaki et al. (2000) have shown that filaments throughout Mrk 266, including the Northern Loop, have line ratios (e.g., $[O\ III]\ \lambda 5007/H\beta$) indicating photoionization from

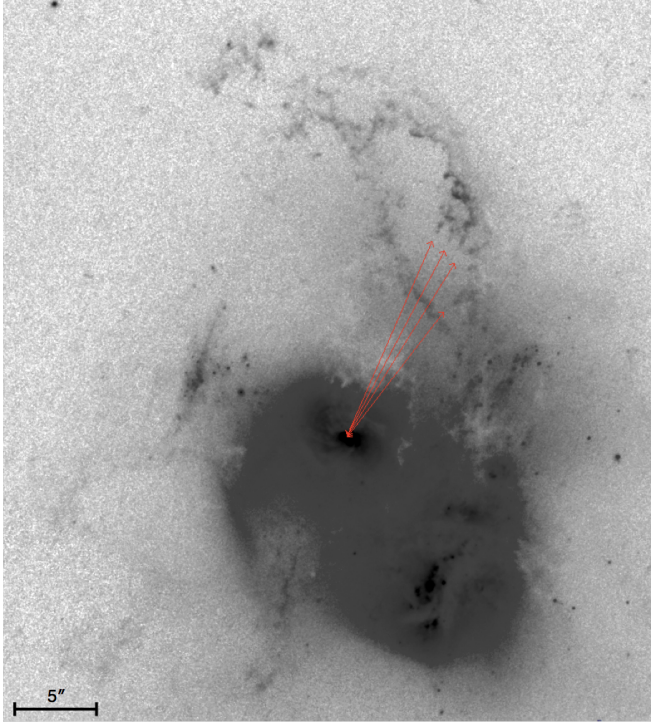


Figure 23. *HST/ACS* B-band ($0.44 \mu\text{m}$, F435W) image in grayscale with a field of view and intensity mapping chosen to emphasize the filamentary structure in the Northern Loop of Mrk 266. The arrows point out elongated structures $0.5\text{--}1''$ ($300\text{--}600$ pc) in length on the western side of the loop that appear to be aligned radially with the NE nucleus.

an AGN dominates over ionization from massive stars, and shocks that could explain the LINER-like nebular spectrum have insufficient energy to account for the luminosity of the extended nebula. However, the luminous starburst in the SW galaxy is also likely to be a major contributor to the overall energetics of the superwind.

The morphological, kinematic and ionization properties of the prominent Northern Loop can be interpreted with the superwind model of Heckman et al. (1990). In this scenario, the star-burst driven gaseous outflow has inflated a “bubble” that is highly elongated along the direction of least resistance (maximum pressure gradient), and the closed loop of optical line emission indicates the superwind in Mrk 266 is in a relatively young radiative cooling phase that occurs before the wind expands further during a “blow-out” phase. This again is consistent with the idea that we are observing a relatively short lived and dynamic phenomena.

3.4.3. Dust in the Wind

The detection of $24\mu\text{m}$ emission co-spatial with the Northern Loop (Fig. 22d) is strong evidence for thermal continuum emission from dust grains entrained in the superwind. By estimating the dust temperature and grain emissivity profile, the mass of dust can be derived following the single temperature thermal model of Hildebrand (1983), which is given by

$$M_{dust} = [(4/3) a \rho / Q_{\nu}] [S_{\nu} D^2 / B(T, \nu)], \quad (2)$$

where a is the average grain size ($0.1 \mu\text{m}$), ρ is the density of grain material, Q_{ν} is the grain emissivity characterized as $Q_{250\mu\text{m}}(250\mu\text{m}/\lambda)^{\beta}$, S_{ν} is the flux density of

the thermal emission at frequency ν , D is the distance, and $B(T, \nu)$ is the Planck function. Assuming $\beta = 1$ and other grain properties from Hildebrand (1983) results in $[(4/3) a \rho / Q_{24\mu\text{m}}] = 9.6 \times 10^{-3} \text{ g cm}^{-2}$ at $24 \mu\text{m}$. In more convenient units, the above equation becomes

$$M_{dust} = 0.016 S_{\nu}(24\mu\text{m}) D^2 [e^{(599.49/T_{dust})} - 1] M_{\odot}, \quad (3)$$

where $S_{\nu}(24\mu\text{m})$ is in Jy, D is in Mpc, T is in K, and M_{dust} is in M_{\odot} . The $24 \mu\text{m}$ flux density measured for the Northern Loop (17 mJy , or 2% of the total flux) corresponds to a dust mass $M_d(24\mu\text{m}) \approx 5 \times 10^7 M_{\odot}$. Using the calibration of Alton et al. (1999) based on the known case of M82, the total far-infrared luminosity ratio of $L_{\text{ir}}(\text{Mrk 266})/L_{\text{ir}}(\text{M82}) = 18$ predicts a dust mass of $\sim 2 \times 10^{7-8} M_{\odot}$ in the entire wind of Mrk 266. This would imply that the $24 \mu\text{m}$ emission from the Northern Loop contains at least 25% (and possibly the majority) of the total dust mass within the superwind of Mrk 266.

However, this result depends on the assumption that most of the observed flux is due to dust emission alone and that we have made a reasonable determination of T_{dust} . One possible source of alternate emission is the [O IV] $25.9 \mu\text{m}$ emission line. We estimate this contribution to be less than 10%³⁰. Since there is no detection in any other mid-IR or sub-mm passband available to help constrain T_{dust} , a characteristic temperature of 37 K is assumed based on modeling of sub-mm observations of the dusty outflow in M82 (Alton et al. 1999).

The overall physical interpretation presented above adds strong support for the superwind interpretation of Wang et al. (1997) in which stellar winds and supernovae are driving a powerful outflow of gas and dust. The Northern Loop is likely the cross section of the most luminous “bubble” of expanding ionized gas in the wind. The fragmented morphology and radial orientation of protrusions in this region suggest it is strongly influenced by radiation or a gaseous outflow energized by the NE galaxy, and the detection of co-spatial $24 \mu\text{m}$ emission provides strong evidence for dust mixed with the ionized gas in the superwind. The new observations are difficult to reconcile with a jet (ejection from an AGN) as suggested by Kollatschny & Kowatsch (1998) or with a (stellar) tidal tail as hypothesized by Brassington et al. (2007).

3.5. SED Analysis

3.5.1. Decomposition of Dust Emission Components

Figure 24 presents results of a multicomponent model decomposition of the IRS spectrum (Fig. 11) combined with the broad-band SED (Table 12, Fig. 9) of global measurements for the Mrk 266 system using the CAFE software package (Marshall et al. 2007)³¹. A very good fit to the SED is provided by a model consisting of PAH emission, atomic and molecular line emission, plus cold

³⁰ This estimate is based on the assumption that the mixture of ionized gas and thermal dust in the superwind of Mrk 266 may resemble a scaled up version of a planetary nebula such as NGC 2346 (Su et al. 2004). The published IRS spectrum of Mrk 266 shows a bright [O IV] $25.9 \mu\text{m}$ emission line, however it does not permit separation of emission from the SW nucleus and the diffuse emission in the Northern Loop.

³¹ CAFE could not be used to constrain the fits for the individual galaxies because the IRS spectral map could not resolve the galaxies over the $14\text{--}38\mu\text{m}$ range of the LL module (§2.7).

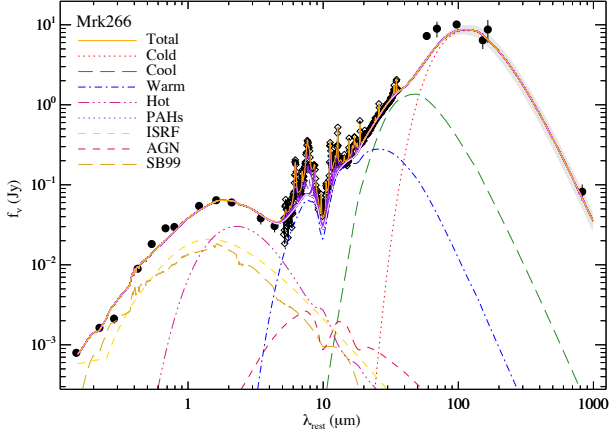


Figure 24. Results of multicomponent fitting using the CAFE software package (Marshall et al. 2007) to model the SED of the global emission from Mrk 266. Solid black circles are broadband continuum measurements, and open black squares are IRS spectral measurements. The solid orange curve represents the sum of the various fitted components identified in the legend. The corresponding fit parameters and uncertainties are given in Table 8.

(26 K), cool (72 K), warm (235 K) and hot (1500 K) thermal dust components heated by the combination of an unobscured photospheric interstellar radiation field (ISRF), an obscured starburst (SB) component with a strength constrained by the observed PAH emission, and an AGN (accretion disk) component with a strength constrained by the fitted hot dust emission. Uncertainties in the derived dust temperatures are ± 1 K.

Table 8 lists the results of the fit. The derived extinction-corrected PAH flux ratios appear to be fairly “normal,” located between the curves for ionized and neutral PAHs in Figure 16 of Draine & Li (2001). The parameter L_{source} is the sum of the derived intrinsic source luminosities $L_{\text{ISRF}} + L_{\text{SB}} + L_{\text{AGN}}$, and L_{dust} is the total dust luminosity. The primary results are the relative fractions of L_{source} , the fractions of L_{dust} , and the dust masses characterized as arising from cold, cool, warm and hot thermal dust components. As noted in Marshall et al. (2007), the four dust components used to model galaxies are typically heated to characteristic temperatures of $T_{\text{cold}} \approx 35\text{K}$, $T_{\text{cool}} \approx 80\text{K}$, $T_{\text{warm}} \approx 200\text{K}$, and $T_{\text{hot}} \approx 1400\text{K}$, where the actual temperatures (noted above and in Table 8 for Mrk 266) are determined from fitting of the radiation field energy density of the corresponding radiation sources. Although the model suggests that a hot dust component accounts for $\approx 10\%$ of the total dust luminosity, this is uncertain because the fitting of this component is weighted heavily by the mid-IR wavelength region where emission from hot dust competes with stellar photospheric emission. Reconciliation of this relatively low AGN contribution with spectral diagnostics that suggest a $\sim 50\%$ AGN contribution in the individual galaxies (§3.2.1) may be due primarily to an aperture effect. The latter measurements were made in apertures that isolate the nuclear regions, and they are thus more sensitive to AGN signatures than the larger apertures used to construct the SED for the global system which encompass more spatially extended starburst emission.

It is illustrative to compare Mrk 266 with the galaxies modeled by Marshall et al. (2007). Overall, the SED

Table 8
Results of SED Decomposition

| Parameter (1) | ISRF+SB+AGN (2) |
|--|-------------------------------|
| $\tau_{\text{warm}}(9.7\mu\text{m})^{\text{a}}$ | 2.7 ± 0.1 |
| PAH $6.2\mu\text{m}/\text{PAH } 7.7\mu\text{m}$ | 0.28 ± 0.03 |
| PAH $11.3\mu\text{m}/\text{PAH } 7.7\mu\text{m}$ | 0.28 ± 0.02 |
| $L_{\text{ISRF}}/L_{\text{source}}$ | 0.19 |
| $L_{\text{SB}}/L_{\text{source}}$ | 0.71 |
| $L_{\text{AGN}}/L_{\text{source}}$ | 0.10 |
| $L_{\text{source}} (L_{\odot})$ | $2.4(\pm 0.2) \times 10^{11}$ |
| $L_{\text{cold}} (26 \text{ K})/L_{\text{dust}}$ | 0.57 ± 0.09 |
| $L_{\text{cool}} (72 \text{ K})/L_{\text{dust}}$ | 0.20 ± 0.03 |
| $L_{\text{warm}} (235 \text{ K})/L_{\text{dust}}^{\text{b}}$ | 0.12 ± 0.01 |
| $L_{\text{hot}} (1500 \text{ K})/L_{\text{dust}}$ | 0.11 ± 0.01 |
| $L_{\text{dust}} (L_{\odot})$ | $2.2(\pm 0.2) \times 10^{11}$ |
| $M_{\text{cold}} (26 \text{ K}) (M_{\odot})$ | $1.5(\pm 0.4) \times 10^8$ |
| $M_{\text{cool}} (72 \text{ K}) (M_{\odot})$ | $1.5(\pm 0.6) \times 10^5$ |
| $M_{\text{warm}} (235 \text{ K}) (M_{\odot})$ | $7.0(\pm 0.2) \times 10^2$ |
| $M_{\text{hot}} (1500 \text{ K}) (M_{\odot})$ | 6.0×10^{-2} |

Note. — Parameters resulting from SED decomposition using the sum of ISRF + starburst + AGN radiation sources, as described in the text and plotted in Figure 24.

^a These values are likely closer to the intrinsic physical attenuation than the much lower value of $\tau_{\text{warm}}(9.7\mu\text{m}) = 0.7 \pm 0.1$ derived from spline fitting that estimates only the apparent strength of the silicate absorption feature §3.2.1.

^b The $L_{\text{warm}}/L_{\text{dust}}$ values are corrected for the attenuation by $1 - e^{-\tau_{\text{warm}}(9.7\mu\text{m})/\tau_{\text{warm}}(9.7\mu\text{m})}$.

of Mrk 266 can be modeled as a starburst dominated LIRG, with weak AGN indicators from the thermal dust or PAH emission, as is also the case in NGC 6240 and NGC 2623. While the cold dust component in Mrk 266 has essentially the same temperature as derived for NGC 6240 (29 K), the cool (72 K) and warm (235 K) dust components of Mrk 266 are significantly warmer than those in NGC 6240 (61 K and 193 K). Together the warm and hot components comprise 23% of the total dust luminosity of Mrk 266. For context, the sum of the (apparent) warm and hot dust fractions are 22% in NGC 6240, 77% in Mrk 463, and 82% in the QSO PG 0804 + 761. Within the uncertainties, Mrk 266 has the same cold dust mass as NGC 6240. Compared to the other two dual-AGN systems which have had SED decomposition using this technique, the T_{dust} distribution in Mrk 266 is quite similar to NGC 6240, and both of these systems have much smaller fractions of warm+hot dust than Mrk 463. The Mrk 266 SED fitting results also illustrate that only $700 M_{\odot}$ of dust at $T \gtrsim 200 \text{ K}$ can generate the same luminosity ($4.4 \times 10^{10} L_{\odot}$) as $1.5 \times 10^9 M_{\odot}$ of dust at $T \approx 72 \text{ K}$.

3.5.2. Flux Ratios

The physical nature of AGNs is often revealed via flux ratios. We begin by determining the “q” parameter as defined by Yun et al. (2001),

$$q_{\text{FIR}} = \log\left(\frac{\text{FIR}}{3.75 \times 10^{12} [\text{W m}^{-2}]}\right) - \log\left(\frac{S_{1.4\text{GHz}}}{[\text{W m}^{-2} \text{ Hz}^{-1}]}\right), \quad (4)$$

where $\text{FIR} [\text{W m}^{-2}] = 1.26 \times 10^{-14} (2.58 \cdot S_{60\mu\text{m}} [\text{Jy}] + S_{100\mu\text{m}} [\text{Jy}])$, and the flux densities are those measured by *IRAS* for the global system. In addition, the q_{FIR} parameter can be defined as

$$q_{24} = \log[(S_{24\mu\text{m}})/(S_{1.4\text{GHz}})], \quad (5)$$

where q_{24} is the 24 μm flux density measured by *Spitzer* MIPS. The data in APPENDIX Tables 12 and 13 give

$q_{\text{FIR}} = 2.0$ and $q_{24} = 0.95$ for the global system, and $q_{24} = 1.77$ (1.14) for Mrk 266 SW (NE). Mrk 266 is typical of galaxies in the *IRAS* 2 Jansky Survey, 98% of which fall in the range $1.64 \leq \langle q_{\text{FIR}} \rangle \leq 3.02$ (population mean $\langle q_{\text{FIR}} \rangle = 2.34$). A useful comparison for the q_{24} values is the sample mean $\langle q_{\text{FIR}} \rangle = 0.83 \pm 0.31$ (1σ dispersion) for over 770 galaxies in the *Spitzer* First Look Survey with redshifts less than 0.4 (Marleau et al. 2007). The global system and Mrk 266 NE are within 1σ of this sample mean, and although q_{24} for Mrk 266 SW is large compared to most LIRGs, it is within the 3σ dispersion of the FLS population. Therefore, Mrk 266 shows no significant deviations from the infrared-radio correlation followed by star-forming galaxies and radio-quiet AGNs.

The ratio of infrared to ultraviolet luminosities provides a diagnostic of the amount of reprocessed versus escaping radiation from young, massive stars. Mrk 266 has an observed ratio of $L_{\text{ir}}/L_{\text{UV}} = 20$, where L_{UV} is the sum of the NUV and FUV luminosities measured by *GALEX*, and it has a ratio $L_{\text{UV}}/(L_{\text{ir}} + L_{\text{UV}}) = 0.047$ (5%). With a correction for the finding that L_{ir} is powered roughly equally by the AGNs and star formation (§3.2.1), about 10% of the total star formation in Mrk 266 is observable directly as escaping UV photons, and 90% is UV radiation reprocessed into thermal infrared emission. Since the star formation rate (SFR) scales directly with the starburst component of $L_{\text{UV}} + L_{\text{ir}}$, the system has $\text{SFR}_{\text{UV}}/\text{SFR}_{\text{Total}} = 10\%$, which is on the high end of the distribution for the GOALS sample ranging 0.2% - 18% with mean 3% (Howell et al. 2010).

Lastly we examine the ratio of hard X-rays to infrared flux. Among 13 local ULIRGs studied by Armus et al. (2007), those with AGN-dominated mid-IR spectra have a ratio of hard X-rays to infrared luminosity $L_{\text{HX}}/L_{\text{ir}} \gtrsim 10^{-3}$, whereas starburst-dominated ULIRGs have $L_{\text{HX}}/L_{\text{ir}} < 10^{-4}$. The *XMM-Newton* measurement for the global Mrk 266 system gives $L_{\text{HX}}/L_{\text{ir}} = 3.5 \times 10^{-4}$, and the higher resolution *Chandra* measurements give $L_{\text{HX}}/L_{\text{ir}} = 5.0 \times 10^{-5}$ and $L_{\text{HX}}/L_{\text{ir}} = 1.0 \times 10^{-3}$ for the SW and NE nuclei, respectively. The component galaxies of Mrk 266 are therefore at extreme ends of the range observed to date in the local (U)LIRG population: The value of $L_{\text{HX}}/L_{\text{ir}}$ for Mrk 266 NE is 40% larger than NGC 6240, which itself is similar to ratios found in optical/UV-selected Seyfert galaxies and quasars (Ptak et al. 2003). Mrk 266 SW, on the other hand, has one of the smallest $L_{\text{HX}}/L_{\text{ir}}$ ratios among local (U)LIRGs, similar to Arp 220 and IRAS 22491-1808 (Armus et al. 2007). This is consistent with new evidence presented in §3.2.5 that the X-ray source in Mrk 266 SW is Compton-thick. The fact that the luminosity ratio of the SW and NE galaxies in hard X-rays ($L_{\text{HX}}(\text{SW})/L_{\text{HX}}(\text{NE}) = 0.16$) is close to the reciprocal of the ratio in the infrared ($L_{\text{ir}}(\text{SW})/L_{\text{ir}}(\text{NE}) = 3.3$) and in cold molecular gas ($L_{\text{CO}}(\text{SW})/L_{\text{CO}}(\text{NE}) = 4.9$; §3.7) is a strong clue that the factor of ≈ 20 disparity in the $L_{\text{HX}}/L_{\text{ir}}$ ratios for these galaxies is mainly due to differences in the column density of material absorbing UV/X-ray photons and re-emitting the energy in the far-infrared, rather than an order of magnitude difference in the intrinsic hard X-ray luminosities of the AGNs.

This same conclusion about high column density material as the responsible agent for the variance of flux ratios can be arrived at by simply comparing the two nuclei.

The data presented in §2.6.2 show that the luminosity ratio of the two galaxies, $L(\text{Mrk 266 SW})/L(\text{Mrk 266 NE})$, is ≈ 0.7 in the far-UV and soft X-ray bands, transitions through 1.0 in the near-infrared ($1.2 \mu\text{m}$), increases to a maximum of 5.7 at $8 \mu\text{m}$, and drops to 3.5 at $70 \mu\text{m}$ (the SED peak) and 3.3 in the total infrared emission (L_{ir}). The $L(\text{Mrk 266 SW})/L(\text{Mrk 266 NE})$ ratio drops further to 2.3 at $850 \mu\text{m}$, and to 1.4 at 20 cm. Thus, although Mrk 266 SW clearly dominates this merger in the mid-IR and far-IR, the two galaxies have similar luminosities in the near-IR, UV, soft X-rays, and radio continuum. It is only at the highest energies with available data for the separate galaxies where the situation is reversed: Mrk 266 NE is 6.4 times more luminous in the hard (2-7 keV) X-ray band than its companion Mrk 266 SW. As shown in §3.2.5, this is more likely due to a higher column density of absorbing material along our line of sight to the SW nucleus (compared to the NE nucleus) than to an intrinsic difference in their power sources.

3.6. Star Clusters

3.6.1. Cluster Detection and (B - I) Color Map

The *HST*/ACS images of Mrk 266 reveal numerous very compact, marginally resolved sources scattered throughout the system. Their overall properties indicate they are star clusters (SCs) and associations similar to those observed in other galaxies undergoing extensive bursts of star formation. The detection method followed the procedure described in detail by Modica et al. (2012) for SCs in the late stage LIRG merger IC 883. First, masks outlining the galaxy were applied to the images. Then *Source Extractor* (Bertin & Arnouts 1996) was used to fit and subtract the underlying galaxy and perform point source detection in the B and I band images. The extracted objects were processed with IDL routines to perform photometry and apply selection criteria that accepted only reliable sources with a FWHM of 1.7-4 pixels, have $\text{S/N} > 5$, and are detected in both bands; details are given in Modica et al. (2012). This procedure resulted in the detection of 120 point sources with $21 \text{ mag} \lesssim B \lesssim 27 \text{ mag}$ and $19.5 \text{ mag} \lesssim I \lesssim 25.7 \text{ mag}$ (uncorrected for extinction); their coordinates and photometric properties are listed in the Appendix (Table 15).

Figure 25 shows the direct *HST* B-band image (a) and the image after processing with *Source Extractor* to fit and subtract the local background and extract SCs (b). The density of SCs is highest in three extended regions identified with green ellipses in Figure 25b: (1) within and surrounding the disk of the SW galaxy; (2) along a band extending $\sim 5\text{-}15''$ (3-9 kpc) north-west from the NE galaxy, passing near the base of the Northern Loop; and (3) in a group centered $\sim 8''$ (5 kpc) north-east of the NE nucleus. There are 22 SCs within a projected radius of $5''$ (3 kpc) around the nucleus of Mrk 266 SW, and only 6 SCs within the same radius around Mrk 266 NE (black circles in Fig. 25b). The ratio of surface densities of detected clusters in the SW and NE galaxies (3.7) is nearly the same as the ratio of their infrared luminosities (3.5, see §3.5), and it is also similar to the ratio of their cold molecular gas masses (4.9, see §3.7). This situation is consistent with the apparent Hubble types and 1.6 μm bulge-to-disk ratios (§3.1.1) of the two galaxies (i.e., Sbb disk galaxies contain more gas to fuel star formation

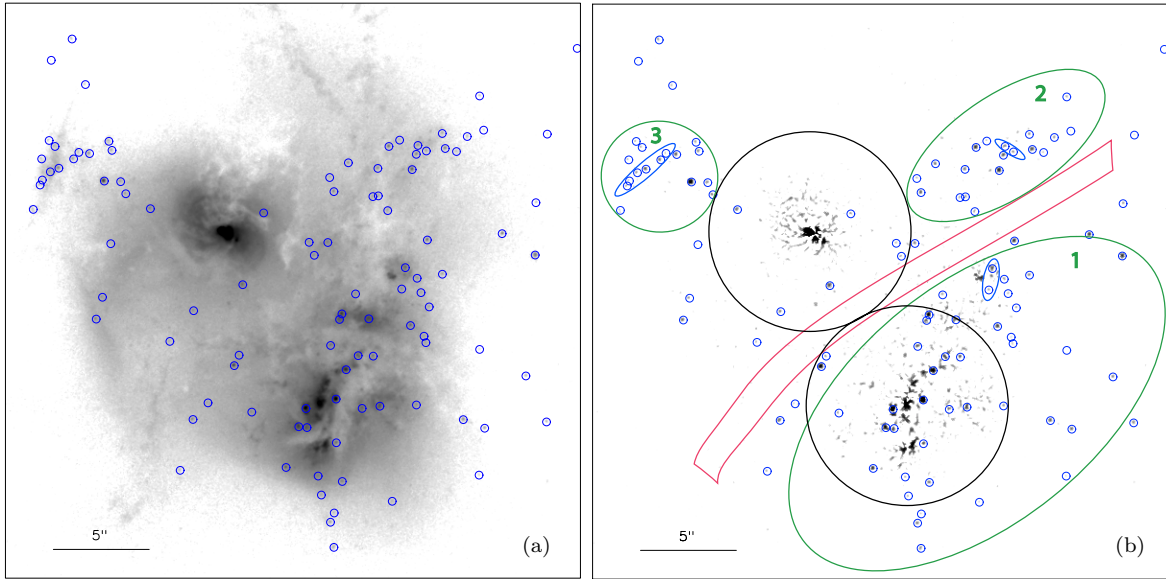


Figure 25. Star clusters (SCs) extracted by Source Extractor identified with small circles overlaid on the $0.44 \mu\text{m}$ (B, F435W) *HST* image before background subtraction (a) and after background subtraction using a median-masking technique (b). Panel (b) also identifies notable regions discussed in the text: three areas where most of the SCs are concentrated (large green ellipses), each of which contains a smaller concentration of very blue SCs (blue ellipses; see also Fig. 26); regions with radius $5''$ centered on the nuclei of the two galaxies (black circles); and a dearth of SCs bisecting the system at $\text{PA} \approx -47^\circ$ (red band).

than S0/a galaxies). Despite a nearly 4-to-1 ratio in the number of clusters detected in the central 3 kpc of the SW and NE galaxies, across the entire system there is a nearly equal number of clusters on both sides of a notable gap about $2''$ (1.2 kpc) wide running between the galaxies at $\text{PA} \approx -47^\circ$ (red band in Fig. 25b).

A color map revealing the variation of (B - I) magnitudes throughout Mrk 266 is shown in Figure 26, with an overlay of symbols coded to indicate the (B - I) colors of the SCs (uncorrected for extinction). Dust lanes present in the direct images (Figs. 1, 13 and 14) are more clearly delineated in this color map as filamentary regions with $(\text{B} - \text{I}) \gtrsim 2 \text{ mag}$. In the SW galaxy, the reddest dust lanes are on the east and west sides of the nucleus, and aligned with the major axis of the underlying starlight detected in the $1.6 \mu\text{m}$ image (Fig. 3); they are also aligned with the apparent rotation axis of the molecular gas (see §3.7). In the NE galaxy, the dust lane has an “S” shape that crosses the nucleus at $\text{PA} \approx -10^\circ$. Higher than average extinction explains the lack of detected clusters in these circumnuclear dust lanes. However, in the region between the galaxies the color map shows bluer (B - I) values, suggesting the apparent dearth of clusters along this gap (red band in Fig. 25b) may be intrinsic.

Some of the bluest SCs (blue circles in Fig. 26) are located in regions identified with blue ellipses in Figure 25b, including groupings centered $\sim 7''$ and $\sim 13''$ northwest of the SW nucleus (inside regions 1 and 2 noted above), and a notable chain $\approx 5''$ in length located northeast of the NE nucleus (inside region 3 noted above). The detected clusters are a direct probe of star formation occurring in regions with relatively low extinction. However, the fact that the total luminosity of the unobscured clusters ($M_B = -16.25 \text{ mag}$, or $L_B = 5 \times 10^8 L_\odot$) is only 0.1% (1.6%) of the total infrared (B-band) luminosity indicates that these clusters provide a minor contribution to the total energy output of the system.

The very blue colors of the Northern Loop and fila-

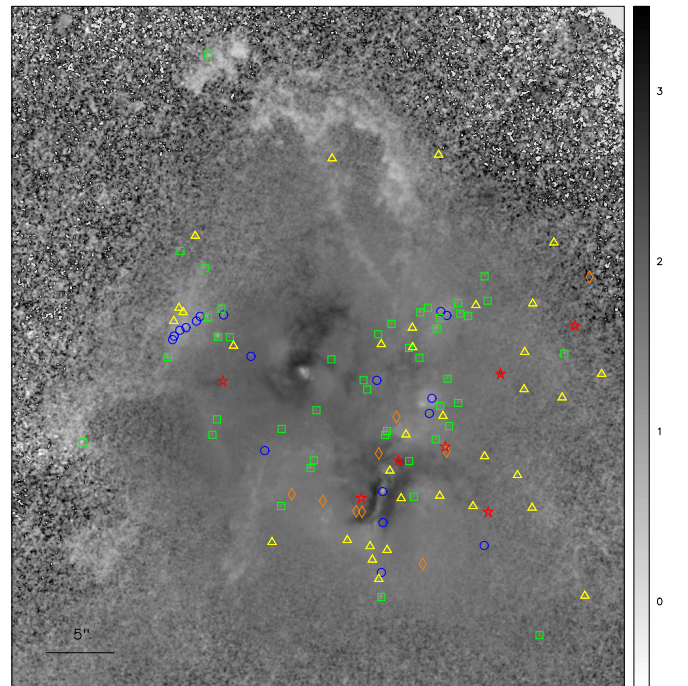


Figure 26. A grayscale F435W - F814W (B - I) color map of Mrk 266, with star cluster positions color-coded by their individual (B - I) colors in ranges as follows: $[\text{F435W}] - [\text{F814W}]$ (B - I) = 0 - 0.5 mag: blue circles; 0.5 - 1 mag: green squares; 1-1.5 mag: yellow triangles; 1.5-2.0 mag: orange diamonds; (B-I) > 2.0 mag: red stars. The scale bar on the right indicates the (B-I) colors of the pixels as observed, uncorrected for extinction (reddening).

ments throughout the system are likely a signature of strong nebular $[\text{O II}] \lambda 3727\text{\AA}$ and $[\text{O III}] \lambda 4364\text{\AA}$ line emission in the B band (see §3.4). The NE nucleus, the arc $0''.4$ to the west, and the bi-conic structure in which they are embedded are comparably blue, with $(\text{B} - \text{I}) \approx -0.2 \text{ mag}$. Similarity in color with filaments throughout the system that are visible in $[\text{O III}]$ emission-line imag-

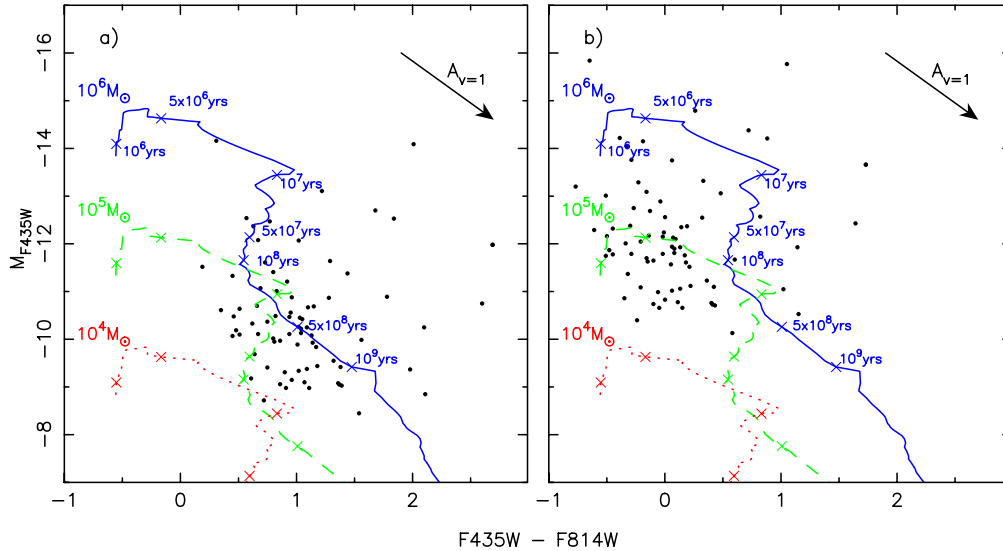


Figure 27. M_B vs. $B-I$ color-magnitude diagram for SCs detected in Mrk 266. Evolutionary tracks computed using population synthesis models (Bruzual & Charlot 2003) assuming an instantaneous starburst and Solar metallicity for cluster masses of 10^4 (red), 10^5 (green) and 10^6 (blue) M_\odot are shown. Marks on the $10^6 M_\odot$ track indicate the age of the starburst. The data are plotted with no extinction correction (a), and with a mean extinction correction of $A_V = 1.2$ mag estimated from various measurements as described in the text (b). The vector represents 1 mag extinction in the V band. Only SCs with uncertainties in $B-I$ less than 0.2 mag are shown.

ing (Ishigaki et al. 2000) lends support to the hypothesis presented in §3.2.4 that the circumnuclear region of Mrk 266 NE is an AGN ionization cone.

3.6.2. Star Cluster Color-Magnitude Diagram

Figure 27 is a $B-I$ vs. M_B color-magnitude diagram with evolutionary tracks constructed using population synthesis models from Bruzual & Charlot (2003). Most of the SCs have observed (apparent) colors of $0.5 \text{ mag} \leq (B-I) \leq 2.0 \text{ mag}$ and $-9 \text{ mag} \leq M_B \leq -13 \text{ mag}$ (Fig. 27a). Although there is an age/mass degeneracy in the uncorrected measurements, at first glance most of the SCs appear to have ages of a few hundred Myr to 1 Gyr. However, given the orientation of the extinction vector in Figure 27, which is nearly parallel to the age tracks in the population synthesis models, it is clear that the SCs are very likely to be significantly younger and/or more massive than they appear when uncorrected for extinction and reddening due to dust. There are other indicators for high but variable dust extinction: (a) dust lanes evident in the color ($B-I$) map (Fig. 26); (b) the observation that $\sim 90\%$ of the total luminosity is generated by dust emitting in the thermal infrared (§3.5); and (c) evidence for dust entrained in the superwind as far as $\sim 25''$ (15 kpc) from the center (§3.4.3).

Due to this high variability we can only apply a mean extinction estimate using the following indicators: (a) The emission-line Balmer decrement ($H\alpha/H\beta$) measured from long-slit optical spectroscopy resulted in $E(B-V)$ values of 0.72 mag and 0.22 mag for Mrk 266 SW and NE, respectively (Veilleux et al. 1995)³². (b) Long-slit spectroscopy along three position angles found $E(B-V) = 0.2 - 0.5$ throughout the inner $\sim 20''$ (10 kpc) of Mrk 266 (Wang et al. 1997). These measurements indicate a characteristic extinction of $E(B-V) = 0.4$ ($A_V = 1.2$ mag) in Mrk 266, which is similar to the sample mean of

$E(B-V) = 0.5(\pm 0.2)$ mag observed for a large sample of local, luminous starburst galaxies Calzetti et al. (1994). To estimate the total extinction at particular wavelengths, we assume $R_V = 3.1$ as found in the general ISM of our Galaxy. However, this can be considered a minimum, because regions containing young star clusters in Mrk 266 (and other LIRGs) could have a significantly larger value of $R_V \approx 6$ as measured in Galactic star-forming regions such as the Orion Nebula and giant molecular clouds (e.g., McCall 2004).

Application of a mean extinction correction of $A_V = 1.2$ mag to the observed colors (Fig. 27a)³³ shifts the points to an intrinsic mean color of $(B-I) \sim 0.0$ mag and to a mean luminosity of $M_B \sim -12$ mag (Fig. 27b). Comparison of the mean extinction-corrected data to the model curves (Fig. 27b) leads to the following results for the detected cluster population on average: (a) most of the SCs have ages between 1 and 50 Myr; (b) although the current data cannot remove the age/mass degeneracy for the reddest clusters ($B-I \gtrsim 0.5$ mag), about half of the objects are very blue ($B-I \lesssim 0.2$ mag), very young (1 - 5 Myr), and are consistent with masses of $\sim 10^5 M_\odot$; (c) the 11 most luminous SCs have $M_B \lesssim -13.5$ mag and are located near the (blue) track for $10^6 M_\odot$ clusters with ages of only $\sim 1-10$ Myr; (d) the two very luminous objects with $M_B \approx -15.8$ mag are located $0'75$ E (the red cluster with $B-I \approx 1.1$) and $0'91$ W (the blue cluster with $B-I \approx -0.6$) of the SW nucleus, respectively (see Fig. 26); and finally (e) if a mean extinction of $A_V = 1.8$ mag ($R_V \approx 6$) is more applicable than $A_V = 1.2$ mag in regions containing the blue SCs, as argued above, than most of the SCs are on average only ~ 1 Myr old and have masses spanning $\sim 10^5$ to $10^6 M_\odot$. These results indicate the detected SCs are massive and likely relatively young. However, they represent only the “tip of the iceberg” in terms of the extensive starburst which is mostly obscured

³² The identifications of the NE and SW nuclei of Mrk 266 were mistakenly swapped in the tables and figures of Kim et al. (1995) and Veilleux et al. (1995).

³³ The Galactic foreground extinction in the direction of Mrk 266 is only $E(B-V) = 0.013$ mag (Schlegel et al. 1998); with caveats documented in NED, this corresponds to $A_V = 0.04$ mag.

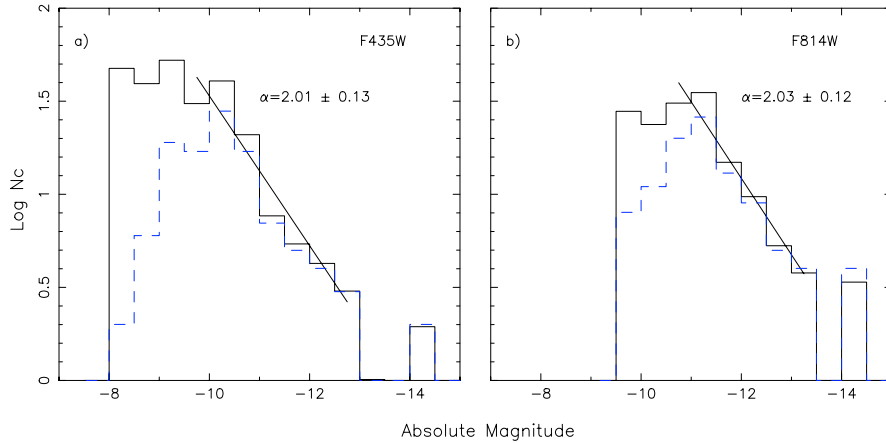


Figure 28. Luminosity functions of the extracted star clusters in the F435W (B) band and F814W (I) band before (blue) and after (black) correction for foreground contamination and completeness as described by Modica et al. (2012) and Vavilkin et al. (2012, in preparation). The solid line represents a linear fit (via χ^2 minimization) to the corrected (black) histogram bins over the ranges $-9.75 \leq M_B \leq -12.75$ and $-10.75 \leq M_I \leq -13.25$. Alpha indicates the slope of the SC luminosity function in each bandpass over these ranges of M_B and M_I , which have *not* been corrected for the estimated mean extinction (see text).

by dust in optical and UV observations.

3.6.3. Star Cluster Luminosity Functions

Figure 28 is a plot of the luminosity function (LF) derived for the SCs detected in the B and I band images. The index (α) of a power law fit to the LF, after correction of the cluster counts for foreground contamination and completeness using techniques described in Modica et al. (2012) and Vavilkin et al. (2012, in preparation), is $\alpha = -2.0 \pm 0.1$ in both the B and I bands.

It is revealing to compare the power-law slope of the star cluster luminosity function (LF) in Mrk 266 with the star cluster LFs observed in other merger systems. In the well-studied Antennae Galaxy, the cluster LF has $\alpha_V = -2.13 \pm 0.07$ (Whitmore et al. 2010). In the early-stage merging LIRG system II Zw 96, $\alpha_B = -1.1 \pm 0.3$ was found (Inami et al. 2010). For clusters in two well-known ULIRGs that appear to be in intermediate and late stages of the merger process, the following slopes were measured by Surace et al. (1998): $\alpha_B = -1.6 \pm 0.1$ for Mrk 463, and $\alpha_B = -1.8 \pm 0.2$ for Mrk 231. For SCs in the late-stage (single nucleus) merger system IC 883, Modica et al. (2012) derived LF indices ($\alpha_B = -2.2 \pm 0.2$ and $\alpha_I = -2.0 \pm 0.2$) that are remarkably similar to the values found in Mrk 266. In another late-stage LIRG merger remnant, NGC 34 (Mrk 938), the star cluster LF has $\alpha_V = -1.75 \pm 0.1$ (Schweizer & Seitzer 2007). (Both IC 883 and NGC 34 are in the GOALS sample, with $L_{\text{ir}} = 5.4 \times 10^{11}$ and $2.5 \times 10^{11} L_{\odot}$, respectively.) It is also noteworthy that the LF slopes in Mrk 266 and these other (U)LIRGs are similar to the LFs of young star clusters in the irregular galaxies SMC and LMC, which have mean $\alpha = -2.0 \pm 0.2$ (Gieles et al. 2006). The specific frequency of young star clusters is defined as $T_N = N_{\text{cl}} \times 10^{(0.4(M_B + 15))}$, where N_{cl} is the number of clusters above the specified luminosity limit normalized by the B-band luminosity of the host galaxy (e.g., Larsen & Richtler 1999). Correcting for completeness in the cluster detection, Mrk 266 has $T_N = 0.91$, which is similar to completeness-corrected T_N values observed in the cluster-rich LIRG sample of Vavilkin et al. (2012, in preparation). We conclude that α and T_N for star clusters in Mrk 266 are similar to other LIRGs.

Various disruption mechanisms have been described in the literature to model the luminosity, mass and age distributions of star clusters in interacting galaxies (e.g., Whitmore et al. 2007). Given that Mrk 266 has one of the most powerful superwinds known in the local universe (§3.4), this raises the question of whether star clusters are being disrupted by this outflow/feedback process to a larger degree than in systems such as the Antennae with much less powerful superwinds and lower star formation rates. The dearth of detected SCs in the interaction zone of Mrk 266 noted above, despite relatively low extinction and molecular gas spanning part of this region (§3.7), and despite the presence of SCs in other regions at equally large distances from the galaxy centers, may be a sign of cluster disruption or suppression of star formation in this narrow band between the two galaxies. A possible explanation would be fast shocks and extensive turbulence at the interface of the colliding galaxies or colliding superwinds expanding from the two galaxies, as discussed in §3.3. However, there is no signature of cluster disruption on a global scale in Mrk 266, as might be revealed through an α or T_N value that is significantly different than the SC populations observed in (U)LIRGs with less powerful superwinds.

3.7. Molecular Gas Properties

3.7.1. The Integrated Emission from CO, NCH, and HCO⁺

Interferometric observations of Mrk 266 in HCN(1-0), HCO⁺(1-0) and CO(1-0) with the *Nobeyama Millimeter Array* were presented by Imanishi et al. (2009). In this section these data are used to explore the distribution of molecular gas with respect to various features in the system, and to derive the physical conditions of the cold molecular gas. Figure 29 presents contours of the integrated emission from these three molecular transitions overlaid on images ranging from X-rays through radio continuum. There are intriguing differences between the spatial distributions of these molecular species. Although the SW galaxy contains about 5 times more flux in CO (1-0) than its companion, the NE galaxy is clearly detected in all three molecular transitions. The bulk of the integrated CO (1-0) emission in the system is aligned with the major axis of the SW galaxy, with a centroid

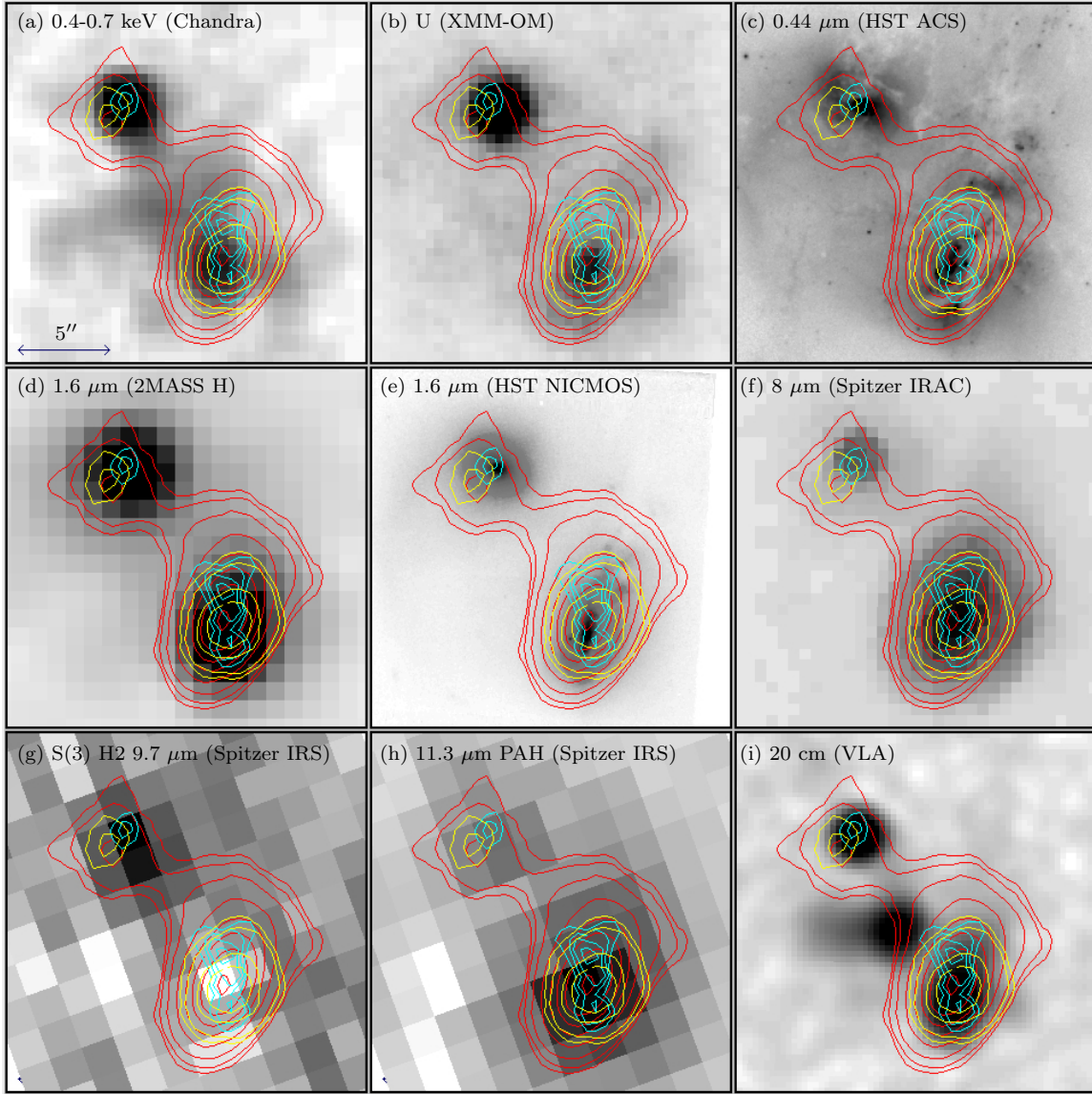


Figure 29. The integrated emission of Mrk 266 in CO(1-0) (red contours), HCN(1-0) (cyan contours), and HCO⁺(1-0) (yellow contours) with a spatial resolution of 4''3 x 3''4 (PA = -31.5°) from the *Nobeyama Millimeter Array* (Imanishi et al. 2009) are shown superposed on grayscale representations of the following images: (a) *Chandra* 0.4-7 keV X-ray image, (b) *XMM-OM* U band, (c) *HST ACS* 0.44 μm, (d) 1.6 μm (2MASS H), (e) 1.6 μm (HST NICMOS), (f) 8.0 μm (IRAC), (g) H₂ S(3) 9.7 μm (IRS), (h) 11.3 μm PAH (IRS), and (i) 20 cm (VLA). The 2MASS 1.6 μm (H) image is included to show the accuracy of the spatial registration of the 1.6 μm NICMOS image. All panels display a field of 20''x 20''. The scale bar is 5''.

near the X-ray/infrared nucleus. CO (1-0) is also detected in a bridge connecting the two galaxies, which is discussed further below (§3.7.2). The HCN gas in the SW galaxy shows double structure with peaks located ≈ 1.2 kpc (2'') to the NE and SW of the region where the CO (1-0) and HCO⁺(1-0) are most heavily concentrated at the location of the X-ray/IR/radio nucleus. If this morphology is due to limb-brightening in a rotating disk, the HCN disk is tilted $\sim 10^\circ$ with respect to the axis of the CO (1-0) and 1.6 μm emission (Fig. 29e). Most of the CO emission in the NE galaxy is offset by ~ 1 kpc (1'5) to the SE of the X-ray/optical nucleus. The CO (1-0) in this region is spatially coincident with the peak of the HCO⁺(1-0), whereas the dense gas traced by HCN is concentrated very close to the nucleus about 1 kpc to the NW. Figure 29c shows that the centroid of the HCN emission is aligned within 0'2 of the eastern point source

in the *HST* B-band image, which we interpret to be the AGN of Mrk 266 NE (§3.2.4).

Applying the formulation of Evans et al. (2005) to compute L'_{CO} , and assuming a CO luminosity to H₂ gas mass conversion factor $\alpha = 1 M_\odot (\text{K km s}^{-1} \text{pc}^2)^{-1}$ suggested by observations of ULIRGs (Downes & Solomon 1998), results in estimates of the warm molecular gas mass for the two galaxies: 3.4×10^9 and $7.0 \times 10^8 M_\odot$ for Mrk 266 SW and NE, respectively. The sum of these components corresponds to a total mass of $M(\text{H}_2) = 4.1 \times 10^9 M_\odot$. However, the maps also include an extended component, and the integrated CO(1-0) line flux of the total system is 180 Jy km s^{-1} (Imanishi et al. 2009). The corresponding total molecular hydrogen gas mass of Mrk 266 from the *Nobeyama* observations is thus $M(\text{H}_2) = 7.0 \times 10^9 M_\odot$. Within the uncertainties, this is consistent with

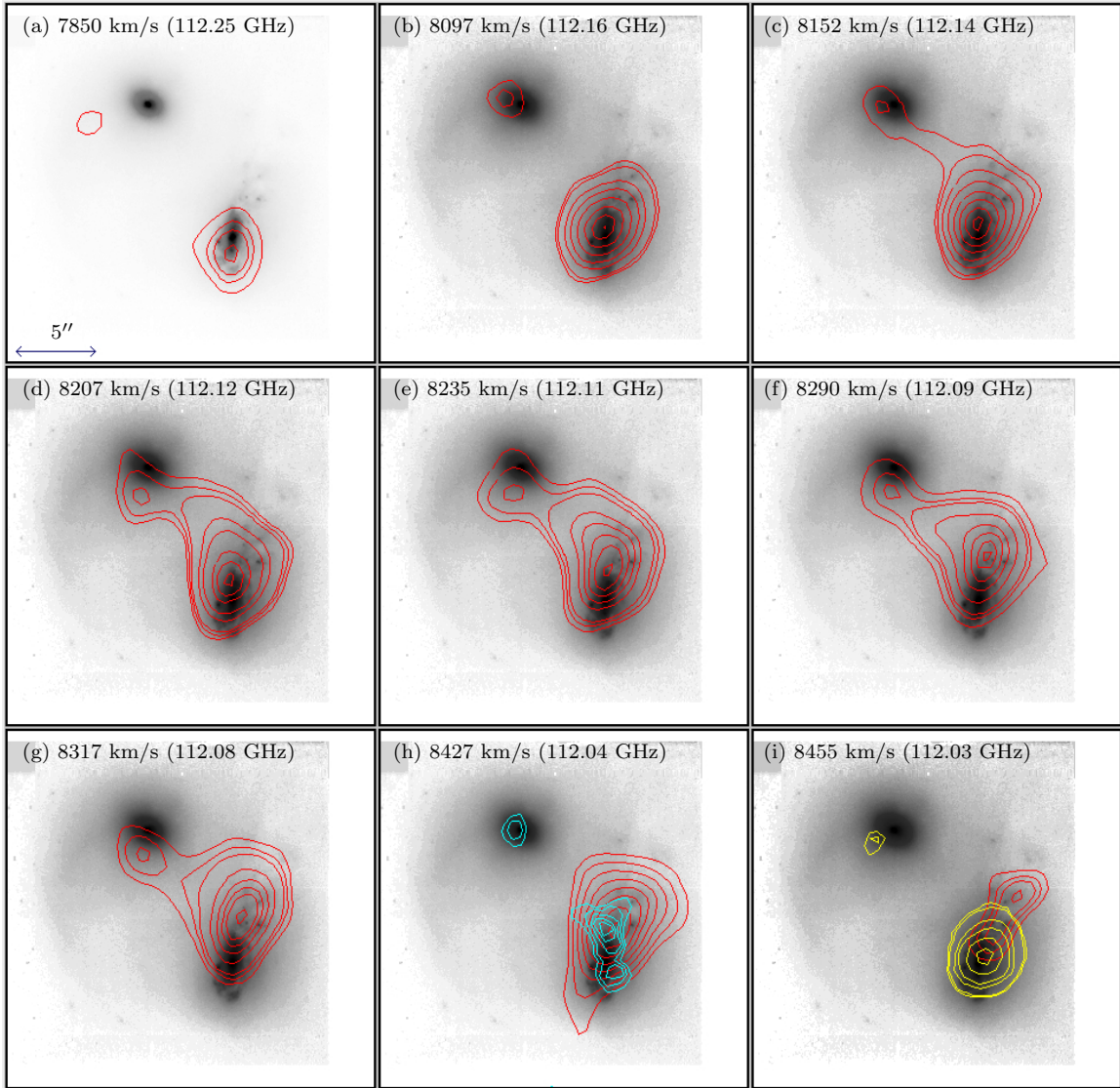


Figure 30. The spatial distribution of the CO (1-0) emission as a function of radial velocity (frequency) using a channel map from the *Nobeyama Millimeter Array* (Imanishi et al. 2009). The CO data are contoured in red and superposed on a grayscale representation of the *HST* 1.6 μm image to illustrate the kinematics of the CO with respect to the old stars in the galaxies. For comparison, the integrated emission from HCN (1-0) is plotted (cyan contours) in panel (h), and the integrated emission from HCO⁺(1-0) is shown (yellow contours) in panel (i). The mean radial velocity (and frequency) is shown in each panel. All panels display a $24'' \times 24''$ field, and the scale bar is $5''$.

206 Jy km s^{-1} measured with single-dish observations (Sanders et al. 1986) and a corresponding estimate of $M(\text{H}_2) = 2.5 \times 10^9 M_\odot$ when adjusted to $\alpha = 1$. If the CO to H_2 conversion factor appropriate for Mrk 266 is similar to GMCs in our Milky Way ($\alpha = 4 \pm 1$, Radford et al. 1991), the actual gas masses may be ~ 4 times larger than the estimates computed here. (Sanders et al. (1986) derived $M(\text{H}_2) = 1.4 \times 10^{10} M_\odot$ assuming $\alpha = 4$.) Assuming a weighted mean dust temperature of 50 K in the CO-emitting regions based on SED fitting (§3.5.1) and using the observed CO (1-0) line widths, applying the formulation of Evans et al. (2005) enables estimation of the radius of the unresolved CO-emitting regions, the dynamical masses of the galaxies, as well as the column densities. These results are presented in Table 9.

3.7.2. Spatial Distribution and Kinematics of CO (1-0)

Figure 30 shows the spatial distribution of CO (1-0) in velocity channels ranging from 7850 to 8455 km s^{-1} , in

Table 9
Molecular Gas Properties of Mrk 266

| Parameter (1) | SW (2) | NE (3) | Total (4) |
|---|----------------------|----------------------|-------------------|
| CO (1-0) flux [Jy km s^{-1}] ^a | 88 | 18 | 180 |
| CO (1-0) FWHM [km s^{-1}] ^a | 500 | 250 | ... |
| L'_{CO} [$\text{K km s}^{-1} \text{pc}^2$] | 3.4×10^9 | 7.0×10^8 | 7.0×10^9 |
| $M(\text{H}_2)$ [M_\odot] | 3.4×10^9 | 7.0×10^8 | 7.0×10^9 |
| $R(\text{CO})$ [pc] | 208 | 134 | ... |
| $M_{\text{Dynamical}}$ [M_\odot] | 1.2×10^{10} | 1.9×10^9 | ... |
| $M(\text{H}_2)/M_{\text{Dynamical}}$ | 0.28 | 0.37 | ... |
| Column Density [cm^{-2}] | 1.6×10^{24} | 7.9×10^{23} | ... |

Note. — Column (1): Observed or derived parameter. Columns (2)-(4): For the SW galaxy, NE galaxy, and the total system, respectively—the value of the parameter in Column (1).

^a The CO (1-0) line fluxes and line widths are from Imanishi et al. (2009); all other parameters are derived here for the first time.

judiciously chosen steps varying from 30 to 250 km s⁻¹, produced from the FITS channel map provided by Imanishi et al. (2009). The CO (1-0) contours are superposed on the *HST* NICMOS 1.6 μ m image for comparison with the highest resolution tracer available for the (old) stellar mass in the galaxies, and to minimize confusion from dust obscuration and young star-forming regions that dominate the imagery at shorter wavelengths.

The CO (1-0) emission in Mrk 266 SW shows a strong velocity gradient ranging from 7850 km s⁻¹ on the SE side to 8235 km s⁻¹ on the NW side of the disk. At progressively higher velocities, the centroid of the CO (1-0) emission is located at larger radii, extending as far as $\approx 5''$ (3 kpc) NW from the SW nucleus. The molecular gas in this off-nuclear region has a radial velocity ≈ 450 km s⁻¹ greater than the SW nucleus, and this gas coincides spatially with the most luminous region of off-nuclear star formation that is prominent in optical and UV images (see Fig. 8). Although the density of SCs is not significantly higher than in the surrounding areas, this region contains many of the most luminous SCs (Fig. 25).

The low $L_{\text{CO}}/L_{\text{IR}}$ ratio in Mrk 266 NE is consistent with its apparent near-IR Hubble type of S0/a (pec), suggesting that its pre-merger gas content was relatively low and incapable of sustaining a high SFR. Figure 30 shows that a large quantity of molecular gas detected over the velocity range 8150 – 8320 km s⁻¹ is bridging between the galaxies. The highest concentration of CO on the NE side of the bridge is centered ≈ 1 kpc ($1''.5$) to the SE of the nucleus of Mrk 266 NE. As shown in Figure 29i, the CO (1-0) in this off-nuclear region coincides with the peak of the HCO⁺ (1-0) emission, whereas the HCN (1-0) emission is concentrated at the NE nucleus. This result is consistent with research that has called into question the use of HCN as a tracer of dense gas fueling star formation, suggesting that in some cases HCN is energized by an X-ray Dissociation Region (XDR) associated with an AGN (e.g., Graciá-Carpio et al. 2008).

The distribution of CO (1-0) in Mrk 266 suggests the system is currently in a short-lived phase in which $\sim 40\%$ of the cold molecular gas is falling toward the center of mass of the system, or transferring between the galaxies along a tidal bridge as predicted by merger simulations (e.g., Cox et al. 2006). Mrk 266 appears to be in a similar evolutionary stage as three other LIRGs in the GOALS sample that have a large fraction of their total CO emission located between the nuclei: VV 114 (Yun et al. 1994), NGC 6090 (Bryant & Scoville 1999), and NGC 6240 (Engel et al. 2010). However, unlike VV 114 where the 1.4 GHz radio continuum emission has a similar spatial distribution as the CO, the enhanced radio continuum emission between the nuclei of Mrk 266 peaks $\approx 2''$ (1.2 kpc) south of the CO bridge (Fig. 29i). Another difference is that whereas the bulk of the HCO⁺ in VV 114 is located between the nuclei (Imanishi et al. 2007), in Mrk 266 the HCO⁺ is still bound to the galaxies.

3.8. Wider Implications

The proceeding sections have shown that Mrk 266 exhibits the simultaneous occurrence of a variety of phenomena including dual AGNs, an outflow containing a likely radiative bow shock in the narrow-line region of the NE nucleus, a starburst with a population of young star

clusters, a galactic scale “blow-out” expelling dust in a superwind, shocked gas between the galaxies, and molecular gas falling toward the center of mass or transferring between the galaxies. In this closing section, Mrk 266 is compared with other local major mergers and (U)LIRGs, and we attempt to place the system into a tentative sequence with a small number of other confirmed dual AGNs (with kpc scale nuclear separations) that may represent stages in the formation of binary AGNs (accreting SMBHs with pc-scale orbital separations).

3.8.1. Emission Between Interacting Galaxies

Interacting systems exhibiting substantial radio continuum, X-ray, or molecular gas emission between the galaxies are rare, but a few have been studied in detail. By comparing these systems with Mrk 266 we may be able to gain further insight into this phenomenon.

The Taffy Galaxy (VV 254): This interacting pair has $\approx 50\%$ of its total 1.5 GHz flux emerging between the companions, which has been interpreted as synchrotron radiation from cosmic ray electrons trapped in magnetic field lines and stretched like taffy as the galaxies pass through each other (Condon et al. 1993). Imaging in 450 and 850 μ m continuum emission and in multiple transitions of CO indicate the bridge between the galaxies consists of interstellar dust and gas extruded from the galaxy disks via direct cloud-cloud collisions (Zhu et al. 2007). Mid-infrared observations have detected substantial PAH emission in the bridge (Jarrett et al. 1999).

The regions between the components of Taffy and Mrk 266 both contain large fractions of their total radio continuum and CO emission, yet they contain little or no evidence for luminous star formation. However, unlike Taffy, there is no detected infrared enhancement between the galaxies of Mrk 266. In addition, while the radio continuum and CO emission are roughly spatially aligned and uniformly distributed between the Taffy galaxies, in Mrk 266 the central radio emission is much more centrally concentrated and the bridge of CO (1-0) emission is spatially decoupled from the radio continuum and X-ray emission. The absence of a discrete mid-IR or far-IR source between the galaxies of Mrk 266 suggests shocks may have destroyed most of the dust grains in this region. The collision in the Taffy system was estimated to occur $\sim 2 \times 10^7$ yr prior to its current configuration (Condon et al. 1993). Its global star formation rate is not significantly higher than in non-interacting spiral galaxies (Zhu et al. 2007), and no evidence for an AGN has been published for either galaxy.

The Antennae (NGC 4038/4039): This galaxy pair is well known for having $\sim 30\%$ of its total bolometric luminosity, $\sim 40\%$ of its total CO (1-0) flux (Zhu et al. 2003), and a high concentration of young star clusters (Whitmore et al. 1999) located in an off-nuclear region between the colliding disks. We have shown that in Mrk 266 the molecular gas bridging the galaxies is decoupled from the central radio/X-ray source, and there is no evidence for star formation between the galaxies. Compared to Mrk 266, the Antennae exhibit: (a) ~ 5 times lower luminosity in the far-infrared and in CO (1-0); (b) a cooler effective dust temperature; (c) a large region of diffuse X-rays, but a weaker superwind; (d) a pair of long tidal tails rather than diffuse, asymmetric tidal debris; and (e) low-luminosity LINER and starburst (H II) nuclei.

Early simulations suggested we are viewing the Antennae galaxies soon after their first encounter (e.g., Dubinski et al. 1996), but a recent model that accounts for the starburst in the overlap region constrains the system to ~ 40 Myr after the second encounter and only ~ 50 Myr before the galaxy centers fully merge (Karl et al. 2010). The close projected separation and small relative velocity of the nuclei imply Mrk 266 is in a similar stage of the merger process as the Antennae. The lack of well defined tidal tails in Mrk 266 may be due to any number of conditions, including a relatively small disk mass in the NE galaxy (§3.1.1); a retrograde encounter or an orbital geometry (e.g., a smaller perigalactic distance) that produces more diffuse tidal debris (Dubinski et al. 1996); or a large ratio of dark matter halo mass to visible (bulge plus disk) mass that can cause tails produced early in the encounter to fall back onto the galaxies quickly, resulting in late-stage tidal debris resembling loops and shells (Mihos et al. 1998). It is noteworthy that the extent of the diffuse optical emission in Mrk 266 (≈ 103 kpc) is similar to the end-to-end length of the tails in the Antennae. A detailed simulation of kinematic data for Mrk 266 is needed to constrain its true dynamical age.

NGC 6240: Mrk 266 appears to be in a similar evolutionary stage as the well-known system NGC 6240, in which X-ray observations by *Chandra* have also revealed dual AGNs (Komossa et al. 2003) and a large fraction of the molecular gas is located between the nuclei (Tacconi et al. 1999). Although the total infrared luminosity is about half that of NGC 6240, Mrk 266 has a much warmer dust temperature ($f_{60\mu\text{m}}/f_{100\mu\text{m}} = 0.72$) compared with NGC 6240 ($f_{60\mu\text{m}}/f_{100\mu\text{m}} = 0.26$). Likewise, decomposition of the infrared SEDs indicates warm (cool) dust components of 225 K (73 K) in Mrk 266 compared to 193 K (61 K) in NGC 6240 (§3.5.1). The 0.4-10 keV X-ray luminosity of Mrk 266, 9.5×10^{41} ergs s^{-1} , is 57% that of NGC 6240, and within the uncertainties of the X-ray flux absorption corrections their intrinsic L_x/L_{ir} ratios are similar ($5 - 7 \times 10^{-4}$). The projected separation of the nuclei in NGC 6240 is ≈ 1 kpc ($1''8$).

Stephan's Quintet: This is a well studied compact group containing a large intergalactic shock region with substantial radio continuum, X-rays, infrared and molecular gas emission. Unlike Mrk 266, the main shock region of Stephan's Quintet exhibits broad (870 km s^{-1}) rotational lines of warm H_2 with an order of magnitude higher surface brightness than the soft X-ray emission (Appleton et al. 2006). This dichotomy may be explained by a difference in the shock conditions in the two systems. Detailed modeling suggests the shock velocity in Stephan's Quintet is $\leq 300 \text{ km s}^{-1}$ (Cluver et al. 2010). As noted by Davies et al. (2000), if the intergalactic shock front in Mrk 266 is produced by the collision of superwinds expanding outward from the two galaxies at $\sim 300 \text{ km s}^{-1}$, adding this $\Delta V \sim 600 \text{ km s}^{-1}$ to the collisional velocity of the two galaxies can produce a net shock velocity approaching $\sim 1000 \text{ km s}^{-1}$. This would heat the gas far above the dissociation temperature of H_2 (Lim 2003), which is consistent with a temperature of $\sim 10^7$ K deduced from modeling of the soft X-ray data (§3.3.2). Another difference between these systems is that although $\sim 40\%$ of the CO (1-0) in Mrk 266 is located in a bridge between the galaxies where little or no star formation is

taking place, in Stephan's Quintet CO (1-0) is detected in regions where star formation is occurring as traced by $24 \mu\text{m}$ dust emission and UV continuum emission from young, massive stars (Cluver et al. 2010).

In summary, the radio continuum and X-ray emission between the galaxies in Mrk 266 is more similar to the large-scale shock detected in Stephan's Quintet than the off-nuclear star formation observed in the Antennae. The lack of bright H_2 line emission and infrared emission from dust grains in the central region of Mrk 266 may be due to the presence of a very fast shock that effectively destroys most of the dust grains, sublimates the molecular gas, and inhibits star formation. The ridge of $\sim 10^7$ K gas between the galaxies of Mrk 266, which is nearly ~ 10 times hotter than in other regions of the diffuse X-ray nebula and has a correspondingly short cooling time, is consistent with this scenario. Since the region with enhanced soft X-rays and radio continuum emission between the galaxies is not well aligned with the molecular gas bridge (Fig. 29) and the physical processes generating these features are likely quite different (shocks generated via superwinds and gas transfer via gravitational tidal forces), we suspect that these two short-lived phases are not directly linked. However, their simultaneous appearance is not a mere coincidence, as both phenomena are causally related to the ongoing galaxy merger.

3.8.2. Will Mrk 266 become a ULIRG?

It is well established that most local LIRGs and effectively all ULIRGs involve interacting and merging gas-rich spiral galaxies (e.g., Sanders & Mirabel 1996), and the ULIRG phenomenon occurs predominantly in late-stage mergers when dust is heated to high temperatures by being transported by gravitational torques (with the rest of the ISM) close to the central power sources (e.g., Mazzarella et al. 1991b; Mihos & Bothun 1998). Clearly ULIRGs must pass through a LIRG phase as the star formation rate and/or AGN fueling rate increases the dust heating to produce a luminosity of $L_{\text{ir}} \gtrsim 10^{12} L_{\odot}$. At least two lines of evidence – one based upon merger simulations and one based on molecular gas properties – suggest that Mrk 266 will transform into a ULIRG.

Numerical simulations show the timescale for major mergers (from initial approach through final coalescence of the nuclei) averages ~ 2 Gyr, but spans 1 – 8 Gyr, depending on the circularity of the orbit, the virial radius and circular velocity (e.g., Jiang et al. 2008). Comparison of the observed properties of Mrk 266 with hydrodynamical simulations (Barnes & Hernquist 1996; Mihos & Hernquist 1996; Hopkins et al. 2006; Cox et al. 2006) suggests we are viewing this system about 50% to 70% of the way through the merger process. The presence of an asymmetric halo of low surface-brightness optical emission spanning over 100 kpc, a relatively small projected nuclear separation of 6 kpc, and a low relative velocity of the nuclei of $\Delta V = 135 \text{ km s}^{-1}$ (Khachikian et al. 2006) indicate the two galaxies are likely undergoing their second or third encounter, with each passage damping the relative velocities of the nuclei, strong dynamical friction causing the orbit to decay, and tidal torques driving strong inflows of gas. As pointed out by Mihos (1999), the timescale for violent relaxation is $\gtrsim 1$ Gyr in the outer regions (low V_c), but only ~ 100 Myr in the inner regions (high V_c). Thus, depending on whether

the nuclei are on the verge of free-fall (which can occur as rapidly as $\approx \frac{1}{4}$ of a rotation period) or whether they will orbit one more time before fully merging, the estimated time to coalescence is about 50 to 250 Myr. (We are referring here to the merger of the stellar systems, not the SMBHs. The latter is discussed in §3.8.3.) Based on Monte Carlo simulations of merger models to match the observed distribution of nuclear separations in ULIRGs (Murphy et al. 1996), Mihos (1999) concluded that most ULIRGs are in the final 20% of the merger process. Thus, Mrk 266 appears to be in an interesting evolutionary stage when the nuclei are about to enter the final phase of coalescence characteristic of ULIRGs.

The total cold molecular gas mass of Mrk 266 is similar to that of ULIRGs observed locally and at high redshifts (e.g., Solomon & Vanden Bout 2005). Given that $\approx 40\%$ of the total CO (1-0) emission is in a bridge between the galaxies, there is a large reservoir of cold molecular gas available to form more stars or to fuel the AGNs as the galaxies and nuclei fully coalesce. With $L'_{\text{CO}} = 6.7 \times 10^9 L_{\odot}$ and $L_{\text{ir}}/L'_{\text{CO}} = 50.4$, Mrk 266 falls directly on the well known correlation between $\log(L_{\text{ir}}/L'_{\text{CO}})$ and $\log(L_{\text{ir}})$ (Solomon & Vanden Bout 2005). Within the evolutionary scenario of Sanders et al. (1988a,b), we expect Mrk 266 will evolve into a ULIRG initially with a relatively “cool” global far-infrared dust temperature similar to Arp 220, followed by a “warm” ULIRG phase exemplified by Mrk 463 (Mazzarella et al. 1991a; Bianchi et al. 2008). Given the new evidence for dust entrainment in the extensive superwind of Mrk 266 (§3.4.3), this system illustrates that the “blow-out phase” when large quantities of dust are expelled to reveal previously obscured optical/UV AGNs can begin during an intermediate stage of the merger before the nuclear coalescence phase when ULIRGs are most likely to occur.

ULIRGs have a much lower space density than LIRGs locally and at intermediate redshifts (Le Floch et al. 2005). In addition, the mean luminosity of ULIRGs in the local universe is lower than ULIRGs and submillimeter galaxies at high redshifts (e.g., Solomon & Vanden Bout 2005). The resolution of these observations may well lie in the pre-merger gas content of the participant galaxies. The higher that gas content, the larger the burst of star formation and subsequent dust heating. In the case of Mrk 266, the NE component contains ≈ 5 times less molecular gas than its companion; this is consistent with its apparent morphological type (S0/a) and correspondingly high bulge-to-disk ratio found at 1.6 μm . Using the well-established correlation of L_{CO} with L_{ir} (Young et al. 1986), a merging pair involving two late-type spirals with molecular gas masses similar to Mrk 266 SW (SBb) would have L_{CO} a few times higher than is observed in the actual Mrk 266 (SBb + S0/a) pair, resulting in a total L_{ir} at the high end of the local ULIRG distribution (Solomon & Vanden Bout 2005).

In the hierarchical model, a galaxy’s Hubble type is a byproduct of its merger history (e.g., Schweizer 2000). In this scenario, although merging played an important role in galaxy evolution over all cosmic time, high- z galaxies and proto-galaxies were very different than those observed at intermediate and low redshifts, and prior to $z \sim 1$ the Hubble sequence was not yet in place. However, from $z \sim 1$ to the present, because many late-type spiral

galaxies merged and transformed into early-type spirals, S0, or elliptical galaxies, the fraction of late-type spirals has decreased substantially (e.g., Oesch et al. 2010). Locally at $z \sim 0$, this makes pairings of gas-rich, late-type galaxies less likely than pairings of one late-type with one early-type galaxy (or of two early-type galaxies). Therefore, at low redshifts a smaller fraction of major mergers will have sufficient gas to fuel star formation or AGN accretion at the level required to reach the ULIRG threshold during early to intermediate phases of the merger. As argued above, however, this would not prevent a ULIRG from developing later if one of the companions has $\gtrsim 7 \times 10^9 M_{\odot}$ of molecular gas available to be driven toward the center of mass of the system to fuel two massive AGNs as they inspiral toward final coalescence. Mrk 266 is apparently in this physical situation.

3.8.3. Evolution from Dual to Binary AGNs

In this final section we turn attention to the significance of Mrk 266 in context with other confirmed dual AGN systems in an attempt to understand the low detection rate of binary AGNs with sub-parsec scale orbits found in recent surveys. We also propose a putative evolutionary sequence involving a quantitative parameter available for a small number of major merger systems with confirmed dual AGNs and candidate binary AGNs.

Current theory predicts the following evolutionary sequence (e.g., Colpi & Dotti 2009, and references therein): (a) pairs of massive galaxies separated by many times the diameter of their luminous disks and bulges will merge in ~ 1 Gyr (a few dynamical time-scales) due to dynamical friction between their massive dark matter halos; (b) the two pre-existing SMBHs in their cores (with $M_{\text{SMBH}}/M_{\text{bulge}} \approx 0.1\%$) will form *dual AGNs* as tidal torques drive the ISM inward to fuel accretion at a higher rate than existed prior to the encounter; during this stage the nuclei are merging from a separation of $\gtrsim 1$ kpc to ~ 10 pc; (c) in many cases conditions may be conducive to forcing the black holes pairs to *inspiral* over a period of ~ 100 Myr to a separation of $\lesssim 10$ pc, at which point they enter Keplerian orbits and may be detectable as *binary AGNs*; (e) the SMBHs will eventually either completely coalesce or else recoil, resulting in the most powerful sources of gravitational waves predicted to exist. Considering the relatively small number of dual AGNs confirmed to date, it is tempting to conclude that it is rare for both SMBHs to have accretion rates high enough to power two luminous AGNs simultaneously. However, given that the column density of gas and dust in (U)LIRGs is high enough to make the central ~ 100 pc optically thick in the mid-infrared, and even in the far-infrared in many cases (e.g., Thompson et al. 2005), many more dual AGNs will likely be detected with observations in other spectral regions. Indeed, X-ray surveys suggest $\approx 60\%$ of optically classified LINERs are true AGNs (Gonzalez-Martin et al. 2006), and high resolution radio continuum imaging finds a high fraction (74%) of AGNs among optically classified LINERs in the 1 Jy ULIRG sample (Nagar et al. 2003).

Along with Mrk 266 and NGC 6240, the following local (U)LIRGs have also been confirmed to contain dual AGNs based on detection of two compact, luminous sources of hard X-rays: Mrk 171 (Arp 299 = NGC 3690 + IC 694) (Ballo et al. 2004) and Mrk 463 (Bianchi et

al. 2008). Mrk 171 is similar to NGC 6240 in terms of infrared luminosity ($L_{\text{ir}} = 8.5 \times 10^{11} L_{\odot}$), and projected nuclear separation (0.9 kpc, $3''.8$). However, with $L_{\text{x}}(2 - 10 \text{ keV}) = 2.7 \times 10^{41} \text{ ergs s}^{-1}$ (uncorrected for absorption), Mrk 171 has $L_{\text{x}}/L_{\text{ir}} = 8.4 \times 10^{-5}$, which is an order of magnitude smaller than Mrk 266 and NGC 6240. With $L_{\text{x}}(2 - 10 \text{ keV}) = 3.8 \times 10^{42} \text{ ergs s}^{-1}$, Mrk 463 has a hard X-ray luminosity 9 times greater than Mrk 266 and 16 times greater than Mrk 171. Mrk 463 has $L_{\text{x}}/L_{\text{ir}} = 1.9 \times 10^{-3}$, which is ~ 2 -5 times larger than NGC 6240 and Mrk 266, and ~ 23 times larger than Mrk 171. A remarkable dual AGN is 3C 75, in which both nuclei are emitting powerful double-sided radio jets (Owen et al. 1985); this system consists of a pair of elliptical galaxies with projected separation 6.4 kpc ($14''$).

There is growing evidence that the current small number of confirmed dual AGNs will increase, primarily with observations of hard X-rays. For example, in a local sample of hard X-ray selected AGNs, 10% have been found to reside in dual systems with separations < 100 kpc (Koss et al. 2012).³⁴ Dual AGNs and binary AGN candidates are also being found in surveys probing to higher redshifts. The $z = 0.36$ system COSMOS J100043.15+020637.2 has been confirmed to contain two luminous AGNs with a separation of 2.5 kpc ($0''.5$) (Comerford et al. 2009). In CXOC J100043.1+020637, Civano et al. (2010) have interpreted the presence of optical morphology indicating a major merger, a large velocity offset, and an X-ray iron line with an inverted P-Cygni profile as a recoiling SMBH or a slingshot effect in a triple system. The published SED indicates $L_{\text{x}}/L_{\text{ir}} \approx 0.018$, which is orders of magnitude larger than in the local (U)LIRGs. Four more dual AGNs with kpc-scale separations and $0.13 < z < 0.21$ have also been discovered recently in the SDSS (Liu et al. 2010).

What appears to be the first bona fide *binary* AGN was discovered in 4C +37.11, which contains two compact radio sources with a projected separation of only 7.5 mas (7 pc). Based on the radio source compactness, variability, motion in the jets, and spectral shapes, Rodriguez et al. (2006) concluded that both radio cores contain AGNs orbiting with a rotational period of 1.5×10^5 yr within a single elliptical galaxy host. It is notable that the sum of the SMBH masses in 4C +37.11, $\sim 1.5 \times 10^8 M_{\odot}$, is similar to Mrk 266; this implies that LIRGs with bulge masses similar to the companions in Mrk 266 may end up as remnants similar to 4C +37.11. The soft X-ray luminosity of 4C +37.11 is ≈ 170 times larger than Mrk 266. (Hard X-ray observations of 4C +37.11 are not available.)

Very few additional binary AGNs have been confirmed, although there are a few candidates. Observations of double-peaked emission lines in the radio-quiet QSO SDSS J153636.22+044127.0 ($z = 0.388$) have been interpreted as a candidate binary SMBH with masses 8×10^8 and 2×10^7 inferred to be separated by only 0.02 mas (0.1 pc) (Boroson & Lauer 2009). Wrobel & Laor (2009) reported detection of two 8.5 GHz radio continuum sources separated by $0''.97$ (5.1 kpc) within the aperture of the

original spectroscopic observations, suggesting this is another kpc-scale dual AGN system. However, further observations show the second radio source is an elliptical galaxy that is not the origin of the red- or blue-shifted Balmer lines (Lauer & Boroson 2009). Another possibility is that SDSS J153636.22+044127.0 is similar to other “double-peak” AGNs such as 3C 390.3 and Arp 102B, which were also promoted as candidate binary AGNs but later found to be more consistent with a rapidly rotating accretion disk within a single broad-line region (Gaskell 2010). Additional observations are needed to distinguish between these alternate hypotheses.

Table 10 lists basic parameters for the small number of confirmed dual AGNs and putative binary AGNs discussed above. Due to the high degree of uncertainty in age dating mergers with factors such as nuclear separation, the morphology of tidal debris, and varying techniques applied in the simulations of specific systems, we propose a merger sequence based on the quantitative parameter $L_{\text{x}}/L_{\text{ir}}$, where L_{x} is the 2-10 keV hard X-ray from *XMM* where available, otherwise the 2-7 keV band from *Chandra*. According to the evolutionary paradigm whereby ULIRGs transform into UV/optical QSOs during the merger of gas-rich galaxies (Sanders et al. 1988a,b), the degree to which the luminous optical/UV/X-ray emission from the accretion disk is obscured should diminish as superwinds driven by star formation and/or AGNs diffuse or expel the dust from the system. To the extent that increasing $\log(L_{\text{x}}/L_{\text{ir}})$, given in parenthesis below, is a reliable gauge of the degree to which the embedded AGN-powered UV/X-ray sources have emerged from their obscuring cocoons, a presumptive sequence is: Mrk 171 (-4.1) \rightarrow Mrk 266 (-3.5) \rightarrow NGC 6240 (-3.1) \rightarrow Mrk 463 (-2.8) \rightarrow COSMOS J100043.15 + 020637.2 (-1.7)³⁵.

Despite the growing number of kpc-scale *dual* AGNs, the number of sub-parsec *binary* AGNs in the class of 4C +37.11 remains very small. Currently SDSS J153636.22+044127.0 is the only candidate out of $\approx 17,500$ AGNs with $z < 0.70$ in the SDSS (Lauer & Boroson 2009). Similarly, a recent study of VLBA data for over 3100 radio-luminous AGNs found only one binary, the previously known 4C +37.11 (Burke-Spolaor 2011). Since major mergers provide a natural process to form binary SMBHs, the apparent dearth of binary AGNs needs explanation. Gaskell (2010) has noted two possibilities: either the lifetime of binary SMBHs is much shorter than predicted (i.e., they inspiral very rapidly rather than remaining in a stalled orbit), or fueling of the accretion disk(s) is somehow suspended. The former explanation seems unlikely because the very presence of the accretion disks forms a significant buffer against rapid inspiral and effectively “softens” the SMBH merger process. A possible physical mechanism for the latter suggestion may be that AGN jets have the potential to impart enough energy into the inner parsecs of a galaxy to impede gas inflow to the accretion disk (Nagar et al. 2005). We propose another physically viable alternative: If dual AGNs are confirmed in many more (U)LIRGs in inter-

³⁴ However, it should be noted that many pairs with such wide separations may not be gravitationally bound, and a hard X-ray selected sample is naturally biased toward a much higher AGN fraction than an infrared-selected sample. The number of confirmed dual AGNs is currently less than 3% of the GOALS sample.

³⁵ SDSS J153636.22+044127.0 is omitted from the proposed sequence because its nature as a true binary AGN is controversial, and the required IR and X-ray measurements are not yet available.

Table 10
Dual to Binary AGN Evolution Based on $L_x(\text{Hard})/L_{\text{IR}}$

| Object | z | D_L (Mpc) | Sep ($''$) | Sep (kpc) | $\log(\frac{L_{\text{IR}}}{L_{\odot}})$ (km/s) | $\log(\frac{L_x(\text{Hard})}{L_{\text{IR}}})$ | Notes | Refs |
|-----------------------------|---------|----------------|-----------------|------------------|---|--|---------------------|------|
| (1) | (2) | (3) | (4) | (5) | (6) | (7) | (8) | (9) |
| Mrk 171 (NGC 3690 + IC 694) | 0.01041 | 51.1 | 3.8 | 0.9 | 11.88 | -4.1 | ... | 1 |
| Mrk 266 (NGC 5256) | 0.02786 | 129 | 10 | 6.0 | 11.53 | -3.5 | ... | 2 |
| NGC 6240 | 0.02448 | 116 | 1.8 | 0.9 | 11.93 | -3.1 | ... | 3 |
| Mrk 463 | 0.05036 | 233 | 3.8 | 3.8 | 11.77 | -2.8 | Young radio jet? | 4 |
| 3C 75 | 0.02315 | 97.9 | 14 | 6.4 | ... | ... | Twin radio jets | 5 |
| COSMOS J100043.15+020637.2 | 0.36060 | 1944 | 0.5 | 2.5 | 11.59 | -1.7 | Recoiling SMBH? | 6 |
| 4C +37.11 | 0.05500 | 242 | 0.0073 | 0.008 | ... | ... | Binary AGN | 7 |
| SDSS J153636.22+044127.0 | 0.38930 | 2133 | 1.0? | 10^{-4} or 5.1 | ... | ... | Binary or dual AGN? | 8,9 |

Note. — Basic parameters for confirmed dual AGNs and putative binary AGNs. Column (1): Object name. Column (2): Heliocentric redshift from NED (see citations therein). Column (3): Luminosity distance computed by NED. Column (4): Projected nuclear separation in arcseconds. Column (5): Projected separation in kpc. Column (6): Log of the infrared luminosity in Solar units. Column (7): Log of the ratio of observed hard X-ray luminosity (2-10 keV from XMM, otherwise 2-7 keV from Chandra, uncorrected for absorption) to infrared luminosity. Column (8): Notes. Column (9): References for the redshift in column (2), the hard X-ray flux used to compute the ratio in column (7), or the Notes in column (8); the codes are as follows: 1 = Ballo et al. (2004); 2 = this article; 3 = Komossa et al. (2003); 4 = Bianchi et al. (2008); 5 = Owen et al. (1985); 6 = Civano et al. (2010); 7 = Rodriguez et al. (2006); 8 = Boroson & Lauer (2009); 9 = Wrobel & Laor (2009). Measurements taken from the literature have been adjusted to $H_0 = 70 \text{ km s}^{-1} \text{ Mpc}^{-1}$, $\Omega_M = 0.27$, $\Omega_V = 0.73$. For COSMOS J100043.15+020637.2, L_{IR} was estimated from the *Spitzer* IRAC 8 μm and MIPS 24 μm measurements in Civano et al. (2010) utilizing equation 1 of the current study.

mediate stages of the merger process with kpc scale separations (i.e., if most of the LINERs in the GOALS and IRAS 1 Jy ULIRG samples are confirmed to be ionized by a power-law source as suggested by the radio observations of Nagar et al. (2003)), this raises the possibility that there will be an insufficient fuel supply remaining to power luminous binary AGNs late in the merger process.

The lifetime of nuclear starbursts and AGNs is inversely proportional to the efficiency of gas depletion and ranges between $\sim 10^7$ yr for ULIRGs and $\sim 10^8$ yr for LIRGs (e.g., Solomon & Vanden Bout 2005). The lifetime of powerful radio-loud AGNs has also been estimated to be only $\sim 10^7$ yr (Bird et al. 2008). This is similar to the dynamical time scale of the final coalescence of the nuclei with high circular velocity at the core of a merger, but only 1-10% of the $\sim 10^9$ Gyr time scale for dynamical relaxation of the stars in outer orbits of the remnant galaxy (e.g., Mihos 1999). Therefore, it is possible that starbursts and dual AGNs may consume or expel the bulk of available gas relatively early in many major mergers, leaving insufficient fuel to power QSOs that can be detected spectroscopically through the stage when the SMBHs inspiral to form a true binary and then coalesce or recoil. This hypothesis counters simulations that find AGN accretion rates peak during the SMBH coalescence (e.g., Johansson et al. 2009).

4. SUMMARY AND CONCLUSIONS

We have presented the results of a multi-wavelength campaign on the luminous infrared galaxy (LIRG) system Markarian 266 that has yielded the following conclusions regarding the morphology, nuclei, dust, molecular gas, outflows, star clusters, and radiation between the nuclei, as well as implications for a better understanding of the origin of ULIRGs and binary AGNs.

1. *HST* images show that the “double-nucleus galaxy” observed in low-resolution images is a strongly interacting pair; we classify the SW and NE galaxies as SBb (pec) and S0/a (pec), respectively. Deeper imaging reveals asymmetric tidal debris spanning ≈ 100 kpc. At H band, the companions are more luminous than L^* galax-

ies, and their estimated stellar masses are $6.1 \times 10^{10} M_{\odot}$ (SW) and $4.4 \times 10^{10} M_{\odot}$ (NE). The stellar bulge luminosities imply remarkably similar nuclear black hole masses of $2 \times 10^8 M_{\odot}$.

2. The NE (LINER) nucleus is emitting 6.4 times more hard X-ray (2-7 keV) flux than the SW (Seyfert 2) nucleus, yet the luminosity of the NE galaxy is only $\approx 20\%$ of the SW galaxy at 24 μm and in CO (1-0) molecular gas emission. The *Chandra* spectra indicate that the SW nucleus is likely the primary source of a bright Fe K α line detected in the *XMM* spectrum of the total system, consistent with a reflection-dominated X-ray spectrum of a heavily obscured AGN. The F(X-ray)/F([O III]) flux ratios also indicate the SW nucleus is much more heavily obscured than the NE nucleus.

3. Soft (0.4-2 keV) X-ray emission extends 15 kpc to the north of the system, between the nuclei, and 3 kpc west of the SW nucleus. The smoothed X-ray structure corresponds remarkably well with filaments in H α and [O III] images. A ridge of X-ray emission between the galaxies has an X-ray spectrum consistent with $T \sim 10^7$ K shock-heated gas, strengthening the idea that the corresponding radio emission is shock-induced synchrotron radiation. The lack of detected 9.7 μm H₂ S(3) line emission supports the suggestion that a very fast shock at the interface of superwinds expanding from the two galaxies might generate the observed non-thermal radio continuum emission and heat the gas above the dissociation temperature of H₂. The derived cooling time of the X-ray emitting gas between the nuclei is only ≈ 4 Myr.

4. The *HST* optical images reveal a circumnuclear arc containing three knots 240 pc west of the NE nucleus. The arc is embedded within B-band emission with a filamentary, bi-conic morphology extending over a radius of 1.2 kpc. This region appears to be dominated by nebular emission from the narrow-line region of a double-sided AGN ionization cone. Radio continuum emission at 1.6 GHz peaks at the optical/near-IR nucleus and has components in alignment with the nucleus and the circumnuclear B-band knots (PA=56 $^\circ$). A plausible explanation

is that the optical knots are clouds entrained in a shock front produced by an AGN-powered collimated plasma outflow (jet). We liken this region to the radiative bow shock 230 pc south of the LINER in M51.

5. Mid-IR spectral diagnostics suggest the bolometric luminosity is powered by roughly an equal mixture of radiation from AGNs and star formation, with substantial scatter among the various methods. Newly constructed SEDs give infrared luminosities of $L_{\text{ir}} = (2.3, 0.7, 3.4) \times 10^{11} L_{\odot}$ for the SW, NE, and total system respectively. Decomposition of the SED of the total system indicates that cold (26 K), cool (72 K), warm (235 K) and hot (~ 1500 K) thermal dust components contribute approximately 57%, 20%, 12%, and 11% of the bolometric luminosity, respectively. The total cold dust mass estimate is $1.5(\pm 0.4) \times 10^8 M_{\odot}$.

6. *HST* imaging resolves the Northern Loop extending 6-20 kpc from the galaxies into a fragmented morphology suggestive of Rayleigh-Taylor instabilities. A few structures 300-600 pc in length are radially aligned with the NE nucleus, suggestive of bow shocks predicted by hydrodynamic simulations of galactic superwinds. Detection of $24 \mu\text{m}$ emission in the Northern Loop implies that at least $\sim 2 \times 10^7 M_{\odot}$ of dust is being swept out of the system by the superwind during a “blow-out” phase that is well underway prior to the final galaxy merger.

7. Approximately 120 star clusters detected with *HST* are concentrated in the SW galaxy and at the base of the Northern Loop; most have estimated ages less than 50 Myr and masses of $\sim 10^5 M_{\odot}$. The ratios of cluster surface densities, L_{CO} and L_{ir} within 3 kpc of each nucleus are similar (i.e., $L(\text{SW})/L(\text{NW}) \approx 4 - 5$). The star cluster luminosity function is similar to what has been found in other LIRGs, and the unobscured clusters contribute little to powering the total infrared luminosity.

8. We conclude that Mrk 266 NE is an AGN based on the presence of: (1) an obscured, hard X-ray point source; (2) a radiative bow shock aligned with ionization cones and apparent radio plasma outflow; (3) PAH emission with small equivalent widths and a deficiency of 6.2 and $7.7 \mu\text{m}$ flux relative to $11.3 \mu\text{m}$ flux; and (4) a $\text{H}_2(1-0) \text{S}(1)$ to $\text{Br}\gamma$ flux ratio of 3.5. The spatially extended H_2 emission demonstrates that LINERs can exhibit strong signatures of an AGN and shock excitation.

9. The bulk of the CO (1-0) emission in the system is aligned with the major axis of the SW galaxy. HCN (1-0) is aligned with $\text{H}_2 \text{S}(3)$ $9.7 \mu\text{m}$ emission in the nucleus of Mrk 266 NE. However, the CO (1-0) and HCO+ (1-0) emission peaks are located ~ 1 kpc SE of the NE nucleus, suggesting that either most of the cold molecular gas has already been stripped from the NE galaxy, or gas is being transferred from the SW galaxy to the NE galaxy. Approximately 40% of the total CO (1-0) emission is bridging the galaxies, likely in-falling toward the center of mass or transferring between the galaxies. In this regard, Mrk 266 appears to be in an evolutionary stage similar to VV 114, NGC 6090, and NGC 6240.

10. Two lines of evidence suggest Mrk 266 may evolve into a ULIRG: First, in the context of merger simulations, the galaxies lie within an asymmetric, low surface-brightness halo of tidal debris spanning ≈ 100 kpc, with a projected separation of 6 kpc and a relative velocity of only 135 km s^{-1} , indicating they are likely undergoing

their second or third encounter with only 50 to 250 Myr remaining until they merge via tidal dissipation. Therefore, Mrk 266 appears to be in a short-lived stage when the nuclei are about to enter the final phase of coalescence characteristic of ULIRGs. Second, the total cold molecular gas mass of $\approx 7 \times 10^9 M_{\odot}$ is similar to local and high-redshift ULIRGs. Since $\approx 40\%$ of the total CO (1-0) emission is located between the galaxies, this reservoir is available to form more stars and to fuel the AGNs as the stellar systems and nuclei inexorably coalesce.

11. We propose that Mrk 266 belongs to an evolutionary sequence in which *dual AGNs* with kpc separations represent precursors to putative *binary AGNs* with pc scale orbital radii. In this scenario, where Mrk 266 is in an intermediate phase between Mrk 171 and NGC 6240, the global $L_{\text{x}}/L_{\text{ir}}$ ratio increases by over four orders of magnitude as obscuring material is expelled by outflows to gradually expose previously obscured AGNs.

12. Since major mergers provide a natural process to form SMBH/AGN pairs, the scarcity of confirmed and candidate binary QSOs in large spectroscopic and VLBI surveys is unexpected. While two possibilities are raised in the literature, that either the SMBHs inspiral very rapidly, or fueling of the accretion disks is quenched during the binary phase, we propose a third hypothesis. Since the gas-depletion lifetime of ULIRGs and LIRGs is 10-100 times shorter than the time-scale for creation of a binary SMBH ($\gtrsim 1$ Gyr), it is possible that, in most instances, the gas will be consumed by star formation and accretion during a dual AGN phase long before the SMBHs inspiral to sub-pc separation.

This work is based on observations with the following facilities: the *Spitzer Space Telescope*, which is operated by the Jet Propulsion Laboratory, California Institute of Technology under a contract with NASA; the NASA/ESA *Hubble Space Telescope*, which is operated by the Association of Universities for Research in Astronomy, Inc. under NASA contract NAS5-26555; the *Chandra* X-ray Observatory Center, which is operated by the Smithsonian Astrophysical Observatory for and on behalf of NASA under contract NAS8-03060; and the *Galaxy Evolution Explorer (GALEX)*, which is operated for NASA by the California Institute of Technology under NASA contract NAS5-98034. The *Aladin* (CDS, Strasbourg) and *SAOImage DS9* tools were used for image analysis. Support for this work was provided by the following NASA grants: an award issued by JPL/Caltech (*Spitzer* PID 3672, PI J. Mazzarella); HST-GO10592.01-A (ACS imaging, PI A. Evans) and program 11235 (NICMOS imaging, PI J. Surace) issued by the STScI. This research made use of the NASA/IPAC Extragalactic Database (NED) and the Infrared Science Archive (IRSA), which are operated by the Jet Propulsion Laboratory, California Institute of Technology, under contract with NASA. We thank Masa Imanishi for providing FITS files for the Nobeyama Millimeter Array observations and Tsuyoshi Ishigaki for supplying optical emission-line images. We thank Chris Mihos for helpful discussions regarding merger time-scales. Finally, we thank the anonymous referee for very helpful comments that led to improvements to the manuscript.

Table 11
Elliptical Apertures for Regions of Interest

| Region (1) | RA, DEC (J2000) (2) | a'' (3) | b'' (4) | PA° (5) |
|------------------|---------------------------|------------|------------|------------|
| SW | (13:38:17.28,+48:16:32.1) | 5.0 | 3.0 | 120 |
| NE | (13:38:17.79,+48:16:41.2) | 5.0 | 3.0 | 120 |
| Between Galaxies | (13:38:17.51,+48:16:36.8) | 6.0 | 2.0 | 115 |
| Northern Loop | (13:38:17.54,+48:16:56.0) | 17.0 | 7.5 | 40 |
| Total System | (13:38:17.66,+48:16:35.8) | 40.0 | 40.0 | ... |

Note. — Parameters for elliptical apertures used for photometric measurements, as illustrated in Fig. 31.

Facilities: CXO (ACIS-S), XMM-Newton (EPIC pn, OM), GALEX (FUV, NUV), HST(ACS, NICMOS), UH:2.2m (), Spitzer(IRAC, MIPS, IRS)

Objects: Mrk 266, Mrk 266 SW, Mrk 266 NE

5. APPENDIX

5.1. Photometric Data for Mrk 266

Figure 31 displays regions parameterized in Table 11 that were used to perform aperture photometry tabulated in Tables 12 and 13, as plotted in Figure 9 (§2.6.2).

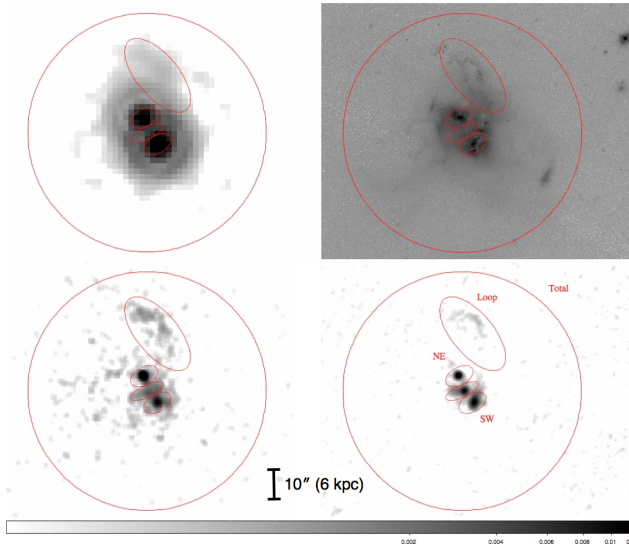


Figure 31. The regions used to perform aperture photometry of the nuclei, central region, and Northern Loop superposed on the 24 μm *Spitzer* MIPS image (upper left), the HST ACS B band image (upper right), the *Chandra* full-band X-ray image (lower left), and the 20 cm radio continuum image (lower right). All four images are shown at the same scale and orientation.

5.2. Clarification of Regions Covered in Published *Spitzer* IRS Data for Mrk 266

As noted in §2.7, mid-IR spectroscopy of Mrk 266 obtained in staring mode with the *Spitzer* IRS is complicated due to aperture affects. To facilitate interpretation of the IRS spectroscopy published to date, the available observations are summarized here, and Table 14 provides clarification of which emission features have been measured for each component of the system.

In the low spectral resolution (R 65-130) observations (AOR #3755264; GTO program P00014; PI J. Houck), the Short-Low (SL, 5.2-14.5 μm) aperture of the IRS

Table 12
Photometric Data for Mrk 266 - Total System

| Bandpass (1) | ν (Hz) (2) | f_ν (Jy) (3) | σ_{f_ν} (Jy) (4) | Ref. (5) |
|-------------------------------|-------------------|---------------------|------------------------------|-------------|
| 2-10 keV (ASCA) | 1.45E+18 | 2.48E-08 | 5.0E-09 | 2 |
| 2.0-7.0 keV (XMM) | 1.09E+18 | 2.11E-08 | 6.3E-09 | 1 |
| 0.7-7 keV (ASCA) | 9.31E+17 | 3.65E-08 | 7.3E-09 | 2 |
| 0.5-2.0 keV (XMM) | 3.02E+17 | 5.96E-08 | 1.2E-08 | 1 |
| GALEX FUV | 1.96E+15 | 7.94E-04 | 3.1E-05 | 1 |
| XMM-OM UVW2 | 1.41E+15 | 2.06E-03 | 8.0E-04 | 1 |
| GALEX NUV | 1.32E+15 | 1.63E-03 | 3.4E-05 | 1 |
| XMM-OM UVW1 | 1.03E+15 | 2.12E-03 | 2.6E-04 | 1 |
| XMM-OM U | 8.71E+14 | 3.87E-03 | 1.4E-03 | 1 |
| HST ACS F435W (B) | 6.89E+14 | 8.92E-03 | 4.1E-05 | 1 |
| V (Johnson) | 5.42E+14 | 1.82E-02 | 8.6E-04 | 3 |
| LW2 (ISOCAM) | 4.44E+13 | 1.14E-01 | 1.4E-02 | 4 |
| R (Johnson) | 4.28E+14 | 2.86E-02 | 8.0E-04 | 3 |
| HST ACS F814W (I) | 3.68E+14 | 2.97E-02 | 5.5E-05 | 1 |
| 2MASS J (1.2 μm) | 2.43E+14 | 5.44E-02 | 6.5E-04 | 1 |
| 2MASS H (1.6 μm) | 1.80E+14 | 6.42E-02 | 8.8E-04 | 1 |
| 2MASS Ks (2.2 μm) | 1.39E+14 | 6.02E-02 | 8.3E-04 | 1 |
| Spitzer 3.6 μm | 8.44E+13 | 3.82E-02 | 5.7E-03 | 1 |
| Spitzer 4.5 μm | 6.67E+13 | 3.05E-02 | 4.6E-03 | 1 |
| Spitzer 5.8 μm | 5.23E+13 | 6.80E-02 | 1.0E-02 | 1 |
| Spitzer 8.0 μm | 3.81E+13 | 1.79E-01 | 2.7E-02 | 1 |
| IRAS 12 μm | 2.50E+13 | 3.20E-01 | 1.8E-02 | 5 |
| Spitzer 24 μm | 1.27E+13 | 9.55E-01 | 1.9E-01 | 1 |
| IRAS 25 μm | 1.20E+13 | 1.07E+00 | 2.8E-02 | 5 |
| IRAS 60 μm | 5.00E+12 | 7.25E+00 | 3.3E-02 | 5 |
| Spitzer 70 μm | 4.20E+12 | 8.95E+00 | 1.8E+00 | 1 |
| IRAS 100 μm | 3.00E+12 | 1.01E+01 | 1.4E-01 | 5 |
| Spitzer 160 μm | 1.92E+12 | 6.41E+00 | 1.3E+00 | 1 |
| 170 μm (ISO) | 1.76E+12 | 8.73E+00 | 2.6E+00 | 6 |
| SCUBA 850 μm | 3.53E+11 | 8.20E-02 | 1.7E-02 | 7 |
| 20.0 GHz (OVRO) | 2.00E+10 | 1.49E-02 | 1.3E-03 | 8 |
| 4.85 GHz | 4.85E+09 | 4.70E-02 | 7.1E-03 | 9 |
| 1.46 GHz (VLA) | 1.46E+09 | 1.07E-01 | 6.2E-03 | 8 |
| Texas 365 MHz | 3.65E+08 | 3.53E-01 | 4.3E-02 | 10 |
| 151 MHz (6C) | 1.52E+08 | 5.90E-01 | 4.0E-02 | 11 |

Note. — Reference codes in Column (5): 1=New measurements in this article; 2=Ueda et al. (2005); 3=Huchra (1977); 4=Ramos Almeida et al. (2007); 5=Sanders et al. (2003); 6=Stickel et al. (2004); 7=Dunne et al. (2000); 8=Edelson (1987); 9=Becker et al. (1991); 10=Douglas et al. (1996); 11=Hales et al. (1990).

contained Mrk 266 NE (off center), and missed both Mrk 266 SW and the central radio/X-ray source; the Long-Low (LL, 14–38 μm) slit contained Mrk 266 SW and the radio/X-ray source between the nuclei, but it missed Mrk 266 NE. Neither aperture had the orientation required to sample the Northern Loop. The low-resolution IRS spectrum displayed in Brandl et al. (2006) is therefore a mixture of emission from Mrk 266 NE in the 5-14 μm region with emission from Mrk 266 SW (and the radio/X-ray source between the nuclei) in the 14-38 μm region.

AOR #3755264 also contained high-resolution observations (spectral resolution ~ 600). Dudik et al. (2007, Fig. 8) plotted the SH and LH apertures of these observations as an overlay on a 20 cm image, although they did not present the resulting spectra; their diagram clearly illustrates the aperture affects that complicate the interpretation of IRS spectra for this system. The SH slit contained only the radio source between the nuclei (missing both nuclei), while the LH slit contained 266 SW and the central radio source but it missed Mrk 266 NE. Observations with the SH (9.9 - 19.6 μm) module were also obtained on 2005 January 10 in *Spitzer* program P03237 (PI. E. Sturm, AOR #10510592); these data cover the SW nucleus, but not the NE nucleus. The available high-

Table 13
Photometric Data for Mrk 266 - Components

| Bandpass (1) | ν (Hz) (2) | f_ν (Jy) (3) | σ_{f_ν} (Jy) (4) | Ref. (5) |
|----------------------------------|-------------------|---------------------|------------------------------|-------------|
| Mrk 266 SW | | | | |
| 2.0-7.0 keV | 1.09E+18 | 2.02E-09 | 6.1E-10 | 1 |
| 0.5-2.0 keV | 3.02E+17 | 7.28E-09 | 1.5E-09 | 1 |
| XMM-OM UVW2 | 1.41E+15 | 1.68E-04 | 1.1E-05 | 1 |
| XMM-OM UVW1 | 1.03E+15 | 2.72E-04 | 5.4E-05 | 1 |
| XMM-OM U | 8.71E+14 | 5.12E-04 | 2.2E-05 | 1 |
| HST ACS F435W (B) | 6.89E+14 | 1.31E-03 | 1.2E-05 | 1 |
| HST ACS F814W (I) | 3.68E+14 | 5.03E-03 | 2.3E-05 | 1 |
| 2MASS J (1.2 μ m) | 2.43E+14 | 1.04E-02 | 2.5E-04 | 1 |
| NICMOS H (1.6 μ m) | 1.87E+14 | 1.45E-02 | 1.7E-04 | 1 |
| 2MASS H (1.6 μ m) | 1.80E+14 | 1.46E-02 | 3.3E-04 | 1 |
| 2MASS Ks (2.2 μ m) | 1.39E+14 | 1.53E-02 | 3.1E-04 | 1 |
| Spitzer 3.6 μ m | 8.44E+13 | 1.50E-02 | 2.3E-03 | 1 |
| Spitzer 4.5 μ m | 6.67E+13 | 1.47E-02 | 2.2E-03 | 1 |
| Spitzer 5.8 μ m | 5.23E+13 | 4.59E-02 | 6.9E-03 | 1 |
| Spitzer 8.0 μ m | 3.81E+13 | 1.28E-01 | 1.9E-02 | 1 |
| Spitzer 24 μ m | 1.27E+13 | 5.91E-01 | 1.2E-01 | 1 |
| Spitzer 70 μ m ^a | 4.20E+12 | 6.01E+00 | 1.2E+00 | 1 |
| Spitzer 160 μ m ^a | 1.92E+12 | 4.30E+00 | 8.6E-01 | 1 |
| 2 cm | 1.50E+10 | 4.90E-03 | 7.0E-04 | 12 |
| 6 cm | 4.89E+09 | 1.01E-02 | 5.0E-04 | 12 |
| 20 cm | 1.47E+09 | 3.24E-02 | 1.4E-03 | 12 |
| Mrk 266 NE | | | | |
| 2.0-7.0 keV | 1.09E+18 | 1.29E-08 | 3.9E-09 | 1 |
| 0.5-2.0 keV | 3.02E+17 | 9.93E-09 | 2.0E-09 | 1 |
| XMM-OM UVW2 | 1.41E+15 | 2.45E-04 | 2.0E-05 | 1 |
| XMM-OM UVW1 | 1.03E+15 | 3.63E-04 | 9.1E-05 | 1 |
| XMM-OM U | 8.71E+14 | 6.49E-04 | 3.0E-05 | 1 |
| HST ACS F435W (B) | 6.89E+14 | 1.59E-03 | 1.5E-05 | 1 |
| HST ACS F814W (I) | 3.68E+14 | 6.02E-03 | 2.8E-05 | 1 |
| 2MASS J (1.2 μ m) | 2.43E+14 | 9.62E-03 | 2.4E-04 | 1 |
| NICMOS H (1.6 μ m) | 1.87E+14 | 1.22E-02 | 1.6E-04 | 1 |
| 2MASS H (1.6 μ m) | 1.80E+14 | 1.22E-02 | 3.0E-04 | 1 |
| 2MASS Ks (2.2 μ m) | 1.39E+14 | 1.09E-02 | 2.6E-04 | 1 |
| Spitzer 3.6 μ m | 8.44E+13 | 7.35E-03 | 1.1E-03 | 1 |
| Spitzer 4.5 μ m | 6.67E+13 | 5.90E-03 | 8.9E-04 | 1 |
| Spitzer 5.8 μ m | 5.23E+13 | 9.57E-03 | 1.4E-03 | 1 |
| Spitzer 8.0 μ m | 3.81E+13 | 2.23E-02 | 3.3E-03 | 1 |
| Spitzer 24 μ m | 1.27E+13 | 3.28E-01 | 6.6E-02 | 1 |
| Spitzer 70 μ m ^a | 4.20E+12 | 1.74E+00 | 7.0E-01 | 1 |
| Spitzer 160 μ m ^a | 1.92E+12 | 1.25E+00 | 5.0E-01 | 1 |
| 2 cm | 1.50E+10 | 4.10E-03 | 6.0E-04 | 12 |
| 6 cm | 4.89E+09 | 1.22E-02 | 4.0E-04 | 12 |
| 20 cm | 1.47E+09 | 2.35E-02 | 1.0E-03 | 12 |
| Between the Nuclei | | | | |
| 2.0-7.0 keV | 1.09E+18 | 9.19E-10 | 2.8E-10 | 1 |
| 0.5-2.0 keV | 3.02E+17 | 8.60E-09 | 1.7E-09 | 1 |
| 2 cm | 1.50E+10 | 2.70E-03 | 5.0E-04 | 12 |
| 6 cm | 4.89E+09 | 6.00E-03 | 2.7E-03 | 12 |
| 20 cm | 1.47E+09 | 2.15E-02 | 9.0E-04 | 12 |
| Northern Loop | | | | |
| 0.5-2.0 keV | 3.02E+17 | 4.63E-09 | 9.3E-10 | 1 |
| XMM-OM UVW2 | 1.41E+15 | 1.94E-04 | 1.7E-06 | 1 |
| XMM-OM UVW1 | 1.03E+15 | 2.10E-04 | 4.8E-06 | 1 |
| XMM-OM U | 8.71E+14 | 4.28E-04 | 3.0E-05 | 1 |
| HST ACS F435W (B) | 6.89E+14 | 8.84E-04 | 1.6E-05 | 1 |
| HST ACS F814W (I) | 3.68E+14 | 2.50E-03 | 2.1E-05 | 1 |
| Spitzer 24 μ m | 1.27E+13 | 3.62E-02 | 7.2E-03 | 1 |
| 20 cm | 1.47E+09 | 2.60E-03 | 5.0E-05 | 12 |

Note. — The reference codes in Column (5) are as follows: 1=New measurements in this article; 12=Mazzarella et al. (1988).

^a The 70 and 160 μ m flux densities for the SW and NE galaxies were estimated using the 8 and 24 μ m measurements as described in the text.

Table 14
Regions Covered in Published IRS Measurements

| Feature (1) | Flux ($W m^{-2}$) (2) | EQW (μ m) (3) | Ref. (4) |
|--|-----------------------------------|-----------------------|-------------|
| Mrk 266 SW | | | |
| [S IV] 10.51 μ m (SH) | $9.00(\pm 0.38) \times 10^{-21}$ | ... | B09 |
| PAH 10.6 μ m (SH) | $0.25(\pm 0.05) \times 10^{-20}$ | ... | B09 |
| PAH 10.7 μ m (SH) | $0.12(\pm 0.03) \times 10^{-20}$ | ... | B09 |
| PAH 11.0 μ m (SH) | $1.09(\pm 0.05) \times 10^{-20}$ | ... | B09 |
| PAH 11.3 μ m (SH) | $14.90(\pm 0.74) \times 10^{-20}$ | ... | B09 |
| PAH 12.0 μ m (SH) | $0.73(\pm 0.10) \times 10^{-20}$ | ... | B09 |
| H ₂ S(2) 12.28 μ m (SH) | $3.72(\pm 0.32) \times 10^{-21}$ | ... | B09 |
| HI (7-6) 12.37 μ m (SH) | $0.69(\pm 0.05) \times 10^{-21}$ | ... | B09 |
| PAH 12.74 μ m (SH) | $7.13(\pm 0.36) \times 10^{-20}$ | ... | B09 |
| [Ne II] 12.81 μ m (SH) | $57.04(\pm 1.64) \times 10^{-21}$ | ... | B09 |
| PAH 13.5 μ m (SH) | $0.13(\pm 0.06) \times 10^{-21}$ | ... | B09 |
| PAH 14.2 μ m (SH) | $0.57(\pm 0.06) \times 10^{-20}$ | ... | B09 |
| [Ne V] 14.32 μ m (SH) | $7.96(\pm 0.17) \times 10^{-21}$ | ... | B09 |
| [Cl II] 14.38 μ m (SH) | $0.46(\pm 0.07) \times 10^{-21}$ | ... | B09 |
| [Ne III] 15.55 μ m (SH) | $27.95(\pm 0.76) \times 10^{-21}$ | ... | B09 |
| PAH 16.45 μ m (SH) | $0.84(\pm 0.08) \times 10^{-20}$ | ... | B09 |
| PAH 17.0 μ m (SH) | $1.07(\pm 0.14) \times 10^{-20}$ | ... | B09 |
| H ₂ S(1) 17.03 μ m (SH) | $8.40(\pm 0.97) \times 10^{-21}$ | ... | B09 |
| [P III] 17.89 μ m (SH) | $0.67(\pm 0.15) \times 10^{-21}$ | ... | B09 |
| [Fe II] 17.95 μ m (SH) | $0.48(\pm 0.14) \times 10^{-21}$ | ... | B09 |
| [S III] 18.71 μ m (SH) | $24.33(\pm 0.69) \times 10^{-21}$ | ... | B09 |
| Mrk 266 SW + Source Between Nucleus | | | |
| [Ne III] 15.55 μ m (LL) ^a | ... | ... | B06 |
| PAH 17.0 μ m (LL) | 0.51×10^{-19} | 0.403 | B06 |
| [S III] 18.71 μ m (LL) ^a | ... | ... | B06 |
| [Fe III] 22.93 μ m (LH) | $2.15(\pm 0.29) \times 10^{-21}$ | ... | B09 |
| [Ne V] 24.31 μ m (LH) ^b | $11.12(\pm 0.59) \times 10^{-21}$ | ... | B09 |
| [O IV] 25.89 μ m (LH) | $52.94(\pm 5.66) \times 10^{-21}$ | ... | B09 |
| [O IV] 25.89 μ m (LL) ^a | ... | ... | B06 |
| [Fe II] 25.98 μ m (LH) | $4.35(\pm 0.70) \times 10^{-21}$ | ... | B09 |
| S ₂ S(0) 28.22 μ m (LH) | $< 1.60 \times 10^{-21}$ | ... | B09 |
| [S III] 33.48 μ m (LH) | $50.92(\pm 2.91) \times 10^{-21}$ | ... | B09 |
| [S III] 33.48 μ m (LL) ^a | ... | ... | B06 |
| [Si II] 34.81 μ m (LH) | $87.02(\pm 4.44) \times 10^{-21}$ | ... | B09 |
| Mrk 266 NE | | | |
| PAH 6.2 μ m (SL) | 0.59×10^{-19} | 0.619 | B06 |
| PAH 7.7 μ m (SL) | 0.92×10^{-19} | 0.467 | B06 |
| PAH 8.6 μ m (SL) | ... | 0.126 | B06 |
| H ₂ S(3) 9.665 μ m (SL) ^a | ... | ... | B06 |
| [S IV] 10.51 μ m (SH) ^a | ... | ... | B06 |
| H ₂ S(2) 12.279 μ m (SL) ^a | ... | ... | B06 |
| [Ne II] 12.81 μ m (SL) ^a | ... | ... | B06 |
| PAH 11.3 μ m (SL) | 0.47×10^{-19} | 0.422 | B06 |
| PAH 14.2 μ m (SL) | 0.08×10^{-19} | 0.065 | B06 |

Note. — Column (1): Spectral line identification followed in parentheses by the IRS module used: SL = 5.2-14.5 μ m, 3''7x57'', R ~ 60-127; LL = 14.0-38.0 μ m, 10''5x168''3, R ~ 57-126; SH = 9.9-19.6 μ m, 4''7x11''3, R ~ 600; LH = 18.7-37.3 μ m, 11''1x22''3, R ~ 600. Column (2): Flux in $W cm^{-2}$. Column (3): Equivalent width in μ m. Column (4): Reference: B06 = Brandl et al. (2006); B09 = Bernard-Salas et al. (2009).

^a These features are visible in the low-res spectrum published by Brandl et al. (2006), but fluxes were not published.

^b This is consistent with a [Ne V] 24.32 μ m flux of $1.19(\pm 0.06) \times 10^{-20} W cm^{-2}$ measured from the same LH aperture by Dudik et al. (2007, Table 2).

resolution spectra were published in an atlas of *Spitzer* spectra for a sample of starburst galaxies (Bernard-Salas et al. 2009).

Table 15 — *Continued*

| SC# | δ R.A. | δ Dec | B | σ | M_B | I | σ | B-I | σ |
|-----|---------------|----------------|------------|------------|------------|------------|------------|------------|-------------|
| (1) | ss.ss (2) | mm ss.s (3) | mag (4) | mag (5) | mag (6) | mag (7) | mag (8) | mag (9) | mag (10) |
| 111 | 15.77 | 16 44.5 | 26.76 | 0.12 | -8.85 | 24.62 | 0.05 | 2.11 | 0.13 |
| 112 | 17.22 | 16 44.0 | 26.77 | 0.21 | -8.84 | 25.77 | 0.41 | 0.97 | 0.46 |
| 113 | 16.42 | 16 46.4 | 26.85 | 0.16 | -8.76 | 25.87 | 0.19 | 0.95 | 0.25 |
| 114 | 16.04 | 16 21.8 | 26.89 | 0.12 | -8.72 | 26.14 | 0.16 | 0.72 | 0.20 |
| 115 | 16.78 | 16 57.1 | 27.07 | 0.18 | -8.54 | 25.73 | 0.12 | 1.31 | 0.22 |
| 116 | 18.37 | 16 40.5 | 27.12 | 0.88 | -8.49 | 24.25 | 0.28 | 2.84 | 0.92 |
| 117 | 15.93 | 16 50.7 | 27.13 | 0.17 | -8.48 | 25.98 | 0.13 | 1.12 | 0.21 |
| 118 | 15.67 | 16 48.2 | 27.16 | 0.13 | -8.45 | 25.59 | 0.09 | 1.54 | 0.16 |
| 119 | 17.56 | 16 56.9 | 27.23 | 0.22 | -8.38 | 25.73 | 0.13 | 1.47 | 0.26 |

Note. — Column (1): Star cluster (candidate) number. Cols. (2) and (3): J2000 δ R.A. and δ Dec of the object. To save space, offsets in seconds of time in R.A. and offsets in arcminutes and arcseconds in Dec are listed. Full coordinates are obtained by adding these values to R.A.=13h38m and Dec=48d (e.g., 13h38m17.19s; 48d16m32.4s). The 1σ uncertainty in the coordinates is $\pm 0''.3$. The objects can be identified as “Mrk 266 SC###” or as “GOALS Jhhmmssss+ddmmss.” For example: Mrk 266 SC001 = GOALS J13381719+4816324. Col. (4): apparent mag in the HST ACS F435W (B) filter. Col. (5): 1σ uncertainty in the B mag. Col. (6): absolute B mag. Col. (7): apparent mag in the HST ACS F814W (I) filter. Col. (8): 1σ uncertainty in the I mag. Col. (9): B - I color mag. Col. (10): 1σ uncertainty in the B - I color mag. Absolute B mag and B-I colors have been corrected for foreground Galactic extinction using values from Schlegel et al. (1998) as provided by NED: $A_B = 0.056$ mag; $A_I = 0.025$ mag. These data have *not* been corrected for extinction within Mrk 266 (see §3.6.2).

REFERENCES

- Alton, P. B., Davies, J. I., & Bianchi, S. 1999, *A&A*, 343, 51
 Appleton, P. N., et al. 2006, *ApJ*, 639, L51
 Armus, L., Heckman, T. M., & Miley, G. K. 1990, *ApJ*, 364, 471
 Armus, L., et al. 2007, *ApJ*, 656, 148
 Armus, L.; Mazzarella, J. M.; Evans, A. S. et al. 2009, *PASP*, 121, 559
 Arnouts, S., et al. 2007, *A&A*, 476, 137
 Awaki, H., Koyama, K., Inoue, H., & Halpern, J. P. 1991, *PASJ*, 43, 195
 Ballo, L., Braitto, V., Della Ceca, R., et al. 2004, *ApJ*, 600, 634
 Barnes, J. E., & Hernquist, L. 1996, *ApJ*, 471, 115
 Bassani, L. et al. 1999, *ApJS*, 121, 473
 Becker, R. H., White, R. L., & Edwards, A. L. 1991, *ApJS*, 75, 1
 Bernard-Salas, J., et al. 2009, *ApJS*, 184, 230
 Bertin, E., & Arnouts, S. 1996, *A&AS*, 117, 393
 Bianchi, S., et al. 2008, *MNRAS*, 386, 105
 Bird, J., Martini, P., & Kaiser, C. 2008, *ApJ*, 676, 147
 Boroson, T. A., & Lauer, T. R. 2009, *Nature*, 458, 53
 Brandl, B. R., et al. 2006, *ApJ*, 653, 1129
 Brassington, N. J., Ponman, T. J., & Read, A. M. 2007, *MNRAS*, 377, 1439
 Bruzual, G., & Charlot, S. 2003, *MNRAS*, 344, 1000
 Bryant, P. M., & Scoville, N. Z. 1999, *AJ*, 117, 2632
 Burke-Spolaor, S. 2011, *MNRAS*, 410, 2113
 Calzetti, D., Kinney, A. L., & Storchi-Bergmann, T. 1994, *ApJ*, 429, 582
 Caputi, K. I., et al. 2007, *ApJ*, 660, 97
 Cecil, G. 1988, *ApJ*, 329, 38
 Civano, F., et al. 2010, *ApJ*, 717, 209
 Cluver, M. E., et al. 2010, *ApJ*, 710, 248
 Cole, S., et al. 2001, *MNRAS*, 326, 255
 Colpi, M., & Dotti, M. 2009, arXiv:0906.4339
 Comerford, J. M., Griffith, R. L., Gerke, B. F., et al. 2009, *ApJ*, 702, L82
 Condon, J. J., Helou, G., Sanders, D. B., & Soifer, B. T. 1993, *AJ*, 105, 1730
 Cooper, J. L., Bicknell, G. V., Sutherland, R. S., & Bland-Hawthorn, J. 2008, *ApJ*, 674, 157
 Cox, T. J., Jonsson, P., Primack, J. R., & Somerville, R. S. 2006, *MNRAS*, 373, 1013
 Dasyra, K. M., et al. 2008, *ApJ*, 674, L9
 Davies, R., Ward, M., & Sugai, H. 2000, *ApJ*, 535, 735
 de Propriis, R., Eisenhardt, P. R., Stanford, S. A., & Dickinson, M. 1998, *ApJ*, 503, L45
 de Vaucouleurs, G., et al. 1991, Volume 1-3, XII, Springer-Verlag Berlin Heidelberg New York (RC3)
 Douglas, J. N., et al. 1996, *AJ*, 111, 1945
 Downes, D., & Solomon, P. M. 1998, *ApJ*, 507, 615
 Draine, B. T., & Li, A. 2001, *ApJ*, 551, 807
 Dubinski, J., Mihos, J. C., & Hernquist, L. 1996, *ApJ*, 462, 576
 Dudik, R. P., et al. 2007, *ApJ*, 664, 71
 Dunne, L., Eales, S., Edmunds, M., et al. 2000, *MNRAS*, 315, 115
 Edelson, R. A. 1987, *ApJ*, 313, 651
 Engel, H., Davies, R. I., Genzel, R., et al. 2010, *A&A*, 524, A56
 Evans, A. S., Mazzarella, J. M., Surace, J. A., Frayer, D. T., Iwasawa, K., & Sanders, D. B. 2005, *ApJS*, 159, 197
 Fazio, G. G., et al. 2004, *ApJS*, 154, 10
 Ferrarese, L., & Ford, H. 2005, *Space Science Reviews*, 116, 523
 Ford, H., Crane, P., Jacoby, G., et al. 1985, *ApJ*, 293, 132
 Gaskell, C. M. 2010, *Nature*, 463, E1
 Gavazzi, G., Pierini, D., & Boselli, A. 1996, *A&A*, 312, 397
 Ghisellini, G., Haardt, F., & Matt, G. 1994, *MNRAS*, 267, 743
 Giele, M., et al. 2006, *A&A*, 450, 129
 Gonzalez-Martin, O., et al. 2006, *A&A*, 460, 45
 Graciá-Carpio, J., García-Burillo, S., & Planesas, P. 2008, *Ap&SS*, 313, 331
 Grimes, J. P., Heckman, T., Strickland, D., & Ptak, A. 2005, *ApJ*, 628, 187
 Hales, S. E. G., et al. 1990, *MNRAS*, 246, 256
 Heckman, T. M., Armus, L., & Miley, G. K. 1990, *ApJS*, 74, 833
 Hildebrand, R. H. 1983, *QJRAS*, 24, 267
 Hinshaw, G., et al. 2009, *ApJS*, 180, 225
 Ho, L. C. 2008, *ARA&A*, 46, 475
 Hony, S., Van Kerckhoven, C., et al. 2001, *A&A*, 370, 1030
 Hopkins, P. F., Hernquist, L., Cox, T. J., et al. 2006, *ApJS*, 163, 1
 Houck, J. R., et al. 2004, *ApJS*, 154, 18
 Howell, J. H., Armus, L., Mazzarella, J. M., et al. 2010, *ApJ*, 715, 572
 Huchra, J. P. 1977, *ApJS*, 35, 171
 Hutchings, J. B., Neff, S. G., & van Gorkom, J. H. 1988, *AJ*, 96, 1227
 Imanishi, M., Nakanishi, K., Tamura, Y., Oi, N., & Kohno, K. 2007, *AJ*, 134, 2366
 Imanishi, M., Nakanishi, K., Tamura, Y., & Peng, C.-H. 2009, *AJ*, 137, 3581
 Inami, H., et al. 2010, *AJ*, 140, 63
 Ishida, C. M. 2004, Ph.D. Thesis, IfA, University of Hawaii
 Ishigaki, T., et al. 2000, *PASJ*, 52, 185
 Iwasawa, K., Crawford, C. S., Fabian, A. C., & Wilman, R. J. 2005, *MNRAS*, 362, L20
 Iwasawa, K., Sanders, D. B., Evans, A. S., Trentham, N., Miniutti, G., & Spoon, H. W. W. 2005, *MNRAS*, 357, 565
 Iwasawa, K., Sanders, D. B., Evans, A. S., Mazzarella, J. M., Armus, L., & Surace, J. A. 2009, *ApJ*, 695, L103
 Iwasawa, K., et al. 2011, *A&A*, 529, A106
 Jarrett, T. H., et al. 1999, *AJ*, 118, 2132
 Jiang, C. Y., et al. 2008, *ApJ*, 675, 1095
 Johansson, P. H., Burkert, A., & Naab, T. 2009, *ApJ*, 707, L184
 Karl, S. J., Naab, T., Johansson, P. H., et al. 2010, *ApJ*, 715, L88
 Kewley, L. J., Groves, B., Kauffmann, G., & Heckman, T. 2006, *MNRAS*, 372, 961
 Khachikian, E., et al. 2006, *MNRAS*, 368, 461
 Kim, D.-C., Sanders, D. B., Veilleux, S., Mazzarella, J. M., & Soifer, B. T. 1995, *ApJS*, 98, 129
 Kollatschny, W., & Kowatsch, P. 1998, *A&A*, 336, L21
 Komossa, S., Burwitz, V., Hasinger, G., Predehl, P., Kaastra, J. S., & Ikebe, Y. 2003, *ApJ*, 582, L15
 Koss, M., Mushotzky, R., Treister, E., et al. 2012, *ApJ*, 746, L22
 Krist, J. 1993, *ADASS II*, 52, 536
 Krolik, J. H., Madau, P., & Zycki, P. T. 1994, *ApJ*, 420, L57
 Kuntz, K. D., Harrus, I., McGlynn, T., et al. 2008, *PASP*, 120, 740
 Lacey, C. G., et al. 2008, *MNRAS*, 385, 1155
 Larsen, S. S., & Richtler, T. 1999, *A&A*, 345, 59
 Lauer, T. R., & Boroson, T. A. 2009, *ApJ*, 703, 930
 Laurent, O., Mirabel, I. F., Charmandaris, V., Gallais, P., et al. 2000, *A&A*, 359, 887
 Le Floc'h, E., et al. 2005, *ApJ*, 632, 169

- Leipski, C., Falcke, H., Bennert, N., Huttemeister, S. 2006, *A&A*, 455, 161
- Lim, A. J. 2003, *Rev. Mex. A&A Conf. Ser.*, 15, 131
- Liu, X., Greene, J. E., Shen, Y., & Strauss, M. A. 2010, *ApJ*, 715, L30
- Magtesian, A. P., & Khachikian, E. Ye. 1991, *Soviet Astronomy Letters*, 17, 447
- Marconi, A., & Hunt, L. K. 2003, *ApJ*, 589, L21
- Marleau, F. R., Fadda, D., Appleton, P. N., Noriega-Crespo, A., Im, M., & Clancy, D. 2007, *ApJ*, 663, 218
- Marshall, J. A., Herter, T. L., Armus, L., Charmandaris, V., et al. 2007, *ApJ*, 670, 129
- Mason, K. O., et al. 2001, *A&A*, 365, L36
- Mazzarella, J. M., & Boroson, T. A. 1993, *ApJS*, 85, 27
- Mazzarella, J. M., Gaume, R. A., Aller, H. D., & Hughes, P. A. 1988, *ApJ*, 333, 168
- Mazzarella, J. M., Soifer, B. T., Graham, J. R., Neugebauer, G., Matthews, K., & Gaume, R. A. 1991a, *AJ*, 102, 1241
- Mazzarella, J. M., Bothun, G. D., & Boroson, T. A. 1991b, *AJ*, 101, 2034
- McCall, M. L. 2004, *AJ*, 128, 2144
- Mihos, C. 1999, *Ap&SS*, 266, 195
- Mihos, J. C., Dubinski, J., & Hernquist, L. 1998, *ApJ*, 494, 183
- Mihos, J. C., & Bothun, G. D. 1998, *ApJ*, 500, 619
- Mihos, J. C., & Hernquist, L. 1996, *ApJ*, 464, 641
- Mirabel, I. F., et al. 1998, *A&A*, 333, L1
- Modica, F., Vavilkin, T., Evans, A. S., et al. 2012, *AJ*, 143, 16.
- Mould, J. R., et al. 2000a, *ApJ*, 529, 786
- Mould, J. R., et al. 2000b, *ApJ*, 545, 547
- Murphy, T. W., Jr., Armus, L., Matthews, K., et al. 1996, *AJ*, 111, 1025
- Nagar, N. M., Wilson, A. S., Falcke, H., et al. 2003, *A&A*, 409, 115
- Nagar, N. M., Falcke, H., & Wilson, A. S. 2005, *A&A*, 435, 521
- Oesch, P. A., Carollo, C. M., Feldmann, R., et al. 2010, *ApJ*, 714, L47
- Owen, F. N., O’Dea, C. P., Inoue, M., & Eilek, J. A. 1985, *ApJ*, 294, L85
- Peeters, E., Hony, S., Van Kerckhoven, C., et al. 2002, *A&A*, 390, 1089
- Peeters, E., Spoon, H. W. W., & Tielens, A. G. G. M. 2004, *ApJ*, 613, 986
- Peng, C. Y., Ho, L. C., Impey, C. D., & Rix, H.-W. 2002, *AJ*, 124, 266
- Petrosian, A. R., Saakian, K. A., & Khachikian, E. E. 1978, *Astrofizika*, 14, 69
- Petrosian, A. R., Saakian, K. A., & Khachikian, E. E. 1979, *Astrofizika*, 15, 209
- Petrosian, A. R., Saakian, K. A., & Khachikian, E. E. 1980, *Astrofizika*, 16, 621
- Ptak, A., Heckman, T., Levenson, N. A., Weaver, K., & Strickland, D. 2003, *ApJ*, 592, 782
- Radford, S. J. E., Downes, D., & Solomon, P. M. 1991, *ApJ*, 368, L15
- Ramos Almeida, C., Pérez García, A. M., Acosta-Pulido, J. A., & Rodríguez Espinosa, J. M. 2007, *AJ*, 134, 2006
- Rieke, G. H., et al. 2004, *ApJS*, 154, 25
- Roche, P. F., & Aitken, D. K. 1984, *MNRAS*, 208, 481
- Rodríguez, C., Taylor, G. B., Zavala, R. T., Peck, A. B., Pollack, L. K., & Romani, R. W. 2006, *ApJ*, 646, 49
- Risaliti, G., Gilli, R., Maiolino, R., & Salvati, M. 2000, *A&A*, 357, 13
- Rush, B., Malkan, M. A., & Edelson, R. A. 1996, *ApJ*, 473, 130
- Sanders, D. B., Scoville, N. Z., Young, J. S., Soifer, B. T., et al. 1986, *ApJ*, 305, L45
- Sanders, D. B., Mazzarella, J. M., Kim, D.-C., Surace, J. A., & Soifer, B. T. 2003, *AJ*, 126, 1607 (RBGS)
- Sanders, D. B. & Mirabel, I. F. 1996, *ARA&A*, 34, 749
- Sanders, D. B., Soifer, B. T., Elias, J. H., et al. 1988a, *ApJ*, 325, 74
- Sanders, D. B., Soifer, B. T., Elias, J. H., et al. 1988b, *ApJ*, 328, L35
- Sanders, D. B., Scoville, N. Z., & Soifer, B. T. 1991, *ApJ*, 370, 158
- Schlegel, D. J., Finkbeiner, D. P., & Davis, M. 1998, *ApJ*, 500, 525
- Schweizer, F. 2000, *Royal Society of London Philosophical Transactions Series A*, 358, 2063
- Schweizer, F., & Seitzer, P. 2007, *AJ*, 133, 2132
- Skrutskie, M. F., et al. 2006, *AJ*, 131, 1163
- Smith, J. D. T., et al. 2007, *PASP*, 119, 1133
- Smith, J. D. T., Draine, B. T., Dale, D. A. et al. 2007, *ApJ*, 656, 770
- Solomon, P. M., & Vanden Bout, P. A. 2005, *ARA&A*, 43, 677
- Spoon, H. W. W., et al. 2004, *ApJS*, 154, 184
- Spoon, H. W. W., et al. 2007, *ApJ*, 654, L49
- Stickel, M., Lemke, D., Klaas, U., et al. 2004, *A&A*, 422, 39
- Sturm, E., et al. 2006, *ApJ*, 653, L13
- Su, K. Y. L., et al. 2004, *ApJS*, 154, 302
- Surace, J. A., Sanders, D. B., Vacca, W. D., Veilleux, S., & Mazzarella, J. M. 1998, *ApJ*, 492, 116
- Tacconi, L. J., et al. 1999, *Ap&SS*, 266, 157
- Tadhunter, C. 2008, *New Astronomy Review*, 52, 227
- Thean, A. H. C., Gillibrand, T. I., Pedlar, A., & Kukula, M. J. 2001, *MNRAS*, 327, 369
- Thompson, T. A., Quataert, E., & Murray, N. 2005, *ApJ*, 630, 167
- U, Vivian et al. 2011, *AJ*, submitted
- Ueda, Y., Ishisaki, Y., Takahashi, T., et al. 2005, *ApJS*, 161, 185
- van der Hulst, J. M., & Hummel, E. 1985, *A&A*, 150, L7
- Veilleux, S., Kim, D.-C., Sanders, D. B., Mazzarella, J. M., & Soifer, B. T. 1995, *ApJS*, 98, 171
- Veilleux, S., Kim, D.-C., & Sanders, D. B. 1999, *ApJ*, 522, 113
- Veilleux, S., Cecil, G., & Bland-Hawthorn, J. 2005, *ARA&A*, 43, 769
- Veilleux, S. 2006, *New Astronomy Review*, 50, 701
- Veilleux, S., et al. 2009, *ApJS*, 182, 628
- Wang, J., Heckman, T. M., Weaver, K. A., & Armus, L. 1997, *ApJ*, 474, 659
- Watabe, Y., Kawakatu, N., & Imanishi, M. 2008, *ApJ*, 677, 895
- Whitmore, B. C., Chandar, R., & Fall, S. M. 2007, *AJ*, 133, 1067
- Whitmore, B. C., Zhang, Q., et al. 1999, *AJ*, 118, 1551
- Whitmore, B. C., et al. 2010, *AJ*, 140, 75
- Wrobel, J. M., & Laor, A. 2009, *ApJ*, 699, L22
- Xu, C. K., Domingue, D., Cheng, Y-W, et al. 2010, *ApJ*, 713, 330
- Young, J. S., Schloerb, F. P., Kenney, J. D., & Lord, S. D. 1986, *ApJ*, 304, 443
- Yuan, T.-T., Kewley, L. J., & Sanders, D. B. 2010, *ApJ*, 709, 884
- Yun, M. S., Reddy, N. A., & Condon, J. J. 2001, *ApJ*, 554, 803
- Yun, M. S., Scoville, N. Z., & Knop, R. A. 1994, *ApJ*, 430, L109
- Zhu, M., Seaquist, E. R., & Kuno, N. 2003, *ApJ*, 588, 243
- Zhu, M., Gao, Y., Seaquist, E. R., & Dunne, L. 2007, *AJ*, 134, 118